
Cosmological radiative transfer through metals in CRASH

Luca Graziani



München 2012

Cosmological radiative transfer through metals in CRASH

Luca Graziani

Dissertation
an der Fakultät für Physik
der Ludwig–Maximilians–Universität
München

vorgelegt von
Luca Graziani
aus Macerata, Italy

München, den 17. April 2012

Erstgutachter: Prof. Dr. Simon D. M. White

Zweitgutachter: Prof. Dr. Jochen Weller

Tag der mündlichen Prüfung: 17. April 2012

Contents

Zusammenfassung	xi
Abstract	xiii
1 Introduction	1
1.1 The Big Bang cosmology	1
1.2 Structure formation in a Λ CDM Universe	7
1.3 Thesis outline	10
2 The intergalactic medium	13
2.1 General properties of the IGM	14
2.1.1 Hydrogen Ly α forest	17
2.2 Metallicity of the IGM	19
2.2.1 Observational constraints	22
2.2.2 Theoretical models of metal enrichment	25
2.2.3 Theoretical models of metal ionisation	27
3 Radiative transfer with CRASH	29
3.1 Ionisation	29
3.2 Radiative transfer	30
3.2.1 A Monte Carlo approach to the radiative transfer problem	32
3.3 The CRASH code	33
3.3.1 CRASH work-flow	34
3.3.2 CRASH software architecture	36
3.3.3 CRASH modularization and optimization	40
3.3.4 CRASH code and file structure	41
4 CRASH3: Cosmological radiative transfer through metals	45
4.1 Radiative transfer through metals	45
4.2 The photo-ionisation code Cloudy	47
4.3 Pipeline implementation	49
4.3.1 Initial conditions for CRASH3	50
4.3.2 The Cloudy database	50

4.3.3	The feedback of metals on the gas temperature	51
4.4	Tests	52
4.4.1	Test 1: Strömgren sphere with metals	52
4.4.1.1	Ionisation field	53
4.4.1.2	CRASH3 pipeline convergence	55
4.4.1.3	Metal ionisation states	59
4.4.1.4	Feedback by metals	61
4.4.2	Test 2: metal fluctuations in a HII region overlap	63
4.4.2.1	Reference case	64
4.4.2.2	Variations in the source ionising rates	66
4.4.2.3	Variations in the source spectra	68
4.4.3	Test 3: Radiative transfer on a cosmological density field enriched by metals	70
5	UV background fluctuations at $z \sim 3$	79
5.1	The IGM at the epoch of helium Re-ionisation	80
5.1.1	The equation of state of the IGM	80
5.1.2	IGM optical depths	81
5.1.3	The column density ratio η and the fluctuations of the IGM	82
5.2	Modelling the shape of the cosmic UV background	85
5.3	UV background in CRASH	86
5.3.1	Numerical scheme of the CRASH UVB	87
5.3.2	Spatial uniformity test	88
5.4	Simulation of UV background fluctuations at $z \sim 3$	92
5.4.1	Galaxy formation simulation	93
5.4.2	Radiative transfer simulation set-up	94
5.4.3	Fluctuations in η - Preliminary results.	95
6	Conclusions	101
	Bibliography	103
	Acknowledgements	120

List of Figures

1.1	CMB Map	3
1.2	Mock Catalogue and Ly α forest	9
2.1	Spectrum of the quasar PKS0454+039	16
2.2	Spectrum of the quasar SDSS J1030+0524	17
2.3	Starburst galaxy NGC 1569 [106]	19
2.4	Molecular outflow in the local early-type galaxy NGC 1266	20
2.5	Tidal interaction in the M81 group [289]	21
2.6	Observed and simulated metal enrichment in the IGM [89]	23
3.1	CRASH code Eclipse tree	40
3.2	CRASH at work	42
3.3	CRASH Simulation structure	43
4.1	CRASH3 simulation pipeline.	49
4.2	Test 1: ionising radiation.	53
4.3	Test 1: ionising luminosity per ion.	54
4.4	Test 1: ionisation fractions internal convergence in CRASH3.	56
4.5	Test 1: temperature internal convergence in CRASH3.	57
4.6	Test 1: fractions of the various metal ions as function of distance d	58
4.7	Test 1: time evolution of the metal ionisation fractions.	60
4.8	Test 1: metal cooling studied as ratio $\delta T/T$	62
4.9	Test 2: geometrical set-up.	63
4.10	Test 2: fractions of C, O, Si and gas temperature as function of h in reference case.	65
4.11	Test 2: ionisation rate variations in one source.	67
4.12	Test 2: spectral temperature variations.	69
4.13	Test 3: slice showing spatial distribution of C I	71
4.14	Test 3: temperature map in a selected slice	72
4.15	Test 3: map of x_{CV}	73
4.16	Test 3: map of x_{CIII}	74
4.17	Test 3: map of x_{OV}	75
4.18	Test 3: map of x_{OIII}	76

4.19	Test 3: map of x_{SiIV}	77
4.20	Test 3: map of x_{SiIII}	78
5.1	Test of UVB spatial uniformity for T .	89
5.2	Test of UVB spatial uniformity for x_{HeIII} .	90
5.3	UVB Simulation: $\eta(\Delta)$	96
5.4	UVB Simulation: statistical distribution of η in the cube	97
5.5	UVB Simulation: statistical distribution of $200 < \eta < 500$ in the cube	98

List of Tables

1.1	WMAP-5 Cosmological parameters	3
4.1	Ionisation potentials for H, He, C, O and Si	50
4.2	Grid of simulations in Test 2.	63
5.1	UVB simulation grid	95

Zusammenfassung

Die modernen Theorien des Ursprungs und der Entwicklung von Strukturen im Universum setzen die Existenz des überall verbreiteten Intergalaktischen Mediums (IGM) voraus. Im IGM erwartet man, dass sich der größte Teil kosmischer baryonischer Materie in Form von diffusem und hoch-ionisiertem Gas befindet, welches aus Wasserstoff, Helium und schweren Elementen besteht. Die physikalische Evolution des IGM im Laufe der kosmischen Zeit stellt eine Schlüsselfrage in der modernen physikalischen Kosmologie dar. Die Antwort auf dieses Problem setzt das Begreifen von vielen Feedback-Prozessen voraus, die durch Beobachtungen noch nicht ausführlich erläutert wurden.

Sowohl bei kleiner als auch bei hoher Rotverschiebung wurden schwere Elemente in den verschiedenen Komponenten des IGM ausführlich beobachtet, in denen sie als Metall-Ionen mit einer Fülle von unterschiedlichen Ionisationsstufen vorhanden sind. Um die richtige Interpretation des Anteils und des physikalischen Zustandes der Metalle bei jeder Rotverschiebung erhalten zu können, muss man eine präzise Modellierung der Metall-Photoionisation erstellen.

Ziel dieser Arbeit ist, ein neues Modell des Strahlungstransports im IGM zu entwickeln und die Effekte der Ausbreitung von Strahlung auf Metall-Ionisation zu beurteilen.

Die Berücksichtigung von Metallen in einem kosmologischen Strahlungstransportscode ist allerdings ein theoretisch besonders komplexes Problem. Um diese Aufgabe zu erfüllen, sind ein tiefgehendes Verständnis der Physik der photoionisierten Regionen, eingehende Kenntnisse des Strahlungstransportproblems in seinen formalen Aspekten und ebenso in der Modellierung, sowie höhere Fähigkeiten und Kompetenzen der Softwareentwicklung erforderlich.

Am Anfang dieser Doktorarbeit wurde die Entwicklung und die Anwendung des Strahlungstransportscodes `CRASH` erläutert. Spezifische Probleme der Modellierung des Strahlungstransports wurden theoretisch und praktisch im Code in Angriff genommen und gelöst. Das wichtigste Ergebnis dieses ersten Schrittes ist eine erheblich aktualisierte und erweiterte Version von `CRASH`. Diese neue Version verbessert ihre Modellierungsfähigkeiten in komplexen kosmologischen Szenarien, um die Reionisation von Wasserstoff und Helium detailliert zu simulieren.

Ferner habe ich die Probleme der Erweiterung von `CRASH`, welche die Einführung der Photoionisation der Metalle im IGM aufwirft, eingehend untersucht. Weiterhin wurden verschiedene Photoionisation-Modelle mit Metallen berücksichtigt; besonders habe ich den wissenschaftlichen Code `Cloudy` in Betracht gezogen.

In dieser Arbeit präsentiere ich eine neuartige Strategie zur Kopplung von **CRASH** und **Cloudy**, anhand derer ich ein numerisches Verfahren auch mittels einer eigens aufgebauten relationalen Datenbank gestaltet und implementiert habe (Software Pipeline). Der neue Code, **CRASH3** genannt, wurde in einer Reihe von idealisierten Fällen (z.B. in einer Strömren-Sphäre, die mit Metallen angereichert ist) ausgiebig getestet und, um seine Eignung zur Simulation von realistischen Szenarien nachzuweisen, in einer kosmologischen hydrodynamischen Simulation betrachtet.

Der letzte Teil dieser Doktorarbeit konzentriert sich auf das Problem eines räumlich fluktuierenden UV-Hintergrundes (UV-Background, UVB) in der Epoche der Reionisation von Helium. Das Modellierungsproblem eines UV-Hintergrundes ohne räumliche Fluktuationen bei einer Rotverschiebung von etwa $z \sim 3$ wird danach mit besonderer Betonung eingeführt, um genau zu erklären, wie zentral die Rolle sein könnte, die der Strahlungstransport in den Ionisationsstufen der im IGM vorhandenen Metalle spielt. Zu diesem Zweck habe ich ein hoch entwickeltes Verfahren vollständig neu gestaltet, implementiert und getestet, welches die räumliche Gleichmäßigkeit des UVB-Felds verbessert und das numerische Rauschen verringert.

Die neueste Version von **CRASH3** einschließlich der neuen UVB-Implementierung und der Photoionisation von Metallen ist zur ersten physikalischen Anwendung bereit, um weitere Details über die spektrale Form des UV-Hintergrundes bei einer Rotverschiebung von etwa $z \sim 3$ zu enthüllen und die derzeitige Kenntnisse der Einschränkungen erheblich zu verbessern.

Abstract

Modern theories of structure formation and evolution predict the existence of a pervasive Intergalactic Medium (IGM) in which the majority of the cosmic baryons is expected to reside as a very diffuse and fully ionised gas composed by hydrogen, helium and traces of metals. The physical evolution of the IGM through cosmic time is one of the key questions of modern physical cosmology and involves a wide range of feedback processes which are still poorly constrained by observations.

Metals have been extensively observed both at low and high redshift in the various components of the IGM, in which they reside as a plethora of different ionised states. The correct interpretation of their abundance and physical state at any redshift then requires an accurate modelling of metal photo-ionisation.

The modelling of the radiative transfer through the IGM and the calculation of its effects on metal ionisation is the focus of the present work.

The inclusion of metals in a cosmological radiative transfer code is a complex problem requiring a deep understanding of the physics in photo-ionised regions, knowledge of the radiative transfer problem in its formalism and modelling, as well as advanced numerical skills.

The work presented in this thesis then starts with the development and application of the radiative transfer code `CRASH`.

Specific problems related to the radiative transfer modelling have been addressed and solved both theoretically and practically in the code. The main result of this first step is the release of a substantially renewed and extended version of `CRASH` increasing its capabilities of modelling complex cosmological scenarios as required in hydrogen and helium Re-ionisation simulations.

The issues related to the extension of `CRASH` including the photo-ionisation of the metals present in the IGM have been investigated. Photo-ionisation models including metals have been considered, with particular emphasis to the scientific code `Cloudy`; a coupling strategy between `CRASH` and `Cloudy` has been proposed and fully implemented as numerical pipeline including a database support. The new code, called `CRASH3`, has been fully tested in a number of idealised cases (as a Strömgren sphere enriched with metals) as well as in the more realistic context of a cosmological hydrodynamic simulation.

The last part of this thesis focuses on the problem of a fluctuating UV background (UVB) at the epoch of helium Re-ionisation. The issue of modelling a uniform UV background at $z \sim 3$ is introduced with a particular emphasis devoted to the role that could

be played by radiative transfer effects on the ionisation states of the metals present in the IGM. To this aim, an advanced numerical scheme, improving the spatial uniformity of the UVB field and reducing the numerical noise, has then been proposed, implemented and fully tested.

The latest version of **CRASH3** including the new UVB implementation and the metal photo-ionisation is ready for its first physical application, i.e. setting more stringent constraints compared to what is presently available on the UVB shape at $z \sim 3$.

Chapter 1

Introduction

Modern physical cosmology has the ambitious aim of understanding the origin and the evolution of cosmic structures assuming the Standard Hot Big Bang model, in which the Universe evolves through different epochs as it expands and cools down. A coherent description of the formation and evolution of the observed Cosmo is an exceptional task which borrows knowledge from many complementary fields. Theoretical and particle physics are necessary to set up the basic equations describing the Universe expansion, the origin of the quantum fluctuations and the formation of subatomic particles in its early stages. Stellar and galactic astrophysics are required instead to explain the formation of stars, the chemical evolution of the Universe, and the nature of the complex galactic structures as observed today. Nevertheless, the knowledge of standard physics seems insufficient to justify the dynamics of galaxies and clusters, as well as the recent observations indicating an accelerated expansion of our Universe. An unknown type of massive particle, called Dark Matter, is in fact required to justify the dynamical gravitational field in which the galaxies form and evolve, as well as to describe their large-scale structure [55, 244]. The properties of a new kind of energy (Dark Energy), which seems to pervade the Universe, will be hopefully understood in the future [36].

In the first Section of this Chapter, I will introduce the foundations of the Big Bang Cosmology with the basic formalism describing the Universe expansion. More details can be found with the same formalism in [174]. In the second Section I will briefly address the Λ CDM model also providing the driving ideas of the current theory of structure formation. In the final Section I will describe the outline of my thesis.

1.1 The Big Bang cosmology

In the Big Bang paradigm [97], the primordial phase of our Universe is characterised by a rapid, exponential expansion (*Inflation phase*) resulted from a series of symmetry-breaking transitions at early epochs ($t \sim 10^{-35} - 10^{-33}$ s), associated with some unknown quantum scalar field [145, 8]. A rigorous description of the physical Universe can not be made because the current high energy physics is valid at energies up to $E \sim 1$ GeV, corresponding to

temperatures $T \lesssim 10^{13}$ K ($t \geq 10^{-6}$ s). After the Inflation, an extremely hot, dense and homogeneous primordial plasma composed by pions ($\pi^{\pm,0}$), nucleons (n,p), charged leptons (e^{\pm}, μ^{\pm}) and their neutrinos $\nu_{e,\mu}$ (all in equilibrium with photons at $T \sim 3 \cdot 10^{12}$ K) is created by the confinement of quarks into hadrons. Following the expansion, this plasma starts to cool down and to form all the subatomic particles in a *Baryogenesis* process within few minutes [274]; the same process freezes out the fundamental ratio n/p $\sim 1/10$. The standard nucleosynthesis of protons and neutrons to produce Deuterium starts when the temperature drops below $T \sim 10^9$ K ($t \sim \text{few minutes}$). As the Universe expands and cools down below a few thousand degrees Kelvin ($t \sim 4 \cdot 10^5$ yrs) the formation of the primordial atoms is allowed via atomic recombination. The *Recombination era* sets up the baryonic component of the current Universe in form of atomic hydrogen (H $\sim 76\%$ in mass fraction) and helium (${}^4\text{He} \sim 24\%$ in mass fraction), some isotopes (D, ${}^3\text{He}$, $[(\text{D} + {}^3\text{He})/\text{H}] \lesssim 10^{-4}$) and traces of ${}^7\text{Li}$ ($[{}^7\text{Li}/\text{H}] \sim 10^{-10}$)¹. At the same time, a decrease in the abundance of free electrons allows the Universe to become transparent to the relativistic component (photons and neutrinos) which expands freely creating a primordial background; the energy density in relativistic particles becomes smaller than that in the non-relativistic ones and the Universe enters the so called *Matter Dominated epoch*.

Today, we observe the fossil record of the early hot phase [68], as an almost isotropic and uniform Cosmological Microwave Background (CMB) composed by photons with a black body distribution of temperature $T_{\text{CMB}} = 2.726 \pm 0.010$ K. A long series of space missions started in the 1990s with the Cosmic Background Explorer (COBE), and continued with the 7-years Wilkinson Microwave Anisotropy Probe (WMAP) [135], had the purpose of studying the properties of the CMB. The isotropy of the CMB first confirmed the ideas postulated by Einstein in its cosmological principle, i.e. that the distribution of matter and energy must be homogeneous and isotropic on the largest scales (≥ 200 Mpc). Today, the isotropy is independently confirmed by the distribution of faint radio sources, the optically selected galaxies and the x-ray background (see [286] for a review). A rich set of information is contained in the primordial background: the CMB constraints the geometry of the Universe to a flat model (see discussion of Equation 1.4 and its consequences in 1.15) and provides estimates of the baryonic ($\sim 4.5\%$) versus dark ($\sim 23\%$) matter, indicating that a new kind of dark energy is pervading the Universe at our epoch, if the flat model holds (see Equation 1.15). Finally, CMB records the imprint of primordial fluctuations from which the structure formation process originated (see Figure 1.1 both panels). Table 1.1 summarises the main cosmological parameters provided by the WMAP-5 data release [242, 134, 135].

The Hubble law of cosmic expansion is the second pillar of the modern cosmology. In 1929 Hubble discovered that galaxies appear to recede with a velocity v_r proportional to their distance r from us. This in turn confirms that the early Universe was a lot smaller and denser in its first stages. Assuming the expansion as homogeneous and isotropic, the Hubble law can be written as:

$$v_r = \dot{r} = H(t) r; \quad H(t) \equiv \dot{a}(t) / a(t), \quad (1.1)$$

¹Where $[A/H]$ indicates $\log(A/H) - \log(A/H)_{\odot}$.

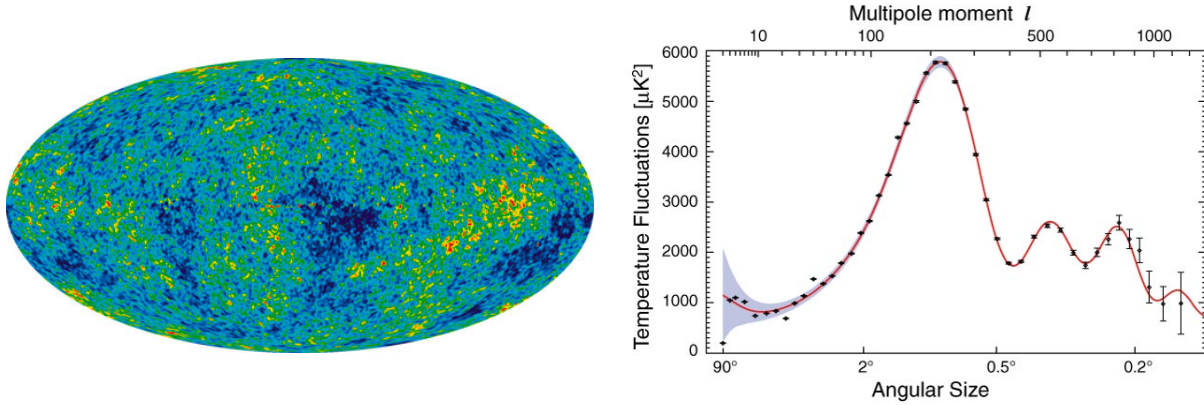


Figure 1.1: **Left panel:** the detailed, all-sky picture of the infant Universe created from seven years of WMAP data. The image reveals 13.7 billion year old temperature fluctuations (shown as colour differences). Adapted from WMAP Science Team (<http://map.gsfc.nasa.gov/media/101080/index.html>). **Right panel:** the "angular spectrum" of the temperature fluctuations in the WMAP full-sky map. The peaks and valleys in the angular power spectrum are caused by acoustic waves present in the last scattering surface of the CMB photons. The heights (depths) and positions of these peaks (valleys) depend on the density of baryonic matter, on the total mean density of the Universe, Hubble constant and other cosmological processes (e.g. the effects of cosmic Re-ionisation). Adapted from WMAP Science Team (<http://map.gsfc.nasa.gov/media/111133/index.html>).

parameter	symbol	WMAP-5 alone	+BAO+SNe
CMB temperature	T_{CMB}	2.728 ± 0.004 K	
total matter density	Ω_{tot}	$1.099^{+0.100}_{-0.085}$	1.0052 ± 0.0064
matter density	$\Omega_{m,0}$	0.258 ± 0.03	0.279 ± 0.015
baryon density	$\Omega_{b,0}$	0.0441 ± 0.0030	0.0462 ± 0.0015
cosmological constant	$\Omega_{\Lambda,0}$	0.742 ± 0.03	0.721 ± 0.015
Hubble constant	h	$0.719^{+0.026}_{-0.027}$	0.701 ± 0.013
power-spectrum norm.	σ_8	0.796 ± 0.036	0.817 ± 0.026
Age of Universe	t_0	13.69 ± 0.13 Gyr	13.73 ± 0.12 Gyr
decoupling red-shift	z_{dec}	1087.9 ± 1.2	1088.2 ± 1.1
Re-ionisation optical depth	τ	0.087 ± 0.017	0.084 ± 0.016
spectral index	n_s	$0.963^{+0.014}_{-0.015}$	$0.960^{+0.014}_{-0.013}$

Table 1.1: Cosmological parameters provided by WMAP-5 data release and corrected by data from baryonic acoustic oscillations (BAO) + SNe.

where $H(t)$ is called Hubble parameter (see Equation 1.17), $a(t)$ is the expansion scale factor and both vary with time. The value of H at the present time t_0 is called Hubble constant and it is often defined in terms of the dimensionless Hubble constant h as:

$$H_0 = 100h \text{ km s}^{-1} \text{ Mpc}^{-1}. \quad (1.2)$$

The value of h is constrained by a number of observations such as Cepheids by the Hubble Space Telescope (HST) [86], which gives $h = 0.72 \pm 0.08$. Secondary distance indicators, such as the Tully–Fisher relation, the fundamental plane of elliptical galaxies, Type Ia supernovae and the surface brightness fluctuations as well as the CMB (see Table 1.1), give an independent and compatible estimate in the range $h = 0.5 - 0.8$.

A direct consequence of this expansion is the stretching of wave signals propagating in the Universe. In the case of one photon with wavelength λ emitted at a time $t < t_0$, the Universe expansion implies that it will be observed at present time t_0 at longer (i.e. red shifted) wavelength $\lambda_0 = \lambda a_0/a(t)$ on the line of sight. Here we have set $a_0 = a(t_0)$.

The amount of redshift z suffered by the photon is defined as:

$$z \equiv \frac{\lambda_0}{\lambda} - 1 = \frac{a_0}{a(t)} - 1. \quad (1.3)$$

It is immediately seen that, because of the constancy of the speed of light, the redshift z of an object is also a distance estimator.

It is possible to formally derive $a(t)$ from the field equations of the General Relativity, which describe the geometric properties of the space-time, as determined by the distribution of matter and energy. In the case of a homogeneous and isotropic Universe, these are described by the Robertson-Walker metric (ds^2):

$$ds^2 = c^2 dt^2 - a^2(t) \left[\frac{dr^2}{1 - Kr^2} + r^2 (d\vartheta^2 + \sin^2 \vartheta d\varphi^2) \right], \quad (1.4)$$

where c is the speed of light, K is the curvature and $(r, \vartheta, \varphi, t)$ are the space-time metric coordinates; the special case $K = 0$ describes a flat space in which r is the radial coordinate and the geodesic distance. By using this metric and the energy-momentum tensor of a uniform ideal fluid with energy density ρc^2 and pressure P , it is possible to reduce the Einstein field equations into the Friedman equation:

$$\left(\frac{\dot{a}}{a} \right)^2 = \frac{8\pi G}{3} \rho - \frac{Kc^2}{a^2} + \frac{\Lambda c^2}{3}, \quad (1.5)$$

where Λ represents the Einstein's cosmological constant and G is the gravitational constant. The Friedman equation relates the cosmological expansion to the values of the density, the curvature and the Λ at each epoch of the Universe.

To close the cosmological model we need an equation of state $P(\rho)$, an equation specifying the thermal state evolution in time, as well as initial conditions in the CMB.

The thermodynamic properties of a homogeneous and isotropic expanding Universe can be described in terms of a small adiabatic system of comoving volume $V \propto a^3(t)$, which follows the Universe evolution in time. The properties of this volume can be then extended to the entire Universe by using the isotropy and homogeneity.

The adiabatic expansion of the volume V is established preserving the entropy per unit comoving volume ($dS = 0$) by the second principle of Thermodynamics:

$$dU + PdV = 0. \quad (1.6)$$

A decrease or an increase of the internal energy of the Universe, U , is caused by its expansion depending on whether $P \leq 0$. From Equation 1.6 we then obtain density and pressure evolution as function of the scale factor a :

$$\frac{d\rho}{da} + 3 \left(\frac{\rho + P/c^2}{a} \right) = 0. \quad (1.7)$$

To specify the type of the matter (relativistic and/or non relativistic) involved at any epoch of the evolution, the internal energy U must be expressed in terms of ρc^2 . The imprints in the CMB show that the Universe has experienced many phases during its expansion passing from a radiation dominated phase to a matter dominated phase, in its late stages. Considering all the possible energy densities, we can write ρc^2 as:

$$\rho c^2 = \rho_m c^2 + \rho_m \epsilon + \frac{4\sigma_{\text{SB}}}{c} T^4 + \rho_\Lambda c^2, \quad (1.8)$$

where ρ_m represents the matter density and $\epsilon = \frac{3}{2} k_B T / m$ the internal energy per unit mass of a mono-atomic ideal gas of temperature T . The contribution of the non relativistic matter, as sum of the rest mass energy and the internal energy, is described by the first two terms of the last equation. The third term is the energy contribution due to the radiation in thermal equilibrium on a black body spectrum, with temperature T , as described in the CMB, and σ_{SB} is then the Stefan-Boltzmann constant. Finally, in the last term, we consider the possibility of a contribution from vacuum quantum fluctuations (linked to the cosmological constant Λ) by considering an energy component with 'mass' density $\rho_\Lambda = \Lambda c^2 / 8\pi G$ and pressure $P_\Lambda = -\rho_\Lambda c^2$.

It is common practice to express the equation of state of the Universe by introducing an 'equation of state parameter' w :

$$P = w\rho c^2. \quad (1.9)$$

Appropriate values of w must be specified to describe the various phases which the Universe goes through during its evolution. For a matter dominated Universe, it is possible to show that a non-relativistic gas is well approximated by a fluid of zero pressure (referred to as dust fluid) and then we set $w = 0$. At early times, when the radiation dominates, the fluid is ultra-relativistic and $w = 1/3$. In the case of a vacuum energy dominated Universe, $P_\Lambda = -\rho_\Lambda c^2$ and the vacuum term provides a positive contribution to the expansion.

Introducing the values of these various components at the present time t_0 : $\rho_{m,0}$, $\rho_{r,0}$, $\rho_{\Lambda,0}$, and assuming that there are no processes transforming one component to another, we can write the Friedmann equation in the intuitive form:

$$\left(\frac{\dot{a}}{a}\right)^2 = H^2(t) = \frac{8\pi G}{3} \left[\rho_{m,0} \left(\frac{a_0}{a}\right)^3 + \rho_{r,0} \left(\frac{a_0}{a}\right)^4 + \rho_{\Lambda,0} \right] - \frac{Kc^2}{a^2}. \quad (1.10)$$

where the expansion is here related to the values of K and to the various densities, at the present time t_0 . As shown by the CMB, our Universe is almost flat and the current density in non-relativistic matter is significant (see Table 1.1). Setting then $K = 0$ in the formula 1.10, we immediately see that the Universe is destined to an infinite increase of its radius in time.

The current estimates for the densities in the Friedmann equation are generally reported as function of the critical density $\rho_{crit}(t)$ at time t , defined as:

$$\rho_{crit}(t) \equiv \frac{3H^2(t)}{8\pi G}. \quad (1.11)$$

The total rest mass density of non-relativistic matter in the Universe is expressed in terms of an adimensional cosmic density parameter $\Omega_{m,0}$ as:

$$\rho_{m,0} = \Omega_{m,0} \rho_{crit,0} \approx 1.88 \cdot 10^{-29} \Omega_{m,0} h^2 \text{ g cm}^{-3}, \quad (1.12)$$

$\Omega_{m,0}$ comes from the CMB estimates and it is tabulated in 1.1. The current density in the relativistic component appears today as dominated by the CMB plus the contribution of a neutrino background as:

$$\rho_{r,0} \approx 7.8 \cdot 10^{-34} \text{ g cm}^{-3}, \quad \Omega_{r,0} \approx 4.2 \cdot 10^{-5} h^{-2}. \quad (1.13)$$

The constraint to the present-day value of ρ_{Λ} is derived from the Friedmann equation as:

$$\rho_{\Lambda,0} = \rho_{crit,0} (1 - \Omega_{m,0} - \Omega_{r,0}). \quad (1.14)$$

Introducing the mean density $\bar{\rho}_0$ at present time and its density parameter as $\Omega_0 \equiv \bar{\rho}_0 / \rho_{crit,0}$, it is possible to describe the curvature of the Universe in terms of critical density as:

$$K = \frac{H_0^2 a_0^2}{c^2} (\Omega_0 - 1). \quad (1.15)$$

By expanding Ω_0 in terms of single components:

$$\Omega_0 = \Omega_{m,0} + \Omega_{r,0} + \Omega_{\Lambda,0}, \quad (1.16)$$

the Friedmann equation can be also written as function of parameter values at present time:

$$\left(\frac{\dot{a}}{a}\right)^2 = H_0^2 \left[\Omega_{\Lambda,0} + (1 - \Omega_0) (1 + z)^2 + \Omega_{m,0} (1 + z)^3 + \Omega_{r,0} (1 + z)^4 \right] \equiv H_0^2 E^2(z) \quad (1.17)$$

In the case of a flat model in which $1 = \Omega_{m,0} + \Omega_{\Lambda,0}$, the expansion is accelerating at present time because $\Omega_{m,0} < 2/3$, as predicted by the CMB. Extending the definition of the cosmic density parameter at generic time t , as $\Omega(t) \equiv \rho(t)/\rho_{crit}(t)$, it is possible to derive the parameter evolution in redshift, by knowing the values at the present epoch. In fact the following useful equations hold:

$$\Omega(z) - 1 = (\Omega_0 - 1) \frac{(1+z)^2}{E^2(z)}; \quad (1.18)$$

$$\Omega_{\Lambda}(z) = \frac{\Omega_{\Lambda,0}}{E^2(z)}; \quad \Omega_m(z) = \frac{\Omega_{m,0}(1+z)^3}{E^2(z)}; \quad \Omega_r(z) = \frac{\Omega_{r,0}(1+z)^4}{E^2(z)}. \quad (1.19)$$

After the recombination epoch, the primordial fluctuations observed in the CMB set up the initial conditions for the structure formation. These fluctuations start growing and form structures under the gravitational field created by the dominant Dark Matter component. The commonly adopted theory for structure formation is the Cold Dark Matter model and it is briefly introduced in the next Section.

1.2 Structure formation in a Λ CDM Universe

Nowadays there are evidences at different scales that the total amount of gravitational matter in the Universe can not reside just in baryons. At the galactic scale the luminous matter is insufficient to justify the flatten behaviour of the galactic rotational curves (see [174] and references therein). In addition, the global motion of the Milky Way satellites and nearby galaxies, requires the existence of a halo of invisible gravitationally interacting matter. On cosmological scales, the amount of baryonic matter predicted by the cosmic nucleosynthesis [274] is far too little to account for the CMB measurements (see Table 1.1 and references [242, 134, 135]). These facts are sufficient to exclude the possibility that the Universe was closed by baryons and to set an upper limit on the baryon density of only 20 percent. Temperature anisotropies in the CMB make pure baryonic scenarios difficult to construct also because there is not enough time between the recombination epoch and today for the structures to grow at the level we observe in our nearby Universe.

The cosmological model which better matches all the current theoretical and observational constraints is called Λ CDM model. This model introduces a new kind of gravitationally interacting matter called Dark Matter (DM) as well as the additional contribution of Λ [35], in order to make the Universe flat as predicted by the CMB.

The dark matter is assumed to form as elementary particle in the early Universe but it is not predicted by Standard Model of particle physics; there are few theoretical candidates but they require an extension of the standard paradigm and none of them has been confirmed by experiments [21]. The dark matter is then defined by its properties, i.e. as collection of collisionless particles (i.e. weakly interacting) with negligible thermal velocities and evolving exclusively under gravitational forces; in that sense it is considered as 'cold' (abbreviated as CDM).

Despite these uncertainties in the physical nature of the dark matter and the role of the cosmological constant, the Λ CDM model can predict structures which satisfy many independent measurements ([13] and references therein). The initial conditions in the CMB power spectrum are in perfect agreement with the model predictions down to the Milky Way halo scale, the predicted baryon density matches with the CMB values and cosmic nucleosynthesis, and finally, the inferred value of the Hubble constant is in good agreement with direct measurements. On large scales, the galaxy clustering estimates match with the statistical properties of large surveys and weak gravitational lensing. The dark-energy contribution also agrees with the current estimates inferred from the supernovae Ia. At the scale in which dwarf galaxies form, the power spectrum of the Ly α forest in QSO spectra also confirms the Λ CDM model expectations. Nowadays the Λ CDM model is then the standard paradigm of cosmic structure formation and it is able to provide a self-consistent scheme which explains how the large-scale of the Universe originated from the small initial density fluctuations seen in the CMB data [244].

The collisionless nature of the dark matter implies that the fluctuations in its density start to grow at early times: in over-dense regions self-gravity dominates against the global expansion and, eventually, produces a local collapse that forms a bound object, in accordance with the standard Jeans model ([87, 181, 247]). To follow the first stages of the structure formation and evolution from primordial density perturbations, it is possible to use the standard linear theory describing the Universe as a fluid made of collisionless dark matter and baryons with a mean density $\bar{\rho}$, so that:

$$\rho(\vec{x}, t) = \bar{\rho}[1 + \delta(\vec{x}, t)], \quad (1.20)$$

where \vec{x} indicates the co-moving spatial coordinates, t the time, and $\delta(\vec{x}, t)$ the mass density contrast. The evolution in time of δ can be followed by the linear theory until perturbations remain small $\delta \ll 1$ (for the full treatment it is possible to consult [174]) by solving the equation ([189]):

$$\ddot{\delta} + 2H(t)\dot{\delta} = 4\pi G\bar{\rho}\delta + \frac{c_s^2}{a(t)^2}\nabla^2\delta, \quad (1.21)$$

where c_s is the sound speed and the equation of state is assumed in the form $P = P(\rho)$. For a more general treatment see Formula 4.24 in [174].

It is possible, for instance, to derive the Jeans mass limit for the collapse, within a linear treatment. As perturbations grow, while on very large scales the linear regime continues to apply, the small scales rapidly develop a non linear behaviour which requires a numerical treatment (although simple approximations of the non-linear stage of gravitational evolution have been developed by Zeldovich 1970).

Large numerical N-Body simulations, with billions of dark matter particles, have been performed to follow the non linear evolution and predict the growth of DM halos. The statistical properties of the Universe at large are well reproduced on scales up to 500 comoving Mpcs. These simulations also confirm that the non linear evolution of the structures produces a uniform and isotropic Universe. The series of Millennium runs (Millennium Run

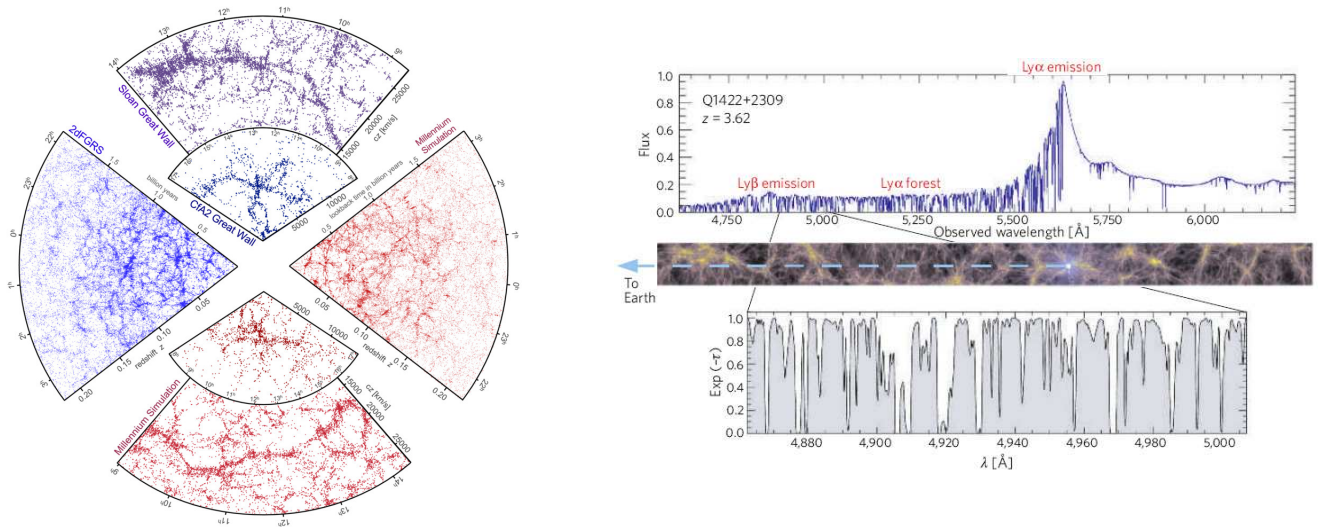


Figure 1.2: **Left panel:** galaxy distribution obtained from spectroscopic redshift surveys and from mock catalogues constructed from cosmological simulations. The small slice at the top shows the CfA2 'Great Wall', with the Coma cluster at the centre. Drawn to the same scale is a small section of the SDSS, in which an even larger 'Sloan Great Wall' has been identified. The cone on the left shows one-half of the 2dFGRS survey. At the bottom and on the right, mock galaxy surveys constructed using semi-analytic techniques to simulate the formation and evolution of galaxies within the evolving dark matter distribution of the 'Millennium' simulation (adapted from [244]). **Right panel:** the Ly α forest as a probe of large-scale structure. The panel on the top shows a typical high-resolution spectrum of a quasar at redshift $z = 3.62$. Hydrodynamical simulations reproduce the observed absorption spectra with remarkable fidelity, as illustrated by the simulated spectrum in the bottom panel, corresponding to intervening large-scale structure at $z \approx 3$. The sketch in the middle panel shows an example of the gas distribution in a simulated Λ CDM model (adapted from [244]).

[248], Millennium II [34] and the latest Millennium XXL completed in 2010) are successful examples of these dark-matter-only simulations, which progressively span larger cosmological boxes and increase in resolution, to better describe the structure of the DM halos (see Fig. 1.2 left panel).

The problem is further complicated when we include the luminous, ordinary matter in the gravitational field set up by the Dark Matter component. Baryonic matter has in fact a more complex physics that involves many phases and requires a fluid dynamic treatment. In the standard Λ CDM scenario, the baryons are expected initially to thermalise with the CMB and then to start falling into the pre-existing gravitational potential wells of the DM halos. On sufficiently small scales the power spectra of the baryon density and temperature, roughly assume the shape of the Dark Matter fluctuations, but the physics of collapsing gas is more complex. The gas can develop shocks and can be reheated up to a temperature at

which the pressure support can prevent any further accretion; a precise knowledge of the gas cooling mechanisms is then required to establish the collapse dynamics. Once the galaxy formation is set up, the physics involved in the galactic evolution is further complicated in many ways: not only the star formation is induced locally by the gas collapse in molecular clouds, but the galaxies also grow in time by interacting and merging. These processes also create large regions of shocked gas and the star formation can also be triggered by galaxy mergers. Once stars are formed, the various stages of their evolution regulate the galactic environment in terms of mechanical, chemical and radiative feedback so that the galaxy formation and evolution can not be accounted for without a precise knowledge of the many feedback processes in place ([50]).

Nowadays, the cosmological hydrodynamical simulations can handle sufficient resolution and spatial scale to accurately simulate cosmological boxes including baryons; a rich set of chemical and mechanical feedback processes can also be accounted for by including galactic winds, metal enrichment, molecular cooling and an approximate treatment of the gas turbulence (see next Chapter for more details). On large scales, one of their primary success consists in the excellent prediction of the intergalactic medium (IGM) properties, by the reproduction of the Ly α forest observed in quasi stellar objects (QSO) spectra (see panels Figure 1.2). The IGM is then one of the best environments in which hydro simulations are an invaluable tool, as illustrated in the next Chapter.

Despite their success, these simulations still suffer some serious limitations. The inclusion of a full treatment of the radiative feedback seriously limits, for instance, their execution on large scales. Further, every simulation is so computationally intense that any large parametric study, to better match fresh observational data, is simply non-viable. The implementation of a radiative transfer code is the main topic of the present work and it will be covered in details starting from Chapter 3.

On the other hand, semi-analytic modelling, relying on the mass function of collapsed objects predicted by the Press-Schechter formalism ([201]) or the predictions of large-scale DM simulations, can permit parametric studies. Semi-analytic methods reproduce the baryonic phase by using physically plausible recipes or the observational phenomenology to evolve the baryons in the DM halos, as introduced in [128]. These methods are very successful in fitting most of the present observations: the stellar mass function, the luminosity and the colour distributions of galaxies are predicted with good precision. The clustering of massive galaxies and the scaling relations between stellar mass and disk/bulge size, the gas metallicity, as well as the Tully-Fisher relation are also easily satisfied.

1.3 Thesis outline

During my PhD I have addressed the problem of simulating the light propagation in the Intergalactic Medium, and its physical consequences on its baryonic component composed by hydrogen, helium and metals.

After briefly introducing the main physics of the IGM in Chapter 2, I will describe the problem of the Cosmological Radiative Transfer (C-RT) in Chapter 3, introducing my

implementation of the new version of the numerical RT code **CRASH**.

In Chapter 4 I will describe my new pipeline extension of the **CRASH** algorithm (**CRASH3**) which includes the effects of radiative transfer on the metallic component of the IGM and calculates the metal ionisation states and the metal feedback on the gas cooling function. A series of tests validating **CRASH3** are reported in the same Chapter.

A first physical application of **CRASH3** is proposed in Chapter 5. The problem of constraining the shape of the UV background at the epoch of helium Re-ionisation is analysed and the **CRASH3** applicability established. A new UV background is proposed and fully tested. Finally, the set-up of the new application and preliminary results are illustrated in the same Chapter.

Conclusions of my PhD projects are reported in the final Chapter of this thesis.

Chapter 2

The intergalactic medium

Nowadays we have a coherent picture of the Intergalactic Medium based on a combination of observations and simulations.

In this picture the space between galaxies is neither empty nor homogeneous but the various collapsed structures are connected by an intricate series of flattened or filamentary substructures composing the so called cosmic web [32]. Substructures of that web, which extend over many hundreds of kilo parsecs, seem to strongly interact with the forming objects by radiative, mechanical and chemical feedback, as the Universe evolves in redshift.

The UV radiation emitted by stars escapes the galaxies and propagates through the IGM: HII regions then form around galaxies and overlap each other making the IGM ionised in its hydrogen component by $z \sim 6$ (*Epoch of hydrogen Re-ionisation*). As the galaxies evolve and the star formation rate (SFR) increases, another population of extremely luminous objects (QSOs) starts to be statistically relevant at lower redshift ($z < 4$). QSOs have harder spectra and can efficiently ionise the helium component of the cosmic gas; the *helium Re-ionisation* is believed to be completed by $z \sim 3$.

The interplay between the evolving galaxies and the IGM is also driven by mechanical and chemical feedback. These processes are certainly in place, at least in the proximity of the galaxies and quasars, where winds signatures have been detected in the spectra [156] and a gas metallicity component has been measured even at high redshifts [17, 18]. Because the primordial nucleosynthesis is unable to produce elements heavier than ${}^7\text{Li}$, the metal component is mainly created inside the stars in galaxies, spread out in the surrounding interstellar medium (ISM) during the many stages of stellar evolution, and then injected in the close IGM by mechanical feedback.

The baryonic component of the Universe is traditionally classified in four phases, according to its density and temperature ([64]). Matter residing into stars and cold gas in galaxies is classified as "Condensed phase" which can be easily detected. The large amount of gas trapped in the Intracluster Medium (ICM) and seen through its x-rays emission, is classified as "Hot phase" ($T \sim 10^7$ K). The "Diffuse phase" is characterised instead by very low densities and it is distributed in clouds which spatially and dynamically follow the underlying dark matter distribution; the majority of Ly α absorbers seen in QSO spectra are part of this phase. Highly ionised gas with temperatures $T \sim 10^5 - 10^7$ K, typical of

shocks, is classified as the "Warm-Hot phase". This component is extremely difficult to detect in absorption because it is fully ionised and it is also difficult to detect its emission because of its very low density [63, 45, 222]. Fukugita et al. [88] performed an inventory of baryons observed today and found roughly a half to be missing, compared with Ly α forest estimates. Cen and Ostriker [44] examined the physical properties of the warm hot intergalactic medium (WHIM) in more detail, finding that it generally resides in filamentary large-scale structures, well outside of virialized objects; by the present day, $\sim 45\%$ of the baryons are believed to reside in the warm-hot phase as predicted by hydro-simulations ([63]).

The Intergalactic Medium is then not just a static, huge repository of the primordial baryons of the Universe, but it is also a bridge between extreme cosmological scales: the rich set of feedback processes that involves its baryonic matter [50] creates many phases and regulates the environments in which generations of galaxies form and evolve. Among others, active galactic nuclei (AGN) and galactic feedback impact the temperature of the IGM providing a heating mechanism ([272]). Mechanical feedback can suppress the star formation in the host galaxy ([245]) and in nearby galaxies ([221]). Finally, the generation of large-scale magnetic fields could also be driven by feedback processes ([137, 94]).

In Section 2.1, I will briefly introduce the main properties of the Intergalactic Medium. Special attention to the current estimate of the IGM metallicity is introduced in Section 2.2. In last Section, the problem of simulating metal production and spreading is introduced and discussed from the theoretical point of view.

A larger selection of the topics summarised in this Chapter can be found in some of the excellent reviews treating the physics of the Intergalactic Medium: [50], [62], [12], [167].

2.1 General properties of the IGM

The spectra of bright sources can be used to open new windows on the Universe at different redshifts; extremely luminous objects can be used in fact as 'background light' for the IGM intervening between the source and the observer.

Since the first quasar discovery ([113]), QSO spectra have been commonly used to study the many properties of the Intergalactic Medium at redshift $z < [5 - 6]$. Because the Ly α absorption is highly sensitive to the H I component [12], the forest of this resonant lines is the best probe of the diffuse gas clouds in the IGM, and gives us a detailed picture of their abundance, composition, and kinematics ([277, 204, 14]). The gamma-ray bursts (GRBs) represent instead an excellent candidate source to probe the early IGM and to detect the population of massive stars (Pop III stars) [53] at high redshifts. The peak flux produced by GRB afterglows is comparable to that of quasars or starburst galaxies at $z \sim 1 - 2$ and, differently from galaxies and QSOs, the GRB afterglow flux is not expected to fade significantly with increasing redshift [53].

The main advantage of studies based on the absorption line spectroscopy consists in its very high sensitivity which allows precise estimates of many gas properties (see also 2.1). The line broadening provides the main set of information about the physical properties of

the absorbing gas: its density, temperature and ionisation state. Further insights on the temperature and kinematics of Ly α clouds can be obtained by measuring the line widths. Because the line recognition allows to probe these properties in the structures along the line of sight, it is then possible to explore also the redshift evolution of the IGM. Current studies, based mainly on QSO spectra, detect hydrogen lines with associated column densities as low as $N \sim 10^{12.5} \text{cm}^{-2}$ in absorption.

In Figure 2.1 I show the typical spectrum of a quasar (PKS0454 + 039) obtained with the Faint Object Spectrograph on the Hubble Space Telescope at redshift $z_{\text{QSO}} = 1.34$ ([47, 278, 177]). Neutral hydrogen located at $z < z_{\text{QSO}}$ along the line of sight will induce absorption lines at wavelengths blueward of the Ly α emission and form a forest; the region redward of the Ly α emission is instead populated only by absorption through other chemical transitions, mainly due to metal lines.

In the Ly α forest, the many absorption systems are historically classified by their column density and grouped into three main types: Ly α forest systems (or clouds), Lyman limit systems (LLSs) and Damped Lyman Systems (DLAs). Absorption systems with $N_{\text{HI}} < 10^{17.2} \text{cm}^{-2}$ are called Ly α forest clouds, those with $10^{17.2} < N_{\text{HI}} < 10^{20.3} \text{cm}^{-2}$ are Lyman limit systems (LLSs) and are spectroscopically identified by a sharp break in the spectrum due to absorption of hydrogen ionising photons. Intermediate column density LLSs can also be recognised if they have a sufficiently large column density to absorb photons with energies above the photoelectric edge or Lyman limit [89]. Systems with $N > 10^{20.3} \text{cm}^{-2}$ are finally classified as DLAs. DLAs have sufficiently high hydrogen column densities to show the radiation damping wings of the Lorentz profile, requiring a Voigt line profile for accurate fitting.

This classification is not strictly exclusive: DLAs are likely to produce Lyman limit systems, as well as lower-column-density Lyman limit systems will produce Ly α forest features. Intermediate structures, referred to as sub-damped absorbers, can be identified between these three broad classes. A finer classification is sometimes used to mark an important physical distinction between intermediate structures and the general class of DLAs: the hydrogen in the DLAs is in fact essentially neutral, while the column densities of the LLSs are sufficiently low to allow a deep penetration of the UV meta-galactic background and to maintain their gas partially ionised.

In the spectrum of the quasar under discussion for example, a damped Ly α system at $z = 0.86$ is identified and it is responsible for the Ly α absorption line at $\lambda_{\text{obs}} = 2260 \text{\AA}$ and for a Lyman limit break at $\lambda_{\text{obs}} = 1700 \text{\AA}$. The absorption at $\lambda_{\text{obs}} = 2870 \text{\AA}$ is due to the presence of C IV in the gas of the same system.

The Ly α absorption is highly sensitive to the presence of even small amounts of neutral hydrogen. At high redshift we can in fact show that the optical depth to absorption by a uniform IGM is proportional to the average fraction of neutral hydrogen [108]:

$$\tau_s = \frac{\pi e^2 f_\alpha \lambda_\alpha n_{\text{HI}}(z)}{m_e c H(z)} \approx 6.45 \cdot 10^5 x_{\text{HI}} \left(\frac{\Omega_{b,0} h}{0.0315} \right) \left(\frac{\Omega_{m,0}}{0.3} \right)^{-1/2} \left(\frac{1+z}{10} \right)^{3/2}, \quad (2.1)$$

where $H(z)$ is the Hubble parameter at redshift z , $f_\alpha = 0.4162$ and $\lambda_\alpha = 1216 \text{\AA}$ are the oscillator strength and the wavelength of the Ly α transition, and $n_{\text{HI}}(z)$ is the neutral

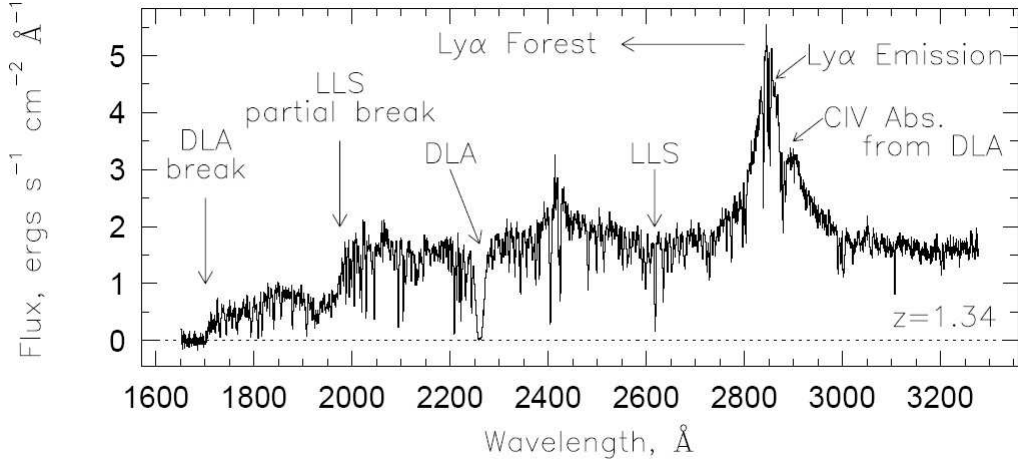


Figure 2.1: Spectrum of the quasar PKS0454 + 039 at $z = 1.34$ as obtained with the Faint Object Spectrograph on the Hubble Space Telescope. The emission lines at $\lambda = 2400\text{\AA}$ and $\lambda = 2850\text{\AA}$ are $\text{Ly}\beta$ and $\text{Ly}\alpha$. The $\text{Ly}\alpha$ forest is the ensemble of absorption lines at $\lambda < 2850\text{\AA}$. A $\text{Ly}\alpha$ absorber at $z = 0.86$ is identified as DLA and produces a Lyman limit break at $\lambda = 1700\text{\AA}$. A Lyman limit system is identified at $z = 1.15$ and produces a partial Lyman limit break at $\lambda = 1950\text{\AA}$. Many metal absorption lines are produced by the DLA at $z = 0.86$ (CIV $\lambda\lambda 1548, 1550$, for example, is redshifted onto the red wing of the quasar's Lyman emission line). Figure adapted from [174]

hydrogen density at the same redshift (assuming primordial abundances). $\Omega_{m,0}$ and $\Omega_{b,0}$ are the present-day density parameters of all matter and of the baryons, respectively (see Formula 1.12). x_{HI} is, as usual, the average fraction of neutral hydrogen. Figure 2.2 reports part of the spectrum of the quasar SDSS J1030+0524 at $z = 6.28$, around the $\text{Ly}\alpha$ emitting line. The $\text{Ly}\alpha$ emission line is shown at the redshifted wavelength $\lambda = 8850\text{\AA}$. Photons at shorter wavelengths are absorbed by the intervening neutral gas and the difference between unabsorbed expectation and the observed spectrum can be used to infer the amount of absorption, and then, to infer the presence of the hydrogen in a neutral state. In this particular quasar, this difference is very large (i.e. the observed flux is near zero) just to the blue side of the $\text{Ly}\alpha$ emission line, indicating a highly neutral intervening IGM.

Gunn & Peterson in 1965 were the first to point out that such absorption features in spectra of high redshift quasars could be used to infer the evolution of the neutral component of the IGM. Because of the high optical depth to neutral hydrogen, absorption features as those of Figure 2.1 suggest that the IGM is in a highly ionisation state, or else the radiation emitted by the QSOs would be completely absorbed. As redshift increases, more absorption is visible and many quasars beyond $z \sim 6.1$ show in their spectra large Gunn-Peterson trough as reported in [75], indicating that the IGM has a larger neutral component at these redshifts. This is the epoch when *hydrogen Re-ionisation* is thought to be completed and will be discussed in more details in the Chapters 3 and 5.

In the following Paragraphs I will briefly review the main IGM properties which can be

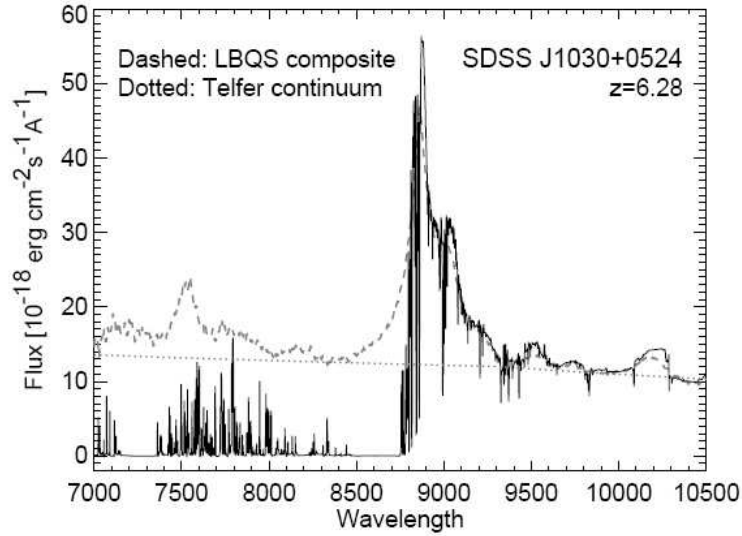


Figure 2.2: Spectrum of the quasar SDSS J1030+0524 at $z = 6.28$ as obtained with the Keck ESI spectrograph. The observed spectrum is shown in solid black line, the expected unabsorbed emission in dashed curve. This is estimated based on an average over many quasars seen at lower redshifts, and it is the sum of a smooth emission (the QSO continuum reported as dotted curve) plus the emission features from atomic resonances, i.e. the emission lines. Figure adapted from [278].

inferred from the spectra of QSOs because most of these properties are frequently assumed in the next Chapters.

2.1.1 Hydrogen Ly α forest

The substructures composing the IGM with $N_{\text{HI}} < 10^{17.2} \text{cm}^{-2}$ are observed in the quasar spectra as the Ly α forest: this appears as a series of redshifted absorption lines and has been detected for the first time in the 1960s. The cosmological origin of these lines was first clearly demonstrated by Sargent et al. (1980), who also found a substantial number of associated C IV absorbers. Fifteen years later, the first IGM hydrodynamical simulations at high redshift ([41, 290, 119, 273, 260]) allowed a detailed reproduction of the forest, also creating a visual picture of what the structures are: typically sheets and filaments, aligned with the sites of future galaxy formation.

The Paragraphs that follow briefly summarise the main properties of the Ly α forest.

Column density distribution As already discussed in the previous Section, the H I column density of the lines composing the Ly α forest is in the range $10^{12} < N_{\text{HI}} < 10^{17} \text{cm}^{-2}$. If the spectrum resolution allows to count the single absorption lines, we can statistically describe the distribution of the column densities by using a distribution function $\mathcal{F}(N_{\text{HI}})$ defined as the number of absorption lines per unit N_{HI} , per unit of the redshift

distribution. Practical application of this technique for Ly α forests at $z \gtrsim 2$ shows that the distribution is well represented by a single power law:

$$\mathcal{F}(N_{\text{HI}}) \propto N_{\text{HI}}^{-\beta}, \quad (2.2)$$

with power index $\beta \sim 1.5$. The situation can be complicated further by the appearance of relevant multicomponent structures in absorption systems with column densities above $N_{\text{HI}} > 10^{15} \text{ cm}^{-2}$ (e.g. Cowie et al 1995). Various authors (Bechtold 1987, Carswell et al 1987, Giallongo et al 1993, Meiksin & Madau 1993, Petitjean et al 1993) have presented evidence for departures from a single power law.

Temperature and turbulence When the absorption line shape can be described by a Voigt profile, the associated Doppler parameter b can then be written as the quadratic sum of its thermal and turbulent contributions:

$$b^2 = \frac{2k_B T}{m} + b_{\text{turb}}^2, \quad (2.3)$$

where b_{turb} accounts for turbulent motions, T is the gas temperature and m is the mass of the absorbing atom. k_B is, as usual, the Boltzmann constant. If it is possible to discriminate the lines, the values of b can then be used, line by line, to infer the gas temperature and the turbulent motion of the associated absorber.

High resolution spectra show that many low column densities Ly α clouds ($N_{\text{HI}} < 10^{15} \text{ cm}^{-2}$) have associated widths with $b \gg 10 - 45 \text{ km s}^{-1}$ i.e. consistent with photo-ionisation temperatures $T \sim 10^{4.5} \text{ K}$ ([37]). Some lines appear instead to be as wide as $b \sim 100 \text{ km s}^{-1}$. Cooler temperatures are possible, particularly if the gas has been expanding sufficiently fast for adiabatic cooling to be appreciable.

Absorbers sizes In principle the spectroscopy along the line of sight (LOS) of a high redshift quasar does not provide any bi-dimensional information and the geometry of the absorbing systems cannot be inferred. In case many lensed QSOs are available (i.e. pairs and group of quasars separated from few arcsec up to one arc-minute) the same absorber can be detected in two different lines of sights and a bi-dimensional information across the sky can be restored; with a few arc-seconds separation it is possible to probe scales below 100 kpc. Unfortunately only few lensed objects can be chosen as targets for Ly α spectroscopy because the number of luminous quasars in groups is very low and, in addition, their emission redshift must allow the Ly α forest to fall in the optical wavelength range. Existing estimates indicate that Ly α absorbers can have transverse sizes of about $200-500h^{-1} \text{ Kpc}$ and their geometry is more likely sheet like, in accordance with the predictions of the numerical simulations ([58]).

Helium Ly α forest By observing the neutral and singly ionised helium Ly α lines at $\lambda = 584 \text{ \AA}$ and $\lambda = 304 \text{ \AA}$, it is possible to infer more properties of the *helium Re-ionisation* and the UV background (UVB) field pervading the IGM at low redshifts. He II at $\lambda = 304 \text{ \AA}$

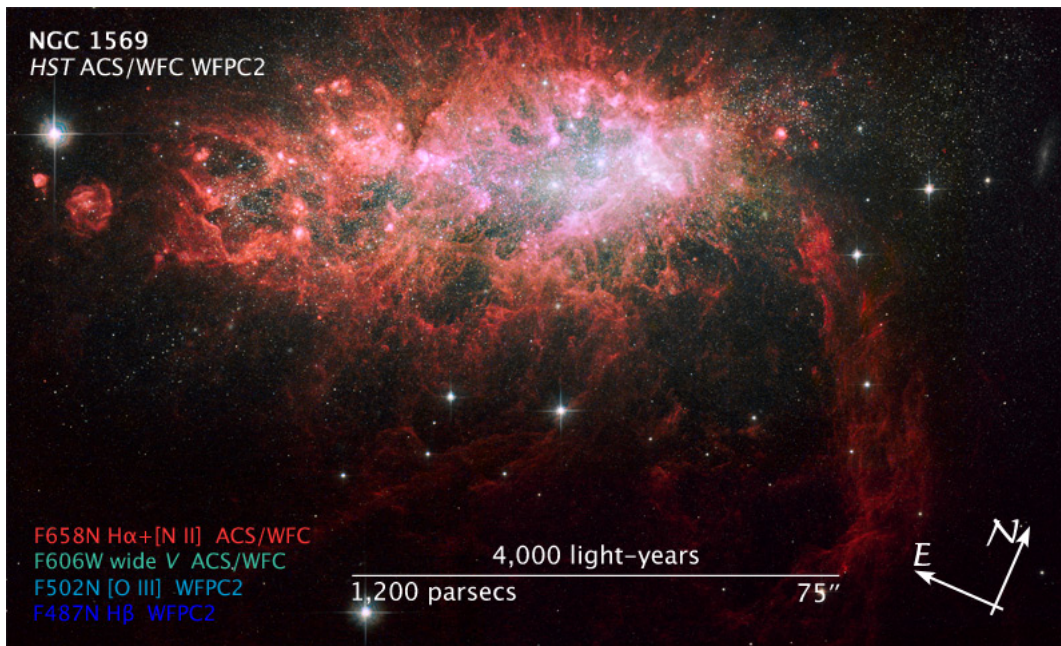


Figure 2.3: Discovered by William Herschel in 1788, NGC 1569 is a Dwarf Irregular Galaxy and it is home to three of the most massive star clusters ever discovered in the local Universe. Galaxy in the middle of a group of about 10 galaxies centred on the spiral galaxy IC 342. Gravitational interactions among the group’s galaxies may be compressing gas in NGC 1569 and igniting the star-birthing frenzy (credits: NASA, ESA, the Hubble Heritage Team (STScI/AURA), and A. Aloisi (STScI/ESA) <http://hubblesite.org/newscenter/archive/releases/2008/38/>).

is in fact a better tracer of the low density baryon distribution than H I . To observe He II it is necessary to survey many quasars redshifted to at least $z > 2-3$, so that the short wavelength $\lambda = 304\text{\AA}$ can enter the far-UV bands accessible to the Hubble Space Telescope. The first measure of intergalactic He II Ly α ([66]) used the spectrum of HS 1700+6416 at $z = 2.7$ finding a moderate optical depth of He II over the redshift range $z = 2.2-2.6$ and driving the conclusion that He II was ionised around $z \sim 3$. Subsequent observations have shown that the He II Ly α optical depth is very patchy at this redshift i.e. the variation in the ratio H I / He II can be sensitive to the UVB fluctuations.

Because the photo-ionisation rates are dominated by the UV background intensity near the ionisation edges, the measurements of the He II and H I column densities can fix the spectral shape of the UVB in the vicinity of the two wavelengths $\lambda = 228\text{\AA}$, $\lambda = 912\text{\AA}$. In Chapter 5 of my thesis I will investigate these problems in more details.

2.2 Metallicity of the IGM

Despite the negligible mass fraction of heavy elements on cosmic scales, the metallicity of

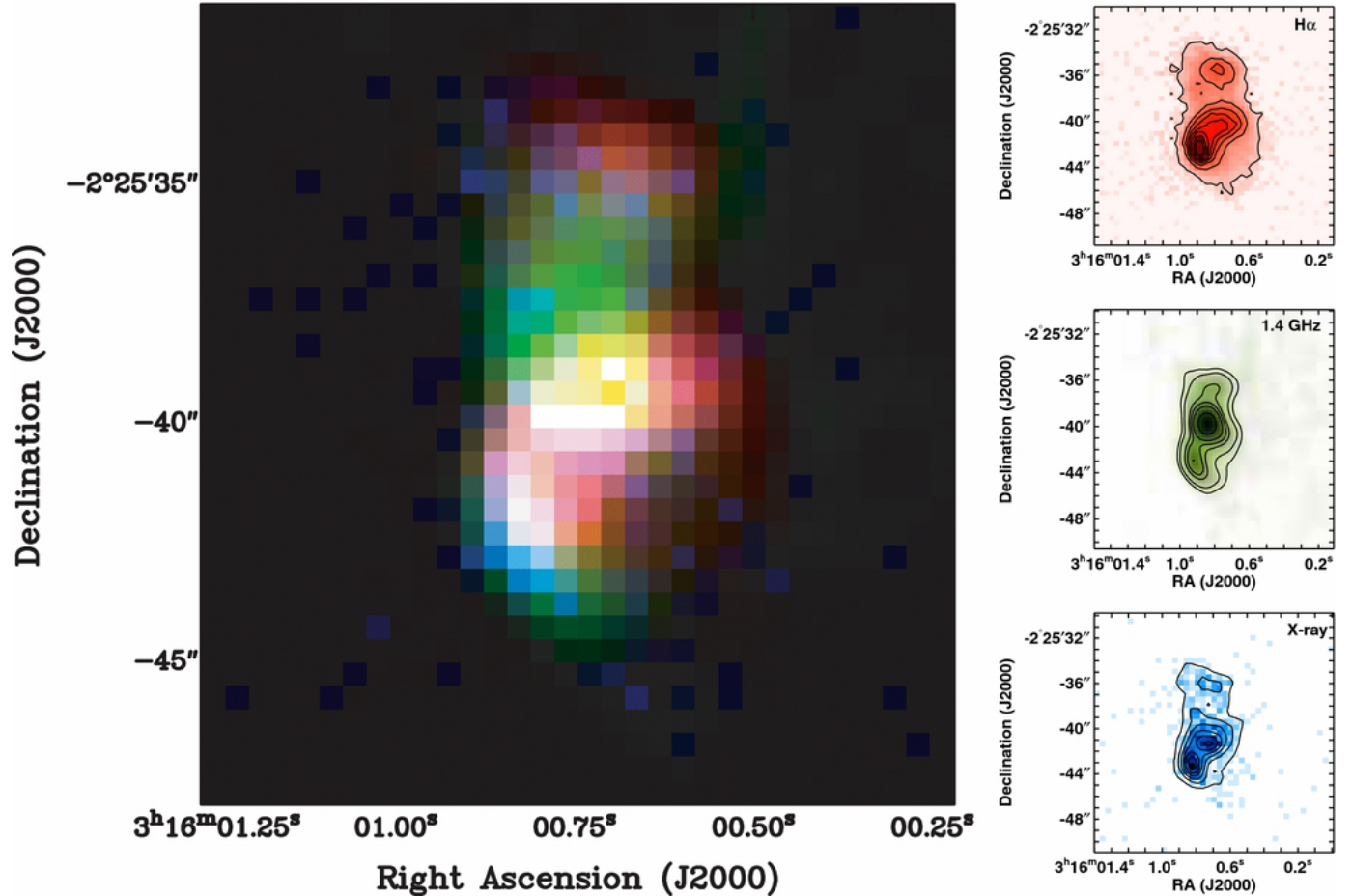


Figure 2.4: Molecular outflow in the local early-type galaxy NGC 1266 [7] **Left:** an RGB image of the H α (red), radio continuum (green), and Chandra x-ray (blue) emission. A spatial correlation is clearly seen in the area of the blue-shifted CO outflow, revealing that these features are co-spatial. We conclude that the H α features, the spurs seen in the radio continuum image, and some of the x-ray emission originate from the outflowing material, although the 1.4 GHz continuum emission could also be coming from a radio jet. **Top Right:** H α image from the SINGS survey. **Middle Right:** VLA A array 1.4 GHz continuum emission (Baan & Klockner 2006). The unresolved peak in the emission is assumed to be from an AGN, and the lobe extending south-east to north west is assumed to trace the interface between the outflowing material and the galaxy ISM. **Bottom Right:** unsmoothed Chandra x-ray image (K. Alatalo et al. 2011, in preparation). The majority of the x-ray photons from NGC 1266 can be fit with a thermal Bremsstrahlung spectrum with an excess of hard x-rays. All images are at the same spatial scale (adapted from K. Alatalo et al. 2011 ApJ 735 88 <http://iopscience.iop.org/0004-637X/735/2/88/>).

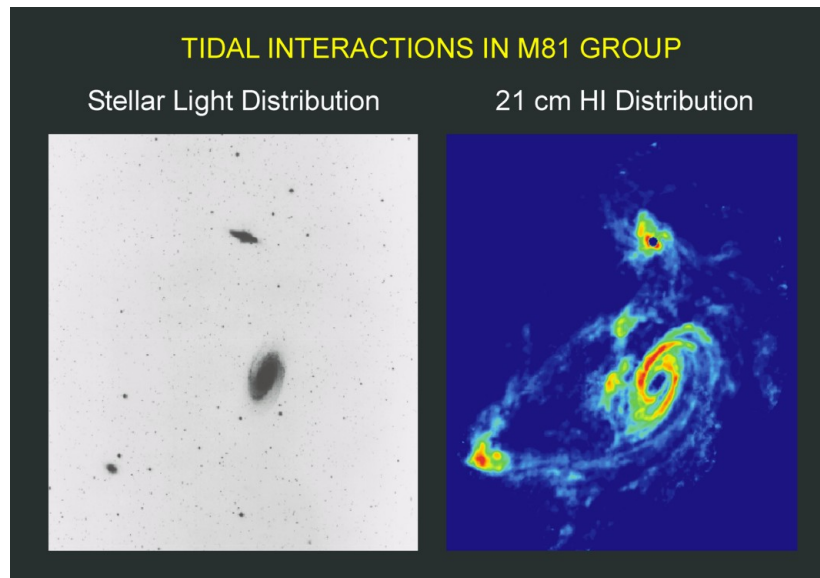


Figure 2.5: **Left panel:** visible-light image of the M81 Group of galaxies (from the Digital Sky Survey), shown in a reversed grey-scale (dark regions are brighter). Most of the light in this image comes from stars in the galaxies. **Right panel:** a radio image, made with the VLA, shows the hydrogen gas, including streamers of gas connecting the galaxies. From the radio image, it becomes apparent that this is an interacting group of galaxies, not isolated objects (adapted from NRAO Gallery <http://images.nrao.edu/116>).

the IGM is a key factor for any theory of structure formation and evolution for a number of theoretical reasons.

First, the presence of metals traces the stellar nucleosynthesis and evolution: metals are in fact produced inside the stars and then expelled through core collapse SNe or released when intermediate mass stars explode as type Ia SNe. Observations of metals in dense regions where the stellar nucleosynthesis is active, provide then a record of the star formation history. Further, the pollution of the ISM gas resulting from supernovae explosions and AGB star winds, affects the successive generations of stars because their initial mass function (IMF) depends on the chemical composition of the environment in which they form.

Second, the metals in the IGM act as marker of the efficiency of feedback processes [50] (see Figure 2.3 for an example of feedback impacting star formation). Observations of metals far from the galaxies show signatures of the galactic winds efficiency, which gives hints about the velocity structure of the IGM ([101, 39, 85, 148]). The presence of metal ions traces the physical state of the gas and constraints the radiation background permeating the gas via radiative feedback. Finally, the gas metallicity produces a direct feedback on the gas cooling function, directly affecting the galaxy formation process ([251, 214, 215]).

Furthermore, the IGM metallicity evolution with redshift places constraints on various plausible enrichment histories ([217]): e.g. an early enrichment by the first generation of

stars [148] and galaxies, a continuous enrichment active during the epoch of cosmic Re-ionisation ([101, 85, 219]), or a late enrichment, coinciding with the star formation peak at $z \sim 2 - 4$ [1].

In the more general context of the structure formation theory, the determination of the metal abundances at various redshifts could also place constraints on the change in the efficiency of the gas cooling function [251, 153, 235, 280], on the collapsing rate of the gas, and on the formation of massive galaxies [258].

2.2.1 Observational constraints

A large set of information about the physical properties of the IGM can be obtained using the metal lines in the spectra of quasars (see Figure 2.1). The widths of the metal absorption lines are directly related to the IGM temperature and then to its small scale velocity structures, because metals remain confined around the galaxies. The narrow widths of C IV have shown that the gas is dominated by photo-ionisation rather than collisional ionisation (see [71] for a recent treatment of these physical processes including metallicity effects). To add more constraints to the spectral shape of the meta-galactic ionising UV background, we can use metal column density ratios as indicated for the helium Ly α forest (see 5). The absorption profiles of metal lines which are not too saturated, give information on the kinematics of the gas in high redshift galaxies.

During the last decade, observational and theoretical studies constraining the nature of the Intergalactic Medium have shown that metals are a pervasive component of the baryonic budget of our Universe and that they are associated with a wide range of hydrogen column density systems at different redshifts ([169, 146, 240, 56, 74, 225, 223, 10, 195, 18]). DLAs and LLSs show C IV lines as well as many low ions (Mn II, Si II, Fe II), and are typically associated to metallicity of $Z = 10^{-2}Z_{\odot}$ (LLSs; e.g. [249]) and $10^{-2}Z_{\odot} \leq Z \leq 0.3Z_{\odot}$ (DLAs; e.g. [118, 205, 194, 139, 249]). The presence of metals in LLSs and DLAs can be interpreted as natural product of the stellar nucleosynthesis acting therein; LLSs are in fact identified as clouds in the galactic halos while high redshift DLAs ($z \sim 3$) are believed to be the progenitors of the present-day galaxies.

Advances in high resolution spectroscopy revealed that clouds in the Ly α forest can also be associated with weak C IV absorption lines. Ions of C IV are in fact detected in most of the clouds with $N_{\text{HI}} \geq 10^{15} \text{cm}^{-2}$ and in more than half of the systems with $N_{\text{HI}} \geq 10^{14} \text{cm}^{-2}$ ([268, 240]). These systems represent the tenuous IGM and are interpreted as part of the filamentary component of the cosmic web connecting collapsed objects; their estimated metallicity ranges in $10^{-4}Z_{\odot} \leq Z \leq 10^{-2}Z_{\odot}$ ([233]). The subsequent discovery of a metallic component in less dense regions ([56, 225, 74, 223, 10, 195]) can be interpreted instead as the evidence of efficient feedback processes involving the tenuous and ultra thin IGM. Figure 2.6 (left panel) summarises the observed metallicity as function of various systems [89].

Observational evidence of some redshift evolution of the metallicity has also been extensively investigated. In the redshift range $1.5 < z < 4$, C IV and Si IV doublets are the main tracers of the IGM metallicity because their rest-frame wavelength is greater

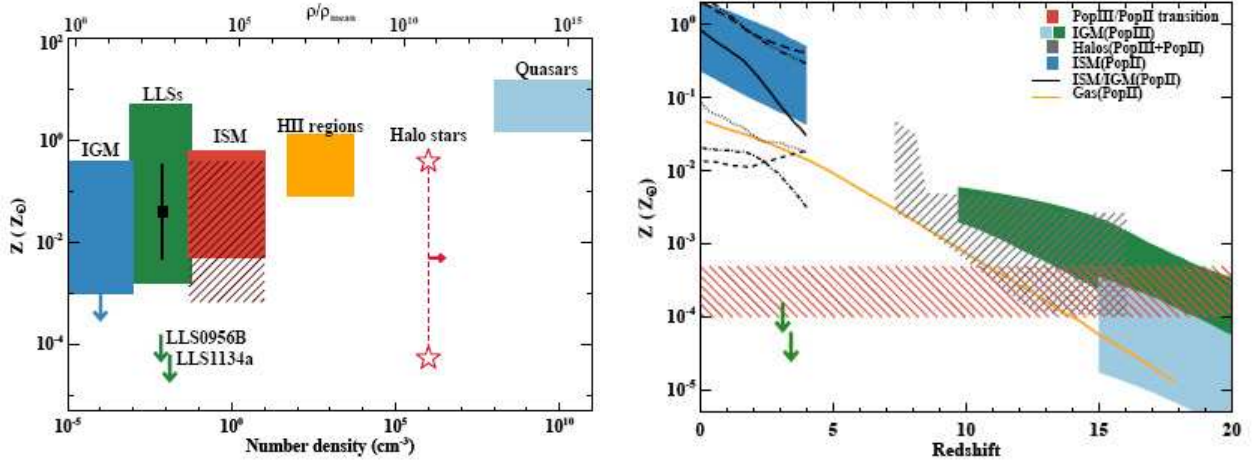


Figure 2.6: **Left panel:** peak to peak variation of the observed metallicity in $z \gtrsim 2$ cosmic structures at different densities. The blue (IGM), green (LLSs) and red (ISM) rectangles show the spread in observed metallicity for diffuse gas in the Universe. Orange rectangle: HII regions in galaxies. Light blue rectangle: quasar broad line regions. The black point with error bars marks the mean metallicity and the standard deviation for $z > 1.5$ LLSs. Galactic halo stars (stars connected with a dashed line) are represented at arbitrary density for visualization purposes. The top axis translates the number density in the over-density above the mean baryon cosmic density at $z = 3.5$. **Right panel:** overview of analytic models and simulations for the metal enrichment of the Universe. Light blue and green shaded regions: IGM metallicity from PopIII stars with different mixing strength and different star formation histories (10,21 in [89]). Red dashed region: critical metallicity that marks the transition between PopIII and PopII stars (23, 33 in [89]). Orange line: analytic model for the gas metal content in the Universe from PopII stars and galactic winds (20 in [89]). Gray shaded region: gas metallicity within halos from hydrodynamical simulations that include yields from both PopIII and PopII stars (22 in [89]). Blue shaded region: analytic model for the ISM metallicity at different halo masses ($10^{11} - 10^{14} M_{\odot}$) and different wind models (34 in [89]). Black lines: metallicity from hydrodynamical simulations with momentum driven winds (19 in [89]) in condensed gas (solid line), hot halo (dotted line), warm-hot intergalactic medium (dashed line), diffuse gas (dash-dotted line), ISM (dash-triple-dotted line), and stars (long-dashed line). Upper limits on the metallicity of LLS1134a and LLS0956B are marked with green arrows. (Figures adapted from [89]).

than the Ly α and the lines cannot be confused with the forest. In this range the column density distribution of C IV seems to remain constant ([239]). The O VI lines can be used to place constraints in the metallicity of the tenuous IGM typically of the order of $Z < 10^{-3}Z_{\odot}$ at redshift $z < 3$ ([205, 56, 38]). This line is a promising tool to detect the warm-hot IGM that should host a large fraction of the cosmic baryons in the low redshift Universe where O VI is the most commonly observed metal line. Tripp et al. [267] have demonstrated that the O VI can be an excellent tracer of baryons in galaxies at $z < 0.5$. Danforth and Shull [59, 61] estimated that 10 percent of the total baryons in the WHIM could be revealed by the lines of O VI. Early investigations into O VI using cosmological simulations ([39, 76, 48, 40]) predicted that stronger O VI absorbers tend to be collisionally ionised while weaker ones tend to be photo-ionised; on the other hand, recent surveys have provided additional controversies about the nature of O VI absorbers. Unified theoretical models have been proposed by many authors ([117, 96]), however, observations remain inconclusive as to whether this scenario could apply ([61, 60]) or to which cosmic gas and metal phases the O VI absorbers actually trace.

Although the determination of the IGM metallicity is traditionally linked to the large set of QSOs in the redshift range $z \sim [4-3]$, new set of data have recently become available up to $z \sim 6$. Although a consensus has not been reached yet, a decline in the abundance of C IV above $z \sim 4.5$ is reported by different groups ([17, 18, 210]).

At high redshifts ($z > 5$) star forming galaxies have been shown to interact with the surrounding medium by powering strong galactic outflows [1].

Many observational data about the IGM metallicity remain then controversial as well as their interpretation; these observations are instead of primary importance e.g. in constraining the history of the metal enrichment process and, up to the present, many enrichment scenarios are still possible. The metal abundance, the number of their ionised states and the distribution in space and over the redshift are in fact still subject of intense debate (see [192, 193, 59, 61, 60]), while an inhomogeneous enrichment seems now to be more realistic than a simplistic uniform metal distribution parametrized as function of the gas over-density at the galaxy proximities ([1, 197, 196]). Also the sources of enrichment are basically unknown: the IGM may have been enriched by the first generations of dwarf galaxies at very high redshifts, or it may have been polluted by more massive galaxies at intermediate redshifts. Scenarios based on early pollution from the first generation of massive stars (POP III, see [50]) seem extremely inefficient because they do not suffer strong stellar winds; wind-mass loss is in fact metallicity-dependent with a scaling law $\propto Z^{1/2}$ that breaks down at $Z < 10^{-2}Z_{\odot}$, where the power-law becomes steeper ([138]). The main contribution to the IGM metal enrichment seems to come then, from those stars that end up their lives as Pair Instability Supernova (PISN) and core-collapse SNe (see [50]).

Recent direct observations of outflows in many local starburst galaxies and Lyman Break Galaxies (LBGs) ([115, 116, 229, 156, 270]) can provide more insights on feedback processes than the metal dispersal information taken from QSOs absorption line spectroscopy. Starburst winds could naturally account for a high-redshift episode of metal enrichment when the characteristic mass of galaxies is small (see Figure 2.4).

2.2.2 Theoretical models of metal enrichment

Many physical mechanisms have been implemented in theoretical models to reproduce the IGM metallicity. To simulate the metal production, we first need to know the star formation rate, usually implemented by using the Schmidt law:

$$\text{SFR} \propto \rho^{3/2}, \quad (2.4)$$

where ρ is the gas density and SFR is normalized with the observations ([131]). If gas is producing stars, the rate of metal production (\dot{M}_Z) [246] is commonly implemented as:

$$\dot{M}_Z = y \cdot \text{SFR}, \quad (2.5)$$

where y is the metal yield provided by the IMF and the models of stellar evolution ([144], [218]).

To justify the presence of metals far from their production sites, many candidate feedback mechanisms have been implemented in both hydro and semi-analytic models. Winds driven by supernovae, from star-forming galaxies or AGN can provide an effective removal mechanism (see Figures 2.3, 2.4, 2.5). On the other hand, winds do not seem sufficient to pollute the large scales of the observed IGM ([85, 5]) and so, once the metals are dispersed in the galaxy neighbourhoods, other processes as the ram-pressure stripping or the tidal stripping could be responsible for the spread of the heavy elements on the ICM scales. Galaxy mergers could also be responsible for effective mixing on IGM scales, as pointed out in [100].

The first attempt to reproduce the observed properties of the most common metal ion at low redshifts (C IV) by using hydrodynamic simulations, has been made by Haehnelt et al. [112]. Subsequent numerical studies ([261, 42, 184, 185]) have demonstrated that an accurate implementation of feedback in the form of galactic winds is a key ingredient to reproduce the metal line statistics. In recent years such mechanisms, previously implemented to simulate the details of single galaxy physics ([203, 19, 129, 130, 102]) or the ICM ([264, 263, 33]), have been ported to large chemodynamical cosmological simulations ([178, 133, 184, 185, 282, 265, 256]).

The first implementation of global metal enrichment into a Smoothed Particle Hydrodynamics (SPH) code ([250]) did not distinguish between different elements and included just core collapse SNe in the instantaneous recycling approximation; more sophisticated recipes for chemodynamics are now available in current implementations ([203, 178, 129, 143, 142, 130, 209, 213, 153, 185, 265]), also distinguishing between individual elements released by AGB stars, SNe Ia, SNe II, and the winds from their progenitors. Nowadays several numerical schemes, particle or grid based, include metal production and spreading and can predict their impact on the chemical evolution of the IGM ([184, 72, 282, 224, 279, 281, 151, 265, 154, 65]). The different implementations of the many feedback processes introduced before, are still under scrutiny in comparison projects (e.g. the AQUILA project [216]) in order to establish their effects on the galaxy formation. In the following Paragraphs I will briefly review these mechanisms.

Galactic Winds Although detailed numerical simulations of galactic winds are continuously improving ([147, 176, 175]), the study of the metal pollution by galactic winds is still based on 'had hoc' assumptions because many pieces of the basic physics driving these outflows are still missing. Many key questions about the physical nature of these winds still remain unanswered: how much galactic mass is involved, what fraction of the initial energy is spent in mechanical or radiative processes, and more importantly, if a single wind recipe at all the redshifts exists.

Semi-analytical methods try to solve all these problems by spanning many input parameters [95] with relatively little computation, on the other hand their treatment is not self-consistent because they need to pre-assume the physical state of the medium to set up their initial conditions. ([223, 67, 23, 24, 220, 22]).

Despite the fact that the first modelling of the observed distributions of metal absorbers ([45]) was able to account for the number of O VI systems without including super-winds, to reproduce the low- z ion distribution [59, 61], a detailed and self-consistent wind implementation is necessary. The super-wind feedback implementation in SPH by Springel and Hernquist [245, 246] is referred to in the scientific literature as energy-driven wind. In the model the wind mass-loss rate \dot{M}_{wind} is assumed to be proportional to the star formation rate SFR:

$$\dot{M}_{wind} \propto \eta \cdot \text{SFR}, \quad (2.6)$$

where η indicates the mass-loading factor and it is considered as a free parameter of the model. There are two main free parameters in this model: the wind speed v_{wind} and the mass-loading factor η . The authors of the model decided to use constant values for both parameters, as constrained by outbursts observations at low redshifts; with this choice they were able to obtain a stellar mass density at $z = 0$ in broad agreement with observations.

The application of this prescription at small, high redshift galaxies, results instead in a heating excess of the IGM by $z = 3$ to agree with C IV observations and in an excess of enrichment in high resolution simulations which can account for the contribution of the small galaxies at earlier times.

Another scheme of galactic wind, triggered by supernovae (SN) explosions and AGNs, has then been implemented in the most recent large-scale simulations ([184, 257]): the momentum-driven, or radiation pressure-driven, wind.

For momentum-driven winds ([179, 262]), the radiation pressure of the starburst drives the outflow, transfers momentum to dust, which acts as radiation absorber and then couples to the bulk of the outflowing material. In this model the wind speed scales as the galaxy velocity dispersion (as observed by Martin [155]) and the amount of input momentum per unit star formation is constant, so that the mass-loading factor must be inversely proportional to the velocity dispersion σ of the galaxy:

$$\dot{M}_{wind} \propto \frac{\text{SFR}}{\sigma}. \quad (2.7)$$

An advantage of momentum driven winds is that, unlike heat, momentum cannot be radiated away, and hence can plausibly drive winds over large distances. These winds may

suffice to explain the statistics of the IGM enrichment ([179]). Many groups ([184, 185]) implemented this model in cosmological simulations finding that with this scheme it is easy to reproduce the statistics of C IV absorption in the high-redshift IGM, better than using the energy-driven winds.

Ram-pressure stripping in clusters and galaxy mergers In dense environments such as groups and clusters of galaxies the ICM exerts a ram-pressure on their members as they move along their orbits. This effect can be sufficiently strong to strip the ISM from the galaxies, and thus mixing the elements in the ISM of the group components, also creating a (re-)cycling of elements over time through stars, galaxies and diffuse gas (see Figures 2.3 and 2.5). On the other hand, these mechanisms seem to have a minor impact on the overall metallicity and filling factor on the IGM scale, as it occurs only in the densest and most polluted regions of space ([219]).

Events of galaxy mergers, where the ISM of the interacting galaxies can be affected by dynamical stripping, can be a favourable mechanisms for the large-scale IGM enrichment. Gnedin ([100]) found that the IGM could be enriched to the observed levels by these mergers because the strong interactions in merger events can efficiently remove enough metals to reproduce the highly inhomogeneous distribution of observed metals.

Dust sputtering Primordial dust could play a key role in the enrichment of the early IGM. Ejection of dust grains by radiation pressure, and successive sputtering, have been suggested by Ferrara et al. [84]. Unlike winds, this mechanism has a minimal impact on the thermal and structural properties of the IGM and does not require shock-waves. Despite the fact that dust pollution can account for the C and Si enrichment at $z = 3$, it fails in reproducing all the chemical species observed in clusters at low redshifts and the efficiency of the sputtering processes in the IGM has to be demonstrated.

Figure 2.6 (right panel) summarises the contribution of the various semi-analytic and numerical works in matching the metallicity observations. Contributions from models including POPIII and different star formation histories, transitions from POPIII and POPII stars, as well as hydrodynamical simulations with winds are included. A clear separation from galactic (ISM) and extragalactic gas metallicity is marked at $Z \sim 0.1Z_{\odot}$.

2.2.3 Theoretical models of metal ionisation

Once the metal pollution has been accounted for in the structure formation simulations, the interpretation of the metal ionised states accessible to the observations to infer the gas properties requires theoretical models for the radiation field maintaining the observed ions. A commonly adopted approach consists in avoiding to solve the full radiative transfer problem and using a simplified model for the UV background. The assumed radiation is then used as energetic input for photo-ionisation codes which compute the metal ionisation states ([184, 186]).

The results of this approach are affected by the uncertainties associated to the assumptions on the shape and intensity of the radiation field, which typically is not calculated self-consistently through a radiative transfer across the inhomogeneous gas distribution. Many studies suggest in fact that the radiative transfer effects of shadowing, filtering and self-shielding induce deviations in the shape and intensity of the background with respect to models in which the effects of the radiative transfer are neglected ([158] and references therein). Fluctuations in the photo-ionisation rates as well as spatial deviations in the IGM temperature due to the inhomogeneity of the cosmic web support this view at least on scales of few comoving Mpc (see [158, 90, 167] and references therein). On large scales of about $100h^{-1}$ Mpc comoving, the QSO spatial distribution and their spectral index variability could be an additional cause of variations in the background ionising field ([166, 295, 296]) below $z \sim 4$.

These fluctuations induced by the radiative transfer could be efficiently recorded in the ionisation balance of the metals because they have a rich electronic structure and their atomic spectrum is more sensitive to the radiation field fluctuations than e.g. hydrogen ([182, 95, 90]).

Numerical schemes which solve the cosmological radiative transfer equation by applying different approximations are now quite mature and well tested ([124, 126] and references therein for an overview of the available codes) and are able to simulate complex scenarios involving large cosmological boxes and number of sources (ex. [125, 266, 162, 54, 52, 11]). Typically these codes are restricted to the hydrogen chemistry, with only a few of them including a self-consistent treatment of the helium component, which is particularly relevant for a correct determination of the gas temperature (see e.g. [49]). None of them though includes the treatment of metal species.

In the ISM community, on the other hand, several photo-ionisation codes are able to simulate the complex physics of galactic HII regions, with great deal of attention to the details of the underlying physics (see [191] for a review). For example, `Cloudy` [83] and `MAPPINGS III` [9] are two codes particularly accurate in simulating the complex physics of the galactic regions largely polluted by heavy atoms and dust grains. At each cosmic scale, the physical properties of the gas (density, temperature) can be derived from the observed ion abundances only under specific assumptions about the spectrum of the radiation field that maintains their ionisation equilibrium; it is then of primary importance to have accurate theoretical models reconstructing the shape and intensity of the cosmic UV background as well as the physics of gas photo-ionisation in astrophysical environments. In the following Chapters I will treat in detail the problem of the radiative feedback on cosmological scales with specific emphasis on the cosmological radiative transfer code `CRASH`.

Chapter 3

Radiative transfer with CRASH

In this Chapter the radiative transfer problem is introduced in the context of the Re-ionisation history of the Universe and it is addressed in its general formalism in Section 3.2. The radiative transfer code **CRASH** is then introduced in Section 3.3 and it is described in its algorithm and in the new software implementation.

3.1 Ionisation

In Astrophysics many environments can be described in term of gas embedded in the radiation emitted by nearby sources: star forming regions, HII regions, Interstellar Medium and Intergalactic Medium, are just few examples. UV photons with energies $E \geq 13.6$ eV emitted by the sources ionise the neutral hydrogen and helium composing the gas mixture of these environments. Assuming a neutral gas of number density $n_{\text{gas}} [\text{cm}^{-3}]$ composed by hydrogen and helium, the evolution of the physical state of the gas is described in terms of the following equations:

$$\begin{aligned}
 n_{\text{H}} \dot{x}_{\text{HII}} &= \gamma_{\text{HI}}(T) n_{\text{HI}} n_e - \alpha_{\text{HII}}(T) n_{\text{HII}} n_e + \Gamma_{\text{HI}} n_{\text{HI}} \\
 n_{\text{He}} \dot{x}_{\text{HeII}} &= \gamma_{\text{HeI}}(T) n_{\text{HeI}} n_e - \gamma_{\text{HeII}}(T) n_{\text{HeII}} n_e - \alpha_{\text{HeII}}(T) n_{\text{HeII}} n_e + \\
 &\quad \alpha_{\text{HeIII}}(T) n_{\text{HeIII}} n_e + \Gamma_{\text{HeI}} n_{\text{HeI}} \\
 n_{\text{He}} \dot{x}_{\text{HeIII}} &= \gamma_{\text{HeII}}(T) n_{\text{HeII}} n_e - \alpha_{\text{HeIII}}(T) n_{\text{HeIII}} n_e + \Gamma_{\text{HeII}} n_{\text{HeII}} \\
 \dot{T} &= \frac{2}{3k_B p} [k_B T \dot{p} + \mathcal{H}(T, x_A) - \Lambda(T, x_A)]
 \end{aligned} \tag{3.1}$$

where T is the gas temperature and the hydrogen and helium ionisation fractions are defined as $x_{\text{HII}} \equiv n_{\text{HII}}/n_{\text{H}}$, $x_{\text{HeII}} \equiv n_{\text{HeII}}/n_{\text{He}}$ and $x_{\text{HeIII}} \equiv n_{\text{HeIII}}/n_{\text{He}}$. Here n_i is the number density of species $i \in \{\text{H}, \text{H II}, \text{He}, \text{He II}, \text{He III}\}$, with $n_{\text{H}} = f_{\text{H}} n_{\text{gas}}$ and $n_{\text{He}} = f_{\text{He}} n_{\text{gas}}$, while f_{H} (f_{He}) is the fraction of H (He) in number. In the above equations, $\alpha_I(T)$ are the gas recombination coefficients for each species ($I \in \{\text{H II}, \text{He II}, \text{He III}\}$) and $\gamma_A(T)$ are the coefficients of the collisional ionisation processes ($A \in \{\text{H I}, \text{He I}, \text{He II}\}$). Γ_A defines the time dependent photo-ionisation rate. In the last equation, describing the energy balance

of the system, p is the number of the free particles per unit volume present in the gas and \mathcal{H} and Λ are respectively the gas heating and the cooling functions. Hereafter I will consider the gas in steady state or, equivalently, the time scales of the atomic processes can be considered much faster than the dynamical time scales. In this case, the physical processes which determine Λ include recombination radiation, free-free emission and collisionally excited line radiation. An accurate treatment of such processes can be found in [71]. On a cosmological scale, the cooling function also depends on the redshift z because of the Compton cooling due to the CMB background.

The photo-ionisation process depends on the UV radiation field intensity and shape, as described by the definition:

$$\Gamma_A(t) = \int_{\nu_A}^{\infty} \sigma_A(\nu) \frac{cu_\nu(t)}{h\nu} d\nu, \quad (3.2)$$

where $\sigma_A(\nu)$ is the frequency dependent cross section of the species A, as established by the non relativistic description of the quantum mechanical spectrum of their ions; ν_A indicates the resonant frequency for the photo-ionisation, and the quantity $u_\nu d\nu$ is the energy density of the radiation in the frequency interval $[\nu, \nu + d\nu]$.

If the dominant ionisation mechanism is photo-ionisation, it is found that the typical temperatures are in the range $T = (1 \cdot 10^4 - 5 \cdot 10^4)$ [K]. On the other hand, if shock heating is present, temperatures exceeding 10^6 K can be reached and the ionisation balance is dominated by the atomic collisions.

3.2 Radiative transfer

In its general formulation, the radiative transfer describes the evolution in time and space of the 4-dimensional Stokes vector associated to an electromagnetic field propagating through a generic medium [46, 170]. Let $\vec{r}, \vec{\Omega}$ represent the radial and solid-angular coordinates of the radiation propagation in space, and ν the value of the photon frequency. If the polarization of the radiation can be neglected, the radiative transfer equation is only described in terms of the radiation intensity component I , commonly defined in terms of the photon distribution function $\zeta(\vec{r}, \nu, \vec{\Omega}, t)$ as:

$$I(\vec{r}, \nu, \vec{\Omega}, t) = ch\nu\zeta, \quad (3.3)$$

where c is the speed of light and h the Planck constant.

The integro-differential equation describing the spatial and temporal evolution of I can be written as:

$$\frac{1}{c} \frac{\partial I}{\partial t} + \vec{\Omega} \cdot \vec{\nabla} I = \epsilon - \kappa I, \quad (3.4)$$

where $\epsilon(\nu)$ is the function characterizing every photon emission process and the term $\kappa(\nu)$ describes every frequency dependent process that absorbs or removes photons by interaction with the atoms of the medium. Because scattering events depend on the integrated

spatial and frequency variables $(\nu, \vec{\Omega})$, these terms also contain an implicit integral over space coordinates and frequencies. The transfer of radiation is then an integro-differential mathematical problem. Hereafter I will neglect the scattering effects, the reader interested in the complex mathematical formalisms of the radiation hydrodynamics including the scattering, can find a modern and extensive treatment in [200, 252].

The first and second terms on the left-hand side of the equation describe the temporal and spatial evolution of the radiation intensity, respectively; while the right-hand side contains all the events adding or removing photons along the direction of propagation.

The radiative transfer equation can be interpreted also as rate equation describing the conservation of the total number of photons crossing the medium as function of time. In terms of this micro-physical description, the mathematical formulation can be rephrased considering the evolution in time of the statistical photon distribution function ζ . If we can simulate the propagation of a large number of photons emitted by sources and propagating through the medium, the distribution function ζ can be statistically reproduced. Every time a photon of frequency ν is emitted by a source, it travels along a straight line of length l (also referred to as mean free path), before interacting with the gas. At each interaction the photon can experience an absorption event as prescribed in the term $\kappa(\nu)$.

In Cosmology, the end of the Dark Ages is marked by the birth of the first stars, the consequent emission of ionising photons and their propagation through the neutral IGM. When photons travel on cosmological scales, the finite speed of light and the Universe expansion impose a change in the radiative transfer equation. First we can not assume the medium as static with respect to the typical crossing time of the light; second the Universe expansion imposes a shift in the frequency of the travelling photons. Defining with $a(t)$ the expansion scale factor (see Equation 1.1 and the formal derivation in the Introduction), the frequency redshift requires $\nu \propto a(t)^{-1}$ (see Equation 1.3) and it can be shown that the radiative transfer equation becomes [167]:

$$\frac{1}{c} \frac{\partial I}{\partial t} + \frac{1}{c} \frac{1}{a} \frac{\partial a}{\partial t} \left[3I - \nu \frac{\partial I}{\partial \nu} \right] + \vec{\Omega} \cdot \vec{\nabla} I = \epsilon - \kappa I \quad (3.5)$$

where the new terms account for the Universe expansion and the Doppler redshift of the travelling photons.

An atomic absorption event is modelled as the removal of the photon at the interaction location and the release of the photon energy $E_\nu = h\nu$ to the interacting atom, which is left in an excited or ionised state. The absorption process probability depends on the atom cross section $\sigma(\nu)$, the photon frequency and the number density of atoms n , found along the propagating direction between two interaction events. The photon mean free path l between two absorptions can then be defined as:

$$l = (n\sigma)^{-1}. \quad (3.6)$$

Another common way of describing the absorption event is in terms of the gas optical depth τ along a travelling distance s :

$$\tau(s) = \int_0^s \sigma n(s') ds'. \quad (3.7)$$

If the medium has constant density

$$\tau = \sigma n s = s/l, \quad (3.8)$$

and the optical depth can be thought as the number of mean free paths travelled by the photon along the distance s .

From a mathematical point of view, the RT equation is a challenging multi-dimensional problem that can be solved analytically only with simplifying assumptions. A typical case is when a geometrical symmetry is present, which allows to simplify the term $\vec{\Omega} \cdot \vec{\nabla} I$. Similarly, if steady state of I can be assumed, the first term in equation 3.4 is equal to zero, making its solution a much easier problem.

The increasing computational power provided by modern supercomputers has facilitated the development of software codes solving the radiative transfer problem by using numerical techniques. The Cosmological Radiative Transfer Comparison Project ([124, 126]) is a scientific collaboration effort between groups around the world, offering the opportunity to compare the results of different numerical techniques applied to the same set of physical problems that require radiative transfer. The RT codes involved in the comparison use different approximations, mostly based on various versions of ray tracing or moment schemes. In the ray tracing approach the radiative flux is simulated tracing rays from the emitting sources, and following the photon propagation on a discretized domain. The transfer calculation can be done by adopting short characteristics, discretized long beams, ray-splitting techniques or randomly sampling the emission directions. The domain discretization is commonly done on fixed or adaptive grid, but implementations of unstructured Lagrangian grids are also available. The frequency dependence can be simulated by using a large number of monochromatic photons, or collections of comoving photons distributed according the spectral distribution of the emitter (photon packets). The treatment of the diffuse radiation produced by the gas reemission can be included by slight modifications of the same methods.

In the moment formalism, a simplified, low order (diffusive) approximation of the intensity field is used to describe the radiation field and to significantly speed up the calculation.

The adoption of one scheme with respect to another is mostly dictated by the physical problem under investigation and the different approximations it requires: authors interested in accounting for the feedback between RT and gas dynamics, normally adopt a simplified RT scheme to reduce the computational time; on the other hand, if the details of the RT must be reproduced and a steady state for the gas can be assumed, the MC scheme generally results more suitable. More details about the codes and their mathematical methods can be found in the Cosmological Radiative Transfer Comparison Project papers and the references therein. Hereafter I will concentrate on the Monte Carlo method used in my PhD thesis.

3.2.1 A Monte Carlo approach to the radiative transfer problem

The Monte Carlo (MC) technique [236] is based on the statistical sampling of given distribution functions. In RT problems these functions describe for example the emission,

propagation and absorption probability of photons.

Once a photon has been emitted with a direction and frequency randomly chosen from the appropriate distribution functions, the algorithm follows the propagation of the photon. When an absorption event occurs, the set of Equation 3.1 is solved and the physical configuration of the medium is updated. By simulating a very large number of photon emissions and propagation, the physical evolution of the radiation intensity I can be evaluated in each point of the domain and at every time with high accuracy. The number of photon emissions is set by the requirement of a convergent solution with a given precision. While this often results in a large computational time, the adoption of a Monte Carlo scheme provides many advantages in terms of software implementation, mainly because of its flexibility [140]. MC codes in fact offer the possibility to treat the RT at the scale of the single photon propagation and interaction, allowing for an accurate implementation of the radiation-to-matter micro-physics. Moreover, the MC codes can be easily scaled in performance with the increasing computational power provided by parallel supercomputing facilities, attenuating the high computational cost required by an accurate sampling of the distribution functions [107, 188].

The success of the MC numerical scheme is also proven by the large number of scientific communities adopting this method for a wide variety of problems. In astrophysics the MC scheme is widely used to solve the radiative transfer problem at every scale and in many different environments. In stellar physics an accurate RT is essential to simulate the emission spectra and the convection dynamics of the upper layers of the stars. In the ISM, the understanding of the energy irradiated by the stars is crucial to solve the complex chemistry regulating the formation and survival of dust and molecules. At the same scale, the radiative processes play a central role in the theory of the star formation, planet formation in protoplanetary discs and the low temperature physics of the molecular clouds. On galactic scales, an accurate RT treatment in dusty media is crucial to establish the global temperature structure of the galaxies, the effects on radiation escape fraction and the global stability of galactic discs [103].

In the following Sections I will describe the cosmological radiative transfer code CRASH [51, 159, 157].

3.3 The CRASH code

CRASH is a 3D radiative transfer code designed to follow the propagation of photons with energy $E \geq 13.6\text{eV}$ through a gas composed by H and He. The code adopts a combination of ray tracing and Monte Carlo sampling techniques to propagate photon packets through an arbitrary gas distribution mapped on a cartesian grid, and to follow, in each grid cell, the time evolution of gas ionisation and temperature. This treatment guarantees a reliable description of such evolution in a large variety of configurations as shown in the Cosmological Radiative Transfer Comparison Project tests [124], and its various applications to the study of the H and He Re-ionisation ([54, 52, 49]), the imprints of the fluctuating background on the Ly α forest [158] and the quasar proximity effects [159].

The MC algorithm adopted allows to easily add new physical processes. In its first version ([51]) the code describes the photo-ionisation due to point sources, and includes the effect of reemission following gas recombination. The subsequent versions brought about significant improvements. First the physics of He and the thermal evolution of the gas have been introduced, together with the treatment of an ionising background field ([159, 158]). In the latest release ([157]), multi-frequency photon packets were introduced, obtaining a significant improvement in terms of accuracy of the ionisation and temperature profiles, as well as computational speed. Hereafter the code name CRASH will refer to its latest update CRASH3 (see Chapter 4). In parallel with the reference code, variants and extensions have been developed such as: MCLy α ([271]), which has adapted the reference algorithm to treat the resonant propagation of Ly α photons; CRASH α ([198, 199]), which follows the self-consistent propagation of both Ly α and ionising continuum radiation; ([188]) have instead developed an MPI parallel implementation of the base CRASH2 algorithm.

3.3.1 CRASH work-flow

CRASH solves the cosmological radiative transfer problem post processing a gas density distribution in a box of linear size L_b . The domain is discretized on a fixed regular cartesian grid of N_c^3 cells and the hydrogen and helium number densities (n_H , n_{He}), the temperature (T) and ionisation fractions (x_{HII} , x_{HeII} , x_{HeIII}) at the simulation initial time t_0 are assigned on the same grid. A certain number of ionising point sources N_s is also specified by their positions in cartesian coordinates, luminosity (L_s in erg s^{-1}) and spectral energy distribution (SED; S_s in $\text{erg s}^{-1} \text{Hz}^{-1}$). The presence of a uniform UV background can also be superposed to the point source distribution by assigning its intensity and spectral energy distribution in the entire domain. The RT simulation is specified by a temporal duration t_f and by a given set of intermediate times $t_j \in \{t_0, \dots, t_f\}$ needed to store the values of the relevant physical quantities.

The simulation run consists in emitting a fixed number N_p of photon packets (defined as collection of photons distributed accordingly to the emitter's SED) from the ionising sources and following their propagation through the domain. Each photon packet keeps travelling and depositing ionising photons in the crossed cells, as far as its content in photons is completely extinguished or it escapes from the simulated box (although periodic boundary conditions in the packets propagation are possible).

At each cell crossing, CRASH simulates the radiation-to-gas interaction by evaluating the absorption probability for a single photon packet as:

$$P(\tau) = 1 - e^{-\tau}, \quad (3.9)$$

where τ is the total gas optical depth of the cell given by the sum of the contributions from the different species, i.e. $\tau = \tau_{\text{HI}} + \tau_{\text{HeI}} + \tau_{\text{HeII}}$. Inside each cell the number densities are constant and the formula 3.8 applies; the single components of the total optical depth are then evaluated as: $\tau_A = n_A \sigma_A s_c$, where s_c is the path casted within the cell as defined in [159], Equation 9.

The number of photons absorbed in the cell can then be estimated as:

$$N_\gamma (1 - e^{-\tau}) \quad (3.10)$$

where N_γ indicates the photon content of a packet entering the cell.

The photons deposited for each frequency are used to compute the contribution of photo-ionisation and photo-heating to the evolution of x_{HII} , x_{HeII} , x_{HeIII} and T . The code then solves the set of ionisation and energy conservation equations described in the previous Section ([159, 157]) at each cell crossing event and dynamically updates the physical state of the medium during the photon propagation.

The evolution of the thermal state of the gas is established with the last formula in 3.1 evaluating the heating and cooling functions \mathcal{H} and Λ . The heating is determined by computing the photo-heating released in the cell, while the Λ is calculated by adding up the contribution of various radiative processes: collisional ionisation and excitation, recombinations, Bremsstrahlung and Compton cooling. Differently from photo-heating, these processes are treated as continuous processes, described by the respective rates (see [159] for details).

When dealing with cosmological problems (e.g. Re-ionisation simulations), the evolution of every physical quantity depending on the redshift must be accounted for (see discussion in 3.1.1 and Equation 3.5). In the current version of CRASH the redshift evolution of the ionisation process is obtained joining a series of snapshots (gas density and source configurations) at successive redshifts z_i . In each snapshot the redshift evolution is calculated during the RT duration time t_f and the box is expanded according to the cosmological expansion law. Between two snapshots the gas number density is evolved as $n_c(z) = n_c(z_i)(1+z)^3/(1+z_i)^3$, where $z_i > z > z_{i+1}$ and the initial conditions for each step are self-consistently established by the results of the previous one. The global set of $f \times i_{max}$ outputs (where i_{max} is the maximum value of the index i) provides the cosmological evolution of the hydrogen and helium ionisation fractions and of the gas temperature, so that the Universe Re-ionisation history is finally reconstructed. It is important to notice that the CRASH work-flow solves the cosmological radiative transfer by neglecting the effects of the radiation feedback on the gas dynamics.

During the first part of my PhD project I have substantially modified the CRASH software implementation enhancing the code performances and introducing software modularity, as detailed in the next Sections. Once the software modularization has been implemented correctly, I have extended the algorithm adding new physics without impacting the global performances: cosmological Doppler shift, gas clumping factor and the modelling of source populations have been added to the main RT algorithm discussed above.

To handle the big scales required by the Re-ionisation, the cosmological Doppler shift for the travelling packets has been introduced. If the scale is sufficiently large, every photon emitted at frequency ν_0 could suffer in fact a non negligible red-shift $\Delta\nu$ (see discussion on Equation 1.3) due to the coupling with the Hubble flow as already explained in the Introduction. After travelling a distance d between two point in an expanding Universe of Hubble parameter H , the photon will reach redshift z with a frequency ν , and so, its

Doppler shift can be estimated as:

$$\Delta\nu \equiv \nu_0 - \nu = \frac{H(z)d}{c}\nu_0 > 0 \quad (3.11)$$

This effect could then be relevant for simulations with large comoving boxes and at low redshifts, when the IGM is more ionised and the photons have higher mean free path.

As already explained, CRASH follows the propagation of coloured packets, i.e. photons grouped in frequency bins according to their source spectrum (see [157]). On the other hand, the Formula 3.11 suggests that the Doppler shift accumulates differently for each group of photons in the packet, in fact $\Delta\nu \propto \nu_0$. At each cell crossing, CRASH accounts for this 'frequency-selective' shift accumulating a separate $\Delta\nu$ for each bin. When the cumulative $\Delta\nu$ becomes greater than the frequency bin size, the algorithm moves the affected photons to the previous bin, representing lower frequencies. This repeats until the energy of the travelling photons falls below $E_{\text{HI}} = 13.6 \text{ eV}$.

Despite the simplicity of this algorithm, a wrong implementation could destroy the code performances because it is applied at every cell crossing. In the new CRASH software framework (see next Section), the correct extension of the FORTRAN type PHOTON_PACKET, solved the problem with minor impact on the software performances.

A second relevant improvement I have implemented in CRASH is the possibility of associating to every source a different spectrum. Population evolution in redshift can also be simulated changing their spectra at each snapshot; this has been done to allow a modelling of an arbitrary number of source populations without increasing the computational time. The details of the implementation of this feature will be discussed in the next Section as example of modelling by FORTRAN types.

3.3.2 CRASH software architecture

In developing the new version of CRASH I have engineered the code to reproduce the algorithmic logic described in the previous Section by using the programming language FORTRAN 95. The source code is then implemented in the traditional imperative programming style, but it strictly follows the software engineering principle of engine abstraction and problem modelling by using FORTRAN types and procedures. Software abstraction ensures that once the main algorithm (in this case the one following the radiative transfer of photons) is established, its application to a specific problem as well as its execution, do not depend on the initial conditions of the problem at hand. Hereafter with every capitalized name I will indicate that the corresponding variable in the code is a FORTRAN TYPE.

Starting from the algorithm existing in the latest version of the code (CRASH2 in [157]), I have, first of all, abstracted the data and the physical properties associated to the problem at hand, from the general radiative transfer scheme. This is done by abstracting every code variable from its specific value which can be set up in external, editable ASCII configuration files.

In addition to data abstraction, I have implemented procedural abstraction by isolating the general CRASH work-flow from any specific routine implementation; the main algorithm

remains then valid for an arbitrary combination of physical effects (e.g. H and He physics, UV or x-ray photons, Ly α photons, metals etc..) which can be enabled or disabled depending on the specific requirements of the problem at hand. To achieve this goal, first I have defined two software layers: the `CRASH_SYSTEM` and the `CRASH_SIMULATION`. These layers correspond to FORTRAN types and their logical, independent work-flow is structured in three steps: initialization, execution, termination. Finally, I have introduced logical switchers, called `CONTROLLERS` (which can be externally configured) in order to change the logical work-flow. One example of `CONTROLLER` is the variable regulating the activation of the Doppler effect: if the simulation starts and it is configured with Doppler off, the photon packets are not shifted in their internal frequencies until the option is changed, even on-the-fly, i.e. during the run.

These changes assure a more flexible code because the main radiative transfer algorithm is extremely general and applicable to a number of different problems by just changing the configuration files, while in its previous version the code required major changes also to the main algorithm. I will now describe in more detail some aspects of the new implementation.

The `CRASH_SYSTEM` is the software layer which handles the program start-up, the initialization of precomputed tables and databases (which will be used throughout the simulations), as well as the `CRASH_SIMULATION` execution. It also includes additional services and functionalities complementary to any successful simulation set-up and run. For example, it provides many ICs creation utilities, a lot of output analysis and format conversion tools, as well as routines that simplify the execution within cluster queues. In the new `CRASH` I have also introduced arbitrary data formats to increase the program output compatibility and to facilitate their visualization. Typical examples of the data formats are HDF5, XML or VTK. To provide a set of `CRASH_SYSTEM` services which is flexible and at the same time which can be easily expanded in the future, at the program start-up (i.e. the `CRASH_SYSTEM` initialization) I have used the technique called software channelling. This means that there are a number of commands, sub-commands and options which move the execution flow away from the standard direction, i.e. the control of the execution flow is delegated to some parallel channels. The combination of the available system commands and sub-commands is available by using the specific command: `'-help'`.

Currently implemented functionalities are:

- ICs creation utilities: creation and modification of density maps, temperature maps and maps of photon sources.
- Output analysis, parsing and conversion tools: statistical analysis of `CRASH` output maps, sub-map comparison, conversion to various formats and data extraction functionalities.
- Database of random number generation algorithms.
- Output visualization tools: gas number density, temperature maps and source distribution maps, as well as the output files containing ionisation fractions and gas temperature can be converted in VTK format files. Visualization of large VTK data

format is fully supported on visualization clusters by the free software Kitware Paraview and Visit.

- System help, debug and trace.
- System paper reference and CRASH citation and credits rules.

The main advantage of this approach is that the CRASH_SYSTEM can be arbitrarily developed and extended without alterations of the radiative transfer algorithm. This also ensures the right software isolation level and guarantees safety in terms of software debugging and error de-correlation.

The basic functionalities of the CRASH_SYSTEM layer are configured loading two ASCII files. The first file (SYS_INIT.in) contains information for the system storage, the type of random number generator algorithm in use and its initialization parameters. The file SYS_ITR.in contains instead the snapshot iterator properties (i.e. the indexes of the current, last and first snapshot) when an evolution in the ICs needs to be taken into account, as for example in a simulation of cosmic Re-ionisation. The implementation of the snapshot iteration at the CRASH_SYSTEM level will also help in preparing for the future separation of a RT module (based only on the CRASH_SIMULATION) that will be coupled with cosmological hydro-codes.

Once the CRASH_SYSTEM initialization is finished, the code work-flow starts the SIMULATION thread.

CRASH_SIMULATION is the software layer which implements the RT work-flow described in 3.3.1. The CRASH_SIMULATION implements the RT scheme reproducing the cosmological radiative transfer scenario described in 3. As already mentioned, I made extensive use of complex FORTRAN types instead of single unrelated variables. Each type represents a logical group of variables reproducing a physical quantity, for example a type could be used to represent a photon packet as an ensemble of single variables describing its spatial coordinates, frequency, intensity etc. Types can, in turn, be grouped into highly structured variables. The nesting level of such objects reflects their logical role within the physical problem we want to address. Following the CRASH work-flow, I have defined the some high level FORTRAN types:

- **COSMOLOGICAL_BOX**: this type represents the physical cosmological box in which the photons propagate. It contains the variables responsible for the domain discretization in cells, the domain evolution with simulation time and expansion with redshift. Each cell is represented by a group of variables called COSMO_CELL. The COSMOLOGICAL_BOX naturally contains two complex types : COSMO_GAS and COSMO_RADIATION.
- **COSMO_GAS**: this type represents the gas inside the cosmological box. It contains all the global variables responsible for the gas properties as its number density, n_{gas} , temperature T and ionisation fractions. Other set of internal types are then used to describe the atomic properties of the gas components: hydrogen and helium. The variable GAS_HYDROGEN, for example, describes properties as the value of the resonance

frequency, of the cross section at the sampled frequencies, of the relative optical depth and recombination time scale, among others.

- **COSMO_RADIATION**: this type represents the radiation field. The point-like emitters are described as a **POINT_SOURCE** type, which collects the physical properties of a source specifying its luminosity, **SPECTRUM** type and position coordinates. The **COSMO_RADIATION** is discretized by using two types: **PHOTON_PACKET_REC** and **PHOTON_PACKET**. A **PHOTON_PACKET_REC** variable represents a group of monochromatic photons re-emitted by the gas following its recombination. It is characterized by the number of photons reemitted, its spatial coordinates and frequency. A **PHOTON_PACKET** instead represents a coloured packet (as described in the **CRASH** work-flow). The diffuse background field is also part of the generic type **COSMO_RADIATION**. It is simulated by a tridimensional set of variables types called **EMITTER_POINTS**, equally distributed over the **COSMOLOGICAL_BOX** grid nodes. Node emitters are simplified **POINT_SOURCE** types, sharing a common **SPECTRUM** type. More details on the background implementation can be found in Chapter 5.

By following the same software abstraction principle introduced in the **CRASH_SYSTEM** description, I have fully parametrized the **CRASH_SIMULATION** with a set of configuration files which are read and used to initialize the relative variables of the **SIMULATION**; this is done during the simulation initialization step. This is another example of code and algorithm isolation: a separated step involving just the **CRASH_SYSTEM** initialization variables has been implemented, in order to isolated every snapshot specific property as prescribed by the main algorithm in 3.3.1.

Once **CRASH_SYSTEM** and **CRASH_SIMULATION** have been specified as detailed above, the implementation of the RT algorithm is trivial. For each emission event by point sources, a variable called **CURRENT_PHOTON_PACKET** stores the properties of the emitted packet (spatial coordinates, frequency bins, Doppler shifts, number of photons per frequency bin, etc) and changes them as the packet propagates along its path. The update of the properties is done every time the packet crosses a cell by calling routines that simulate its interaction with the gas contained in that cell. In terms of the variables already introduced, the cell which is crossed becomes the variable **CURRENT_CELL** of the type called **COSMO_CELL**. Once the **CURRENT_PHOTON_PACKET** properties have been updated and if enough photons are still contained in the packet, this is moved to the next cell, otherwise it is considered fully absorbed and erased from the memory. The flow control then returns to the loop handling the emission from the point sources.

The global **CRASH_SIMULATION** work-flow is then realized nesting the previous packet-to-cell interaction into a loop over the point sources and/or the background node emitters. A further external loop over the emission events per source (N_p emitted packets per each source or node) controls the MC sampling of the **COSMOLOGICAL_BOX** and closes the thread flow.

The final program termination is a two step process: the first step is the **CRASH_SIMULATION** termination, which erases all variables from the RAM memory. Then the flow control returns to the **CRASH_SYSTEM** for the FORTRAN program end execution.

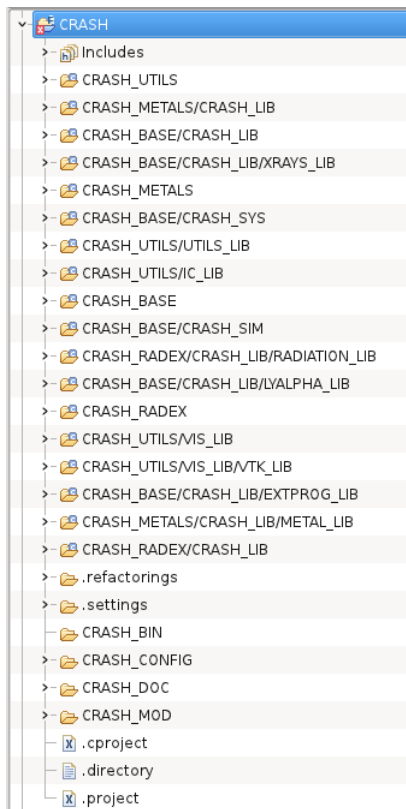


Figure 3.1: Code tree as shown in the Eclipse code Browser. The source folder CRASH_BASE contains the basic CRASH2 source code. The CRASH_METALS contains the metal ions plug-in and CRASH_RADEX the radiation tracking capability, these plug-ins are distributed with CRASH3. CRASH_UTILS contains plug-in with tools for ICs creations and output parsing and analysis capabilities.

The development strategy described before has the main advantage of minimizing the loop iterations, unveil the feedback relationships between variables, and intuitively mimic the real physics beyond the simulated processes.

3.3.3 CRASH modularization and optimization

The modularization of the MC scheme simplifies the software development and optimization. In terms of development, I have implemented the CRASH modularization strategy by using the variable modularization, and the functionality modularization, as technically explained in the previous Section. This high level of variable typisation (i.e. making extensive use of types) helps in avoiding code redundancies and in implementing a correct scoping strategy¹. In this way it is possible to avoid any redefinition, re-allocation and copy, just by correctly handling the visibility of the global variables naturally nesting them

¹The scoping strategy defines the visibility of a variable: it is referred to as global if a variable is visible to all the subroutines at all times and it is always kept in memory; it is instead local if a variable is

inside super-variables. This also helps in following more clearly the physics behind the simulated process and allows the software compiler to optimize the source code during the binary executable production.

One practical example is provided by the implementation of the multi-spectrum feature, which, as already mentioned, allows each source to have its own spectrum, so that the code can be applied to realistic configurations in which different source populations are present at the same time. Each `POINT_SOURCE` is in fact implemented as a separate type, and thus it is possible to increase the number of its properties just by adding more details to the type. For example, it would be trivial and at no computational cost to associate to each point source also an escape fraction. This process is known as extension of abstract types. In addition, delegating the source configuration to the initialization of `CRASH_SYSTEM` and `CRASH_SIMULATION` allows a pre-analysis and pre-loading of all the spectra in use, which are stored in a database. This, in turn, can help saving computer memory and allowing an arbitrary number of associations. A practical example of computational gain comes from simulations of IGM Re-ionisation, when the RT is run for several different snapshots and, each time, a new set of sources and spectra should be reloaded. In its present implementation though, `CRASH` keeps in memory all the sources and spectra loaded during the initialization, allowing a substantial increment in simulation speed and performances.

The functionality modularization consists in the possibility of plugging new functionalities into `CRASH` without changing the main algorithm of the code. In practice this means that new physical processes can be easily included as separate modules and defining new type variables. For example, in its latest formulation `CRASH` simulates the propagation of photons through a gas made of hydrogen and helium, but a new module (explained in details in Chapter 4) which includes heavy elements has been added. In the near future, the contribution of dust will be included in a similar way. Extensions of the frequency range to include x-rays and the coupling with $\text{Ly}\alpha$ photons have already been implemented (but still under testing), by extending the definition of the type `SPECTRUM` and the energy balance. These changes have been successfully implemented without changing anything in the main algorithm, without adding software loops and thus minimizing the impact on the simulation performances.

3.3.4 CRASH code and file structure

The source code of `CRASH` is managed and organized by using the free development environment Eclipse (<http://www.eclipse.org>). The source code organization strictly reflects the modularization described in the previous Sections. The separation between `CRASH_SYSTEM` and `CRASH_SIMULATION` is reflected by a code separation into the folders `CRASH_BASE/CRASH_SYS` and `CRASH_BASE/CRASH_SIM`. Common RT libraries implementing the `COSMO_GAS` type, `COSMO_RADIATION` type and internal variable types, are contained in the `CRASH_BASE/CRASH_LIB`. The basic version of `CRASH` is then stored into the `CRASH_BASE` directory. Other folders contain additional plug-in features imple-

allocated and de-allocated within a subroutine.

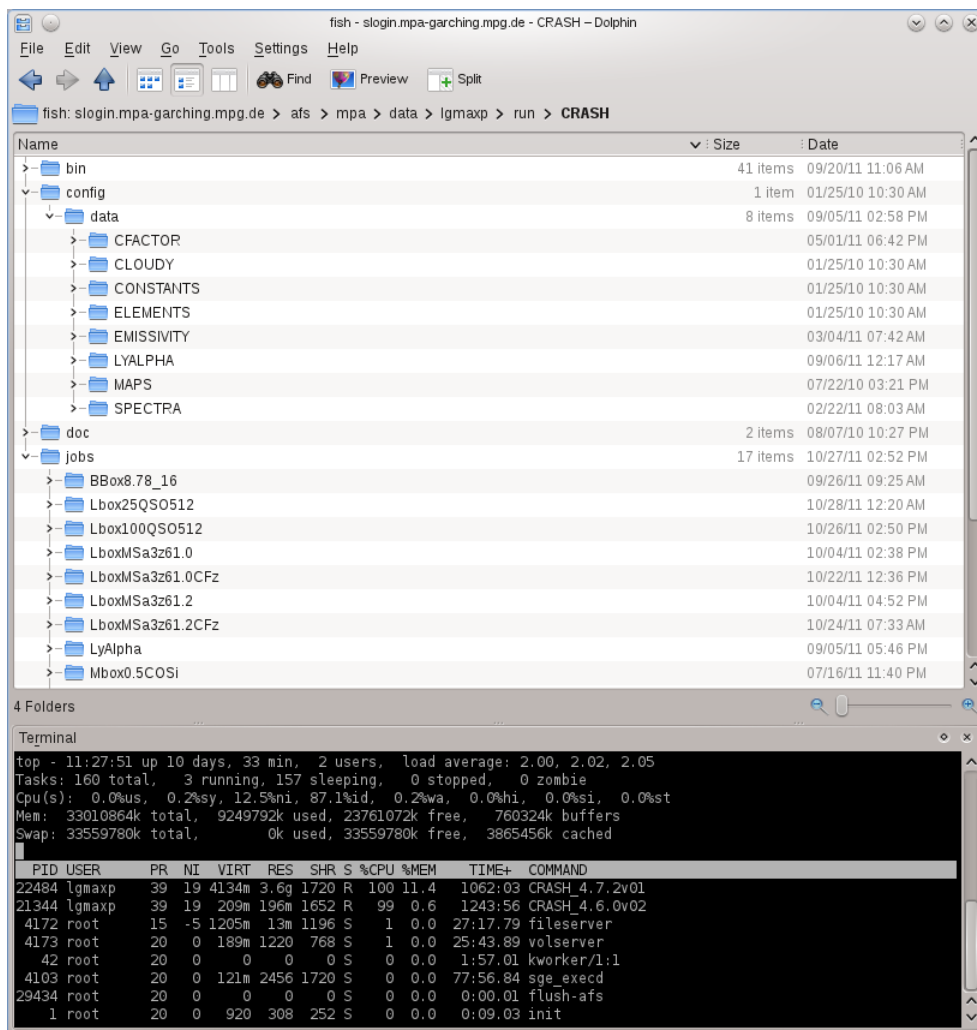


Figure 3.2: CRASH file tree and directory organization. In the bottom, a remote view of two running simulations of CRASH in the MPA cluster.

mented as FORTRAN modules. CRASH_UTILS stores, among others, FORTRAN utilities to generate ICs and parse output files. These utilities are plugged into the CRASH_SYSTEM and can be called by shell parameters as already explained. In the folder CRASH_METALS the plug-in extension for the heavy elements can be found. This plug-in is part of the CRASH3 distribution and will be extensively discussed in the next Chapter with the radiation tracking plug-in contained into the folder CRASH_RADEX. In Figure 3.2 we report a file system browser view of a typical CRASH installation. All the binaries and script files of the CRASH_SYSTEM are stored in the CRASH/bin directory, the data files loaded at the system initialization are contained into the CRASH/config directory and the program documentation and presentation files into the CRASH/doc directory. The job directory contains many sub-directories representing separate simulations. The file system structure of every simulation is rigidly established as shown in Figure 3.3. Every sim-

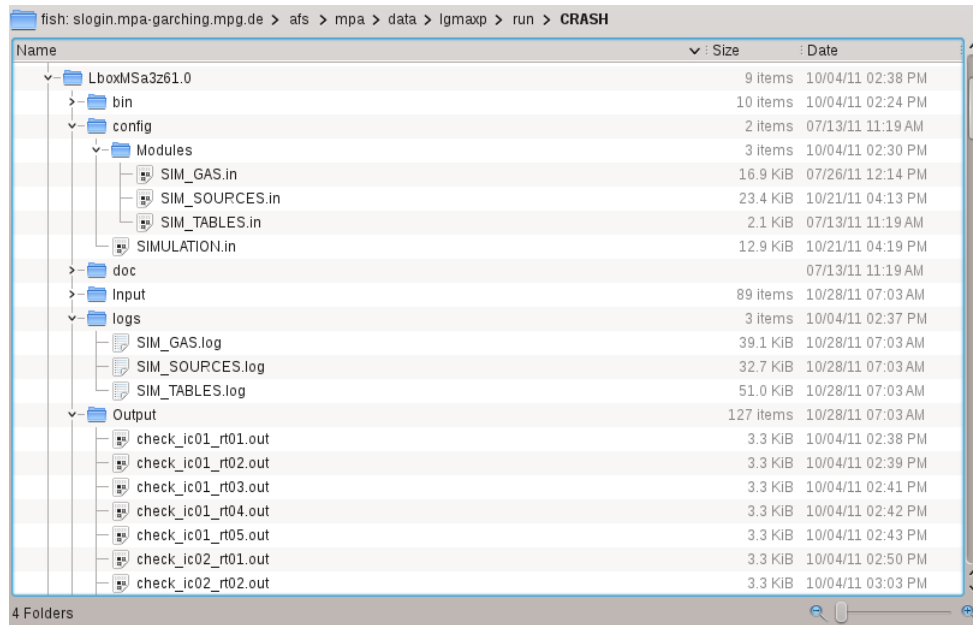


Figure 3.3: CRASH SIMULATION file tree and directory organization.

ulation can be considered as a separate subprogram with its own configuration in the CRASH/jobs/<SIM_FOLDER>/config directory. The simulation scripts responsible for the queue processing and submission are contained in the “bin” directory. Specific simulation backup or running notes can be stored into the “doc” directory. Every RT entity has its own log stored into the “log” directory. ICs are stored into the “Input” directory and the final outputs into the “Output” folder.

The rigid association between source code and file system structure allows the running of many simulations in a common framework of tabulated data avoiding configuration errors and inconsistencies. Every simulation is a self-consistent and independent task run by the abstract engine implemented in many binary files in the CRASH/bin directory. The choice of the engine version or the run can be made just changing a variable name in the simulation submission script. As shown in the cluster remote view reported in Figure 3.2 it is then possible to run different versions of the code at the same time, simplifying the program debugging and execution in an unified software scheme.

Chapter 4

CRASH3: Cosmological radiative transfer through metals

In this Chapter I will introduce the third release of `CRASH`, which is able to perform RT simulations including the most common metals observed in the IGM (2.6) and to derive their ionisation states self-consistently with the field created by the radiative transfer.

`CRASH3` [104] introduces C, O and Si in the standard `CRASH2` [157] photo-ionisation algorithm by using a pipeline which combines the excellent capabilities of `CRASH` in tracing the radiation field with the sophisticated features of the photo-ionisation software `Cloudy` [83]. The inclusion of a sensitively large set of data imposed by the numerous metal ionisation states has required a further source code re-engineering and a re-modelling of the photon packet-to-cell interaction to implement the radiation tracking (see 4.3.1). The third code release, fully re-factored and customised to solve these issues, is consequently more optimized, and it further improves on the modularisation described in Chapter 3.

I will introduce the general problem of including metal ions in a radiative transfer algorithm in Section 4.1. The photo-ionisation code `Cloudy` is then briefly introduced in Section 4.2 and the details of the new implementation of `CRASH3` pipeline in Section 4.3. Finally, some of the many tests I have performed to establish the new code release reliability are reported in Section 4.4.

4.1 Radiative transfer through metals

The extension of the `CRASH` algorithm (see 3.3) with the full micro-physics of metals is hardly viable because of the extreme complexity of the metal electronic structure which would increase the computational costs of a RT simulation to unacceptable high levels (see [70, 71] and references therein for a complete treatment of the physics of the metals in astrophysical ionised regions). For this reason, I have adopted a hybrid approach in which `CRASH` performs the RT only through H and He, while the metal ionisation states are implemented self-consistently, but they are calculated with the photo-ionisation code `Cloudy` ([83, 191, 82], but see also 4.2 for a brief introduction).

The two algorithms interact in a single pipeline called **CRASH3** which coordinates their inputs and outputs as detailed in 4.3.

CRASH3 recognises the metal enriched sub-domain by applying a masking technique to it and by labelling the enriched cells with subscript k . After masking the k -cells containing metals (see Section 4.3.1 for more details), **CRASH** derives the spectral energy distribution and luminosity of the ionising radiation background (S_k, L_k) created in each of the k -cells; **Cloudy** then uses these values to determine the corresponding ionisation states of the metals and the temperature of the enriched gas.

To ensure that the ionisation configuration of the metals is consistent with this energy set-up, I have implemented an internal convergence test in which the pipeline automatically checks that the ionisation fractions of H and He evaluated by **Cloudy** and **CRASH** are in agreement at each step. An example of the internal convergence that can be reached by accurately tuning the pipeline is discussed in Section 4.4.1.2.

Despite the conceptual simplicity of this approach, the coupling of **CRASH** and **Cloudy** in a single numerical scheme is neither straightforward nor trivial. In the following I will describe the strategy adopted for such integration, also discussing its validity.

First, it is necessary to point out that this approach neglects the contribution of metals to the optical depth for energies $E > 13.6\text{eV}$, as well as to the diffuse radiation emitted by recombining gas. This approximation is justified as long as the metal abundances are very small compared to those of H and He. In fact, if the total number density of heavy elements (n_Z) is $n_Z > 10^{-3}n_H$, the total photo-ionisation cross section is dominated by the metal component (see [71] - Chapter thirteen for a complete discussion). Because the metallicity observed in the IGM is below this value (see 2.2), the above assumption is justified in the cases of our interest.

On the other hand, metals could impact the thermal state of the gas with a non negligible contribution to the gas cooling function Λ (see Equation 3.1). This feedback on the gas temperature is therefore taken into account as discussed in Sections 4.3.3 and 4.4.

It should be clarified that in order to couple the **Cloudy** 1D approach with the fully 3D radiative transfer implemented in **CRASH**, a series of assumptions are needed. These are discussed below.

Once the pipeline knows the (S_k, L_k) values in the metal enriched cells, it re-simulates the ionisation and thermal state of a set of k -equivalent metal enriched systems with **Cloudy**. This choice means that the spatial scale at which both engines are asked to converge matches the spatial resolution of **CRASH**, i.e. the cell size Δx .

Coupling the code 'cell by cell' has several advantages, among which in each cell of **CRASH** all the physical quantities are spatially uniform and thus the equivalent set-up of **Cloudy** can set every physical quantity as constant.

Once the coupling strategy is established, the ionisation structure in the enriched cells can be evaluated as a sequence of equilibrium configurations at times t_m . To reduce the computational cost of the global pipeline, I have made extensive use of a large database of precomputed results from **Cloudy**.

The values of (S_k, L_k) are determined in each k -cell adding up the contribution of all the incoming photon packets in the time interval $t_{m+1} - t_m$. In practice, the code tracks

all the multi-frequency packets entering the cell from arbitrary directions, each packet being distorted by the continuous absorptions during its path; the average SED in the k -cells $S_k(t_{m+1})$ is then calculated from the contribution of all the photon packets in each frequency bin.

As detailed in Section 4.2, `Cloudy` can deal with either a single source configuration or a background radiation. If only a single source is present in the computational domain of `CRASH` or when each cell is illuminated from a preferential direction, then the `Cloudy` point source configuration should be used (this is tested in Sec. 5.1) to estimate the ionisation and temperature configuration of the cell. When instead a cell is illuminated more or less uniformly from all directions, then the background radiation set-up should be adopted in the `Cloudy` configuration.

In the current implementation of the `CRASH3` pipeline I have included the species C, O and Si, which are the most abundant metals observed in the IGM, typically in the form of ions like $O\text{ II}$, $O\text{ VI}$, $Si\text{ IV}$, $C\text{ IV}$ as specified in 2.2. However, the inclusion of other species, which may be relevant for a more accurate estimate of the gas cooling function, is a straightforward extension of the present scheme and will be illustrated in Section 4.4.

In the following, I give more technical details on the `CRASH3` implementation.

4.2 The photo-ionisation code Cloudy

`Cloudy` [83] is a code designed to simulate the physics of the photo-ionised regions produced by a wide class of sources ranging from the high temperature blue stars to the strong X-ray emitting Active Galactic Nuclei. The main goal of `Cloudy` is the prediction of the physical state of photo-ionised clouds including all the observably accessible spectral lines. The latest stable release of `Cloudy` (at the time of writing v 8.01¹) simulates a gas which includes all the heavy elements of the typical solar composition and the contribution of dust grains and molecules present in the ISM.

In this Section I will focus on the description of the `Cloudy` features that have been primarily used to implement `CRASH3`. The reader interested in the details of the code implementation or in reviewing the many physical processes included in the code can find more appropriate references in [83] and [82].

Unlike `CRASH`, `Cloudy` is a 1D code assuming as preferred geometrical configuration a symmetrical gas distribution around a single emitting source, with photons propagating along the radial direction. `Cloudy` can also simulate the diffuse continuum reemitted by recombining gas as nearly isotropic component under the assumption that the diffuse field contribution is generally small and can be treated by lower order approximations. Additional isotropic background fields can also be handled, as long as their shape and intensity are specified by the user. Some popular background models (like the Haardt and Madau cosmic UV spectrum [149]) are already distributed with the code. The contribution of the CMB can also be accounted for in the computation because it is an important source of Compton cooling for low density gas configurations typical of the IGM (see 2.1).

¹<http://www.nublado.org>

The micro-physics implemented in `Cloudy` is very accurate: it includes all the metals present in the typical solar composition [105] described as multilevel systems and treated self-consistently with the ions of the lightest 30 elements. Photo-ionisation from valence, inner shells and many excited states, as well as collisional ionisation by both thermal and supra-thermal electrons and charge transfer, are included as ionisation mechanisms. The gas recombination physics is simulated including the charge exchange, radiative recombination, and dielectronic recombination processes. `Cloudy` simulates all these processes adopting an approximation method for the radiation field evaluation known as escape probabilities method [122], instead of evaluating the full radiative transfer as done by `CRASH`. This choice implies the loss of many details pertaining the line properties description, e.g. line pumping by the incident continuum, photon destruction by collisional deactivation and line overlap. In the standard release of `CRASH` the details of the lines are not accounted for and the above limitations are thus negligible.

Once the characteristics of the source and the species involved in the calculation are set up, `Cloudy` estimates the radial distribution of the ionisation and temperature fields by simultaneously solving the equations of ionisation and thermal equilibrium ([70, 187, 71]). A static solution describing the physical state of the gas is then found by dividing the domain in smaller regions and iterating until convergence is reached. The usual assumption of such calculations is that atomic processes occur on timescales much faster than the temporal scales of the macro-physical system. `Cloudy` does not 'a priori' assume that the gas is in equilibrium and the solution provided is a general non-equilibrium ionisation configuration for a static medium that does not retain any information of the temporal evolution of the system towards the converging state. A large set of information about the relevance of the physical processes that establish the final convergence, and the details of the line emission processes are also provided with a great level of detail; this micro-physic treatment can not be directly handled in `CRASH` with the same level of accuracy.

`Cloudy` describes the thermal equilibrium of the photo-ionised gas providing the local thermal balance obtained in each simulated sub-region. In the absence of non-thermal electrons produced by high-energy photons, this thermodynamic equilibrium is generally specified by the electron temperature T_e because the electron velocity distribution of the gas is predominantly Maxwellian. The `Cloudy` output contains many different averaged values of T_e useful for line diagnostics (see the `Cloudy` Hazy 3 manual); in the `CRASH3` pipeline, where the code coupling is implemented on the scale of the cells simulated by `CRASH`, the values of the gas temperature will refer to a volume average of T_e .

Although I tried to minimise the differences between both codes, the deeply different set-up of the simulations in `CRASH` and `Cloudy`, both in the source spatial distribution and in the gas micro-physics, has presented some challenges, which will be detailed in the following Sections.

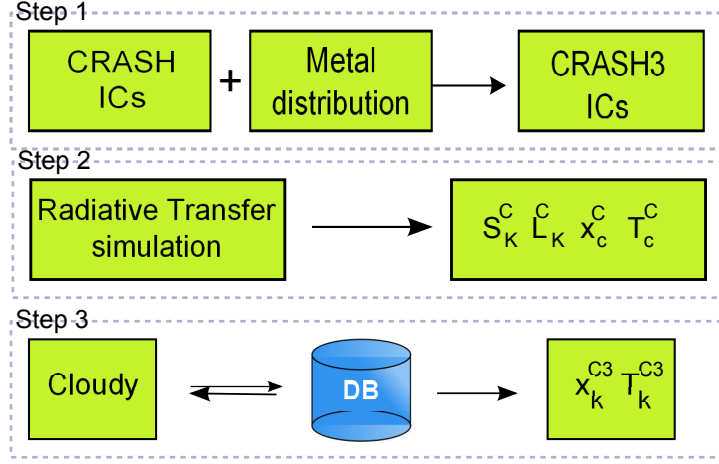


Figure 4.1: CRASH3 simulation pipeline for a single snapshot. The quantities S_k^C and L_k^C define the SED and luminosity tracked in the k metal enriched cells. x_c^C refers to the H and He ionisation fractions in each cell c of the domain and T_c^C is the corresponding gas temperature. x_k^{C3} are the final ionisation fractions for all the species in the tracked cells and T_k^{C3} the temperatures in the enriched cells as provided by the database (DB). See text for more details.

4.3 Pipeline implementation

In this Section I give a description of the CRASH3 pipeline used to derive the metal ionisation fractions. This is sketched also in Figure 4.1. It should be noted that if the radiative transfer is performed in a cosmological context, the pipeline applies to each single redshift, z . In this case, in addition to the ICs of the RT simulations, other physical quantities might depend on z , e.g. the cooling off the CMB radiation.

The starting point of the pipeline (Step 1 in Figure 4.1) is the set-up of the CRASH3 ICs, which are the same of CRASH as specified in Section 2, with the addition of the number density of heavy elements in the k metal enriched cells, i.e. $(n_{C,k}, n_{O,k}, n_{Si,k})$.

The next step (Step 2 in Figure 4.1 with variables marked by the superscript C) consists in performing a RT simulation which, in addition to the evaluation of $x_{\text{HII},c}^C$, $x_{\text{HeII},c}^C$, $x_{\text{HeIII},c}^C$ and T_c^C in all the cells of the domain, tracks also the SED and luminosity of the ionising radiation in each of the k ($< N_c^3$) metal enriched cells (S_k^C, L_k^C) . All the above physical quantities are stored at times t_m .

Finally, a search engine looks for the Cloudy precomputed configuration that best matches the values $(x_{\text{HII}}, x_{\text{HeII}}, x_{\text{HeIII}}, S, L)_k^C(t_m)$ and provides the ionisation fractions of the metal ions and the electron temperatures T_k^{C3} of the gas in the metal enriched sub-domain (Step 3 in Figure 4.1 with values marked by superscript $C3$). If the matching criteria are not satisfied (see below for more details), the database is extended with additional on-the-fly Cloudy runs, using (S_k^C, L_k^C) as energy input. It is important to point out that Step 3 is confined to the k enriched cells. In fact, it does not severely affect the basic algorithm performances for two reasons: (i) a large number of Cloudy calculations are precomputed

E_{ion} [eV]	H	He	C	O	Si
E_{xI}	13.598	24.587	11.260	13.618	8.152
E_{xII}		54.400	24.383	35.118	16.346
E_{xIII}			47.888	54.936	33.493
E_{xIV}			64.494	77.414	45.142
E_{xV}			392.090	113.900	166.770
E_{xVI}			489.997	138.121	205.060

Table 4.1: Ionisation potentials for H, He, C, O and Si until the ionisation level VI as used in Cloudy.

and stored in a database which can be accessed in a reasonable computing time, and (ii) metal pollution in the IGM is statistically confined around the sources, so that a limited number of cells ($k \ll N_c^3$) is involved in the calculation.

In the following I will discuss in more detail some aspects of the pipeline.

4.3.1 Initial conditions for CRASH3

As already mentioned, in addition to the initial conditions of CRASH, CRASH3 requires the spatial distribution and abundance of all the metal species present in the computational domain. These can be artificially created by hand (as done in Section 5.3) or can be obtained as a result of e.g. hydrodynamic simulations that include physical prescriptions for metal production and spreading (see 2.2.2).

A preliminary analysis of the spatial distribution of metals allows to identify the k -cells that need the radiation field tracking (Step 2) and the final evaluation by Cloudy (Step 3). To keep track of these cells a boolean mask is built isolating the enriched portion of the simulation volume from the non-enriched one. The building of the mask can be performed before the beginning of the simulation and passed as additional IC or can be created in memory during the simulation initialization. If the mask contains k -true values, a shadow map of k cell spectra S_k^C is allocated to store the shapes of the incoming packets: each time a packet enters a cell, the mask is used to check whether the cell is an enriched one and consequently the packet spectral shape should update S_k^C . This assures that the radiation field in the relevant cells is properly sampled and its temporal variations accounted for.

4.3.2 The Cloudy database

In this Section I provide some details on the pre-computation of the database. The number of Cloudy computations required to describe a single snapshot including metals is estimated as:

$$N_S = k \times (m_f + 1), \quad (4.1)$$

where m_f is the number of times the evaluation of the metal ionisation state is performed. As a reference, $N_c = 128$, $m_f = 5$, and 1 percent of enriched cells would require $N_S = 10^5$

Cloudy computations which cannot be performed on the fly. I have then implemented a Standard Query Language (SQL) database (DB) using one of the codes freely available to the scientific community ².

Because I want the physical processes treated by Cloudy and CRASH to be as similar as possible (with the exclusion of the treatment of C, O and Si), I have stored configurations that explicitly disable in Cloudy the CO and H₂ molecules, as well as the dust grain physics and all the other metals. The charge transfer effects and the radiation pressure are disabled as well.

A more critical point is the use of the spectrum derived from the RT in a Cloudy simulation because the two engines span different frequency ranges. While CRASH simulates the propagation of hydrogen ionising photons, Cloudy requires that any spectral information is provided in the energy range $13.6136 \cdot 10^{-8} \text{eV} < E < 100 \text{MeV}$. For this reason, the spectrum used as input for Cloudy is the same as the one used in CRASH in the frequency range $13.6 \text{eV} \leq E \leq E_{max}$, while it is set to zero for $13.6136 \cdot 10^{-8} \text{eV} < E < 13.6 \text{eV}$ and $E_{max} < E < 100 \text{MeV}$.

As already mentioned, if the radiative transfer is run in a cosmological context the contribution of the CMB is included.

4.3.3 The feedback of metals on the gas temperature

CRASH3 evaluates the temperature evolution of the simulated gas in two steps. First, the gas temperature T_c^C is calculated by a CRASH simulation in each cell of the computational volume as in Step 2 of the pipeline. Then, T_c^C is corrected for the effects of metals in the enriched cells k by using the temperature T_k^{C3} , evaluated at Step 3.

On the other hand, a correct computation of the temperature is not trivial, because also in the absence of metals the temperatures predicted by CRASH (Step 2) and CRASH3 (Step 3) are not in perfect agreement in the vicinity of the point sources (see tests in [159, 157]). More generally, it has been shown that different approaches to the radiative transfer do not always predict consistent temperatures in such regions [124]. Every time a large discrepancy between temperatures in the two steps occurs it is important to understand if this is due to the metal cooling or just to the differences in the two codes. I then define the temperature deviation δT_k^i as:

$$\delta T_k^i = T_k^C - T_k^{C3}, \quad (4.2)$$

where $i = met$ refers to the deviation calculated for a gas contaminated by metals, while $i = pris$ refers to a pristine gas. The difference $\delta T_k = \delta T_k^{met} - \delta T_k^{pris} \geq 0$ by design and it is due only to the metal cooling. In the enriched cells in which δT_k is greater than some threshold value for the minimum tolerated deviation, T_k^C is replaced by T_k^{C3} . Note that the temperature correction has some weak feedback also on physical state of the gas via its recombination coefficients, especially for the helium component.

²e.g. Apache Derby: <http://projects.apache.org/projects/derby.html>

4.4 Tests

In this Section I present three tests designed to establish the reliability of the new code. The first test (Sec. 4.4.1) focuses on the standard Strömngren sphere case, albeit of a metal enriched gas. The second test (Sec.4.4.2) investigates the sensitivity of **CRASH3** by studying the fluctuations of the radiation field induced by different source types and tracked by the different metal ionisation states. Finally the third test (Sec. 4.4.3) describes a more realistic physical configuration by using as ICs those from a snapshot of a hydrodynamic simulation.

Hereafter the gas metallicity (or equivalently the metal mass fraction) is defined as $Z_g = M_Z/M_g$, where M_Z is the total mass of the elements with atomic number higher than 2 and M_g is the total mass of the gas; the metal mass fraction in the Sun is set to $Z_\odot \approx 0.0126$ (accordingly to the metal abundances relative to hydrogen as reported in the **Cloudy** Hazy guide I and references therein) taking in consideration the 10 most abundant elements: H, He, C, N, O, Ne, Si, Mg, S and Fe.

4.4.1 Test 1: Strömngren sphere with metals

I consider a configuration similar to the one in TEST 2 of the Cosmological Radiative Transfer Comparison Project [124], but for the presence of metals.

The simulation box has a comoving side length of 6.6 kpc and it is mapped on a regular grid of $N_c^3 = 128^3$ cells. The gas is assumed to be uniform and neutral at the initial temperature $T = 100$ K, with a number density $n_{gas} = 0.1 \text{ cm}^{-3}$ and a hydrogen (helium) number fraction of 0.9 (0.1). Only one point source is considered with coordinates (1,1,1), a black body spectrum at temperature $T = 10^5$ K and ionisation rate of $\dot{N} = 10^{51} \text{ phot s}^{-1}$ (i.e. a luminosity $L \simeq 5 \cdot 10^{40} \text{ erg s}^{-1}$). To ensure a good convergence of the MC scheme, the source radiation field has been sampled by $2 \cdot 10^8$ photon packets. The redshift of the simulation is set at $z = 0$ and the simulation duration to $t_f = 5 \cdot 10^8 \text{ yrs}$.

I also contaminate the gas with $n_C \simeq 2.2 \cdot 10^{-7}$, $n_O \simeq 4.41 \cdot 10^{-7}$ and $n_{Si} \simeq 3.12 \cdot 10^{-8}$, corresponding to $Z_g = 6 \cdot 10^{-3} Z_\odot$.

Although I contaminate the entire box with metals, it is possible to significantly reduce the number of the required **Cloudy** runs taking advantage of the spherical geometry of the HII region and assuming that each radial direction is equivalent. This is justified as long as the number of photon packets used is large enough that the fluctuations induced by the Monte Carlo sampling are negligible.

I then apply a spherical average of the radiation field at each distance d (expressed in cell unit) from the ionising source; the resulting \bar{S}_d spectra are then used as input for the N_S **Cloudy** calculations, as given in Equation 4.1³. Finally, the source spectrum is sampled by 91 frequencies and it extends to an ionisation potential of $E_{max} = 0.2$ keV in order to include the photo-ionisation edge of the ion O VI. Because I want to test the correctness of **CRASH3** in the simplest set-up, the temperature correction algorithm (see 4.3.3) is not applied in this test.

³Notice also that in this uniform case k reduces to d because of the spherical symmetry.

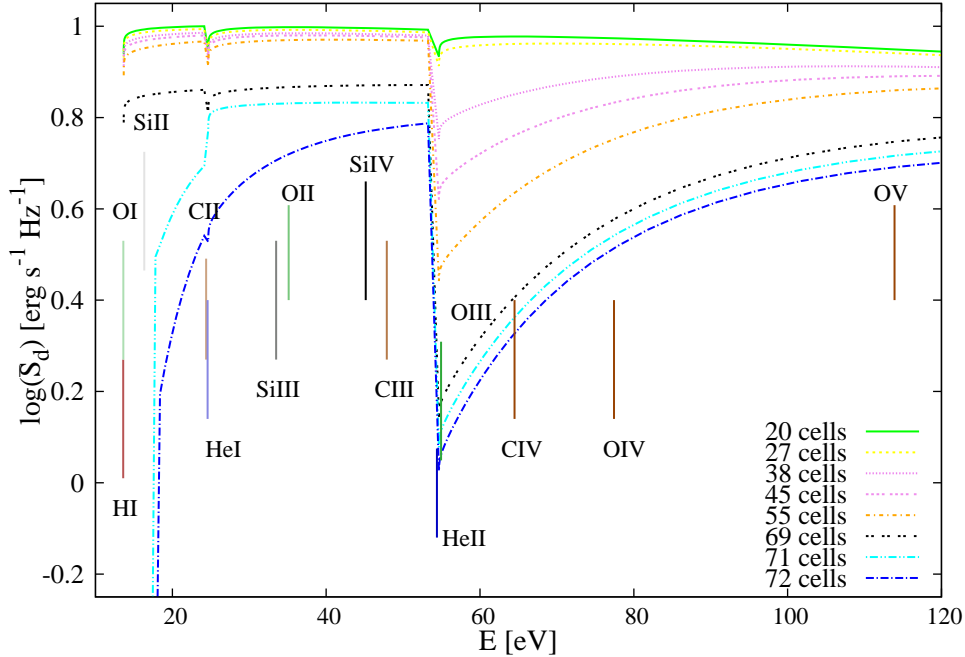


Figure 4.2: Normalized logarithm of the spherically averaged spectra $\log(\bar{S}_d)$. Lines refer to the spectra at different distances d varying from 20 (green solid) to 72 (blue dashed-dotted) cells. The spectra correspond to a time $t = 10^7$ yrs. As a reference, some ionisation potentials are also indicated as vertical lines.

4.4.1.1 Ionisation field

In Figure 4.2 I show how the spectral shape of the ionising radiation field described in terms of \bar{S}_d changes with the distance d as a result of geometrical dilution and filtering. Each line refers to the simulation time $t = 10^7$ yrs.

The spectra shown are truncated at $E = 120$ eV to have a better visualisation of the most relevant line potentials. The upper curve corresponds to a distance $d = 20$ cells (green solid), while the lower to $d = 72$ cells (blue dashed-dotted); at larger distances the luminosity $L_{ion}(d)$ becomes too faint to solve the ionisation equilibrium at Step 3 of the CRASH3 pipeline. The spectra are normalized to the maximum value of the spectrum at $d = 20$ cells for a better visualisation. The ionisation potentials of the metals enriching the box are also shown as reference even if, by design, metals do not contribute to the filtering of the ionising radiation.

The absorption due to H I, He I and He II is clearly visible in correspondence of the respective ionisation potential, i.e. 13.6 eV, 24.6 eV and 54.4 eV. The spectra at a distance $d > 69$ cells (black dashed-spaced) show an almost complete absorption at $E < 18$ eV due to the high column density of H I encountered.

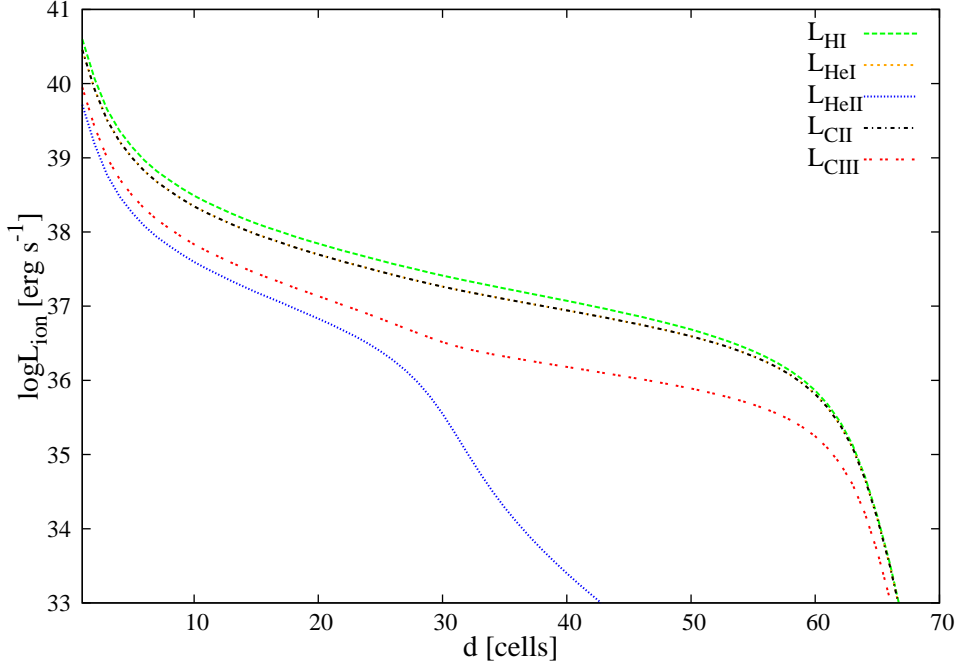


Figure 4.3: Logarithm of the photo-ionising luminosity L_{ion} [erg s^{-1}] as function of d . Different curves are calculated integrating all the photons above the ionisation threshold of: H I (green dashed line), He I (orange short-dashed), He II (blue dotted), C II (black short-dashed-dotted), C III (red dashed-spaced).

Figure 4.3 shows the total photo-ionising luminosity, L_{ion} [erg s^{-1}] available for the H, He and C ions as a function of d at a time $t = 10^7$ yrs. L_{ion} is defined as:

$$L_{ion}(d) = h^{-1} \int_{E_{ion}}^{E_{max}} \bar{S}_d dE, \quad (4.3)$$

where E_{ion} [eV] is the ionisation potential of the species considered (see Table 4.1 for reference) and h is the Planck constant.

Because CRASH3 only considers the photons with $E > 13.6$ eV, L_{ion} is an underestimate for those elements with an ionisation potential below 13.6 eV, i.e. carbon and silicon (also see 4.3.1). Note that L_{CII} (black short-dashed-dotted) overlaps with L_{HeI} (orange short-dashed) because of the very similar ionisation potential. If I increased the frequency resolution of the spectrum the curves would show some small difference. This would be at the expenses of the computational time without significant advantages in the accuracy of the metal ionisation state. For this reason I do not further increase the frequency resolution.

The luminosity of some species is not shown because the values are below the ones plotted in the Figure.

Notice that all the luminosities decrease smoothly with d ; this is consistent with the behaviour expected in an HII region, as already reported and extensively commented in [159] and [157] for the hydrogen and helium components.

4.4.1.2 CRASH3 pipeline convergence

Before proceeding further with the analysis of the results, I discuss the internal convergence described in Step 3 of the pipeline, by comparing the results of Step 2 (CRASH algorithm) and Step 3 (CRASH3 algorithm).

In Figure 4.4 I show the profile of x_{HI} , x_{HII} (top panel), x_{HeI} , x_{HeII} and x_{HeIII} (middle panel) as evaluated by Step 2 (dashed lines and variables with superscript C) and Step 3 (solid lines and variables with superscript C^3) in the gas configuration without the metal component and at a simulation time $t_f = 5 \cdot 10^8 \text{yrs}$, when the HII region has reached its equilibrium configuration. The values of x_{HI} and x_{HII} are shown in the top panel and result in agreement within 10^{-4} up to the ionisation front (I-front), identified with the location where the ionised fraction drops below 0.8. Across the front the agreement degrades from few percents to ~ 15 percent in the two cells in which the curves of x_{HI} and x_{HII} cross. In the tail of the I-front the agreement restores up to 10^{-3} . Both codes predict the front crossing in the same cell. A similar behaviour is shown in the middle panel for the ionisation fractions of helium. The ionisation fronts of He II (gray lines) and He III (violet lines) show a discrepancy of ~ 7 percent only in the cell in which the profiles cross, while in the remaining cells the discrepancy is limited to some percent. Reasonable accuracy (less than 20 percent) is also reached in the fronts of He II (gray lines) and He I (red lines) where both algorithms predict a similar shape. This front results difficult to reproduce because at the end of the HII region the illumination of the cells is very faint and sometimes the algorithm at Step 3 cannot converge.

The bottom panel shows the difference Δx between the two estimates of x_{HII} (blue solid line), x_{HeII} (gray solid line) and x_{HeIII} (violet solid line) in the previous panels, as function of the distance d . The increase in the difference between algorithms is evident in the points where the ions recombine.

Despite the satisfying internal agreement in the CRASH3 implementation, some small discrepancies remain, due to the differences between the CRASH and Cloudy geometries and the implementation of the ionisation and energy equations (see Section 4.2). By numerical experiments, I found that a critical ingredient to reach an acceptable convergence is to sample the source spectrum with a large number of frequency bins. This is necessary because the helium component is very sensitive to this sampling, in particular in the vicinity of the ionisation potential of He II.

The temperature radial profiles estimated by the two Steps are also shown in Figure 4.5 (top panel). The value of T^{C^3} corresponds to the electron temperature evaluated at Step 3. The plot shows large discrepancy between the temperatures in the cells near the source. In the bottom panel $\Delta T/T^{C^3}$ shows relative deviations from 60 percent (close to the source)

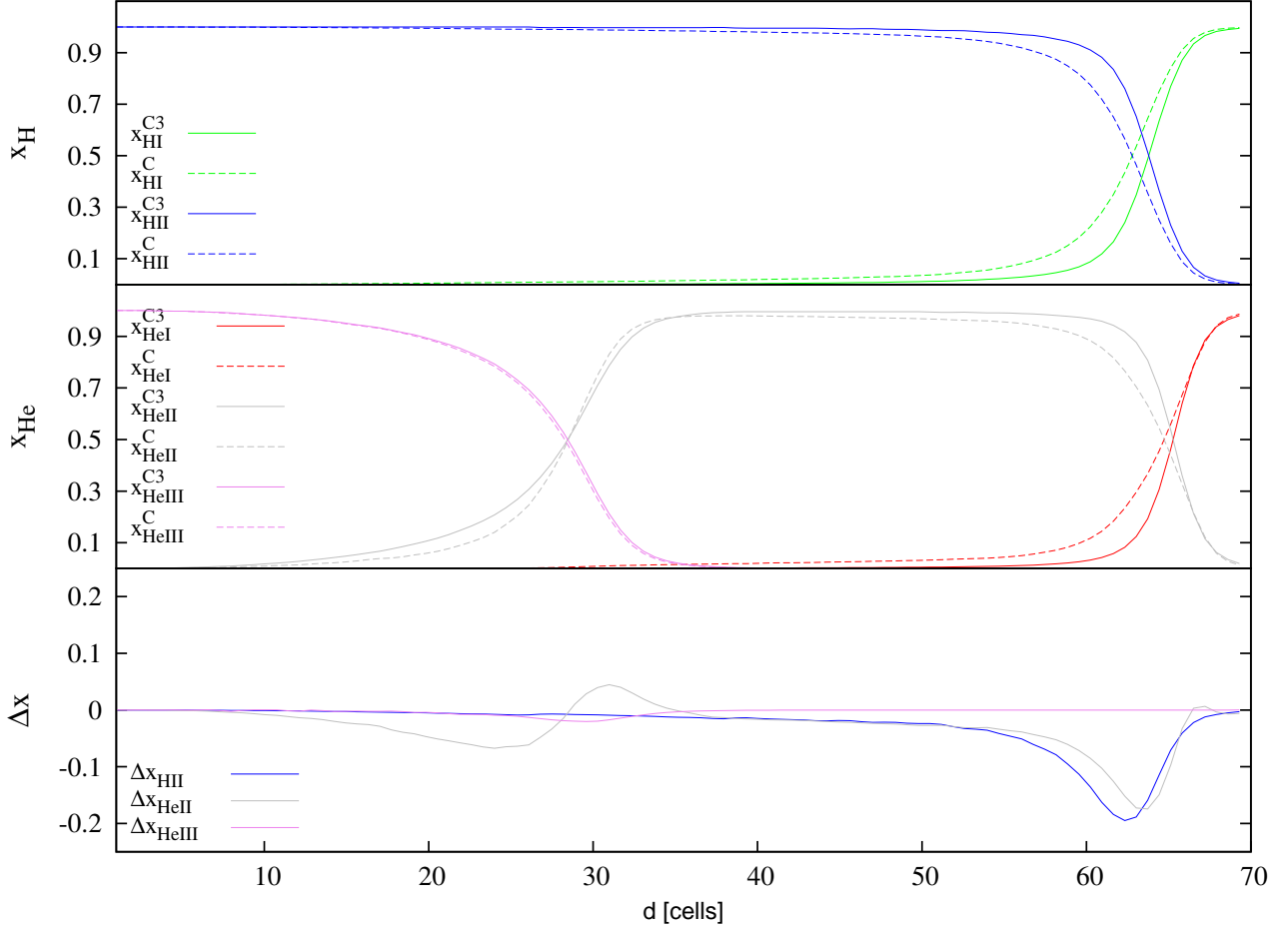


Figure 4.4: Internal convergence test between Step 2 (CRASH2) (dashed lines and variables with superscript C) and Step 3 (CRASH3) (solid lines and variables with superscript C^3) for the simulation time $t_f = 5 \cdot 10^8$ yrs. At distances larger than 70 cells the gas is neutral and therefore it is not shown in the plots. **Top panel:** profile of x_{HI} (green lines) and x_{HII} (blue lines) for Test 1 run in absence of metals. **Middle panel:** same as above for x_{HeI} (red lines), x_{HeII} (gray lines) and x_{HeIII} (violet lines). **Bottom panel:** difference Δx between the two estimates of x_{HII} (blue solid line), x_{HeII} (gray solid line) and x_{HeIII} (violet solid line).

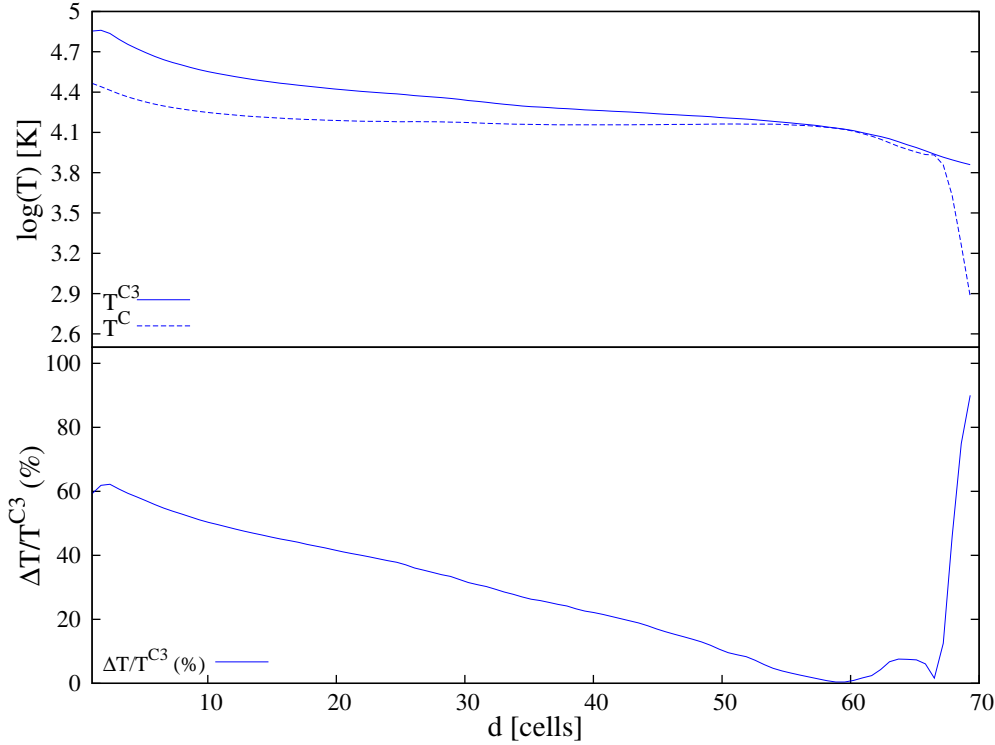


Figure 4.5: Temperature convergence between Step 2 and Step 3, as function of the distance from the source d , expressed in cell units. **Top panel:** temperature of Step 3 (T^{C3}) (solid line) and Step 2 (T^C) (dashed line) for the reference run at simulation time $t = 5 \cdot 10^8$ yrs, without metals. **Bottom panel:** relative difference $\Delta T/T^{C3}$ (solid line) in percent from the Step 3 (CRASH3) and Step 2 (CRASH2) temperatures.

down to 30 percent in $d \sim 30$ cells. The difference drops below 30 percent at $d > 30$ cells. This is not reflected in the H,He ionisation fraction agreement discussed above (see Figure 4.4) because of the weak temperature dependence in the gas recombination coefficients. Such a difference has been already noticed and discussed in the CRASH2 vs Cloudy comparison test in [157] and can be ascribed just to the different implementations of the temperature estimate in the two codes.

Because CRASH updates the temperature (compared to its initial value) only in those cells reached by ionising photons, outside the HII region T drops to the initial value of 100 K. On the other hand, the temperature calculated by Step 3 is provided by Cloudy and all the external regions where the illumination is too faint do not allow any convergent solution.

These convergence tests have been repeated using different ICs to test the dependence on the gas number density or on the source luminosity. More specifically, I have run simulations on a grid of cases with values $n_{gas} = 1, 0.1, 0.01 \text{ cm}^{-3}$ and $\dot{N} = 5 \cdot 10^{50}, 5 \cdot 10^{51} \text{ phot s}^{-1}$. It is found that, as the gas density decreases, the agreement improves for the

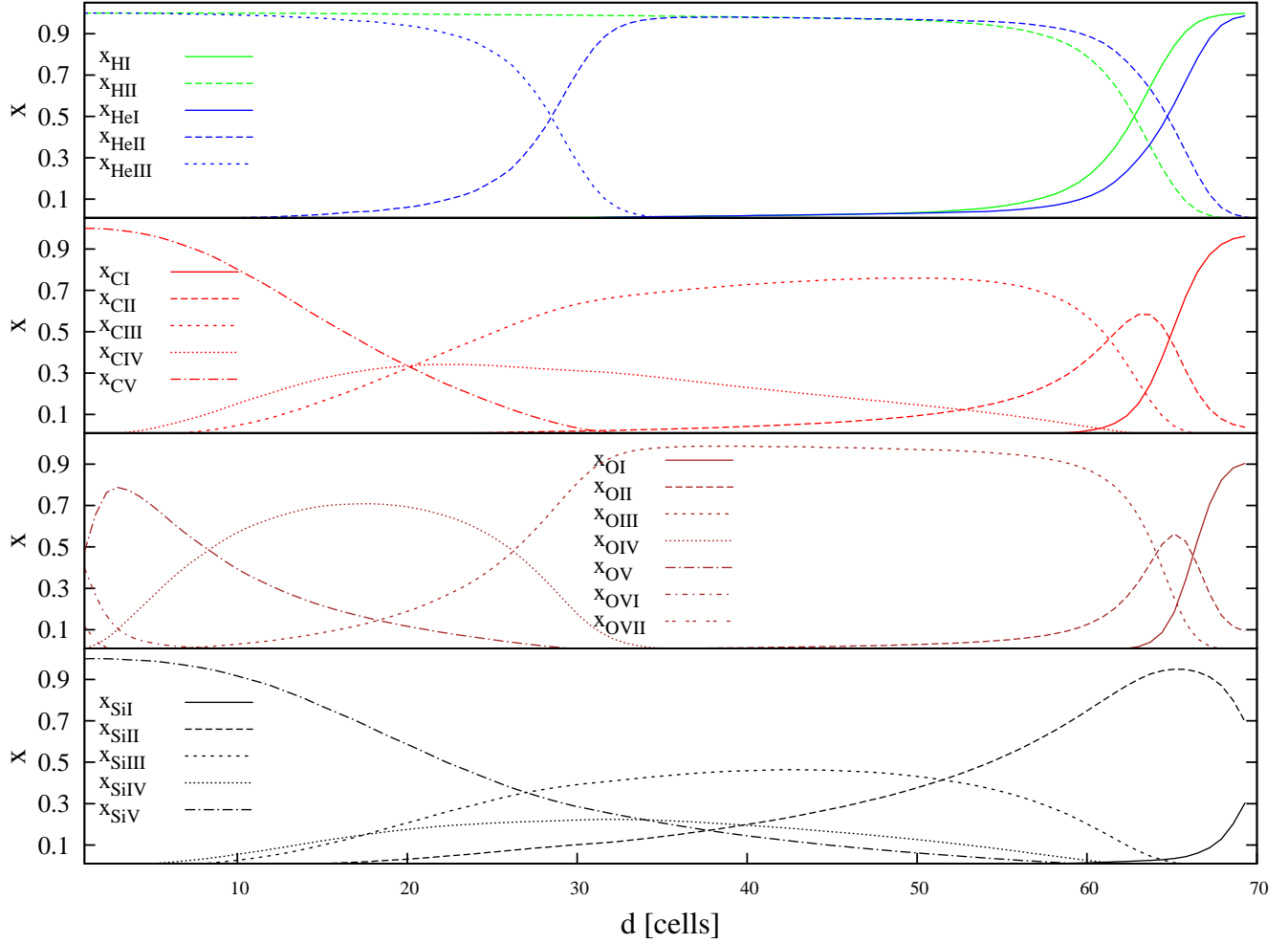


Figure 4.6: Fractions of the various components as function of distance d from the source in the run described in Test 1. The values are taken at simulation time $t = 5 \cdot 10^8$ yrs. From the top panel to the bottom the species are: H (green lines) and He (blue), C (red), O (brown) and Si (black). In each panel the same ionisation states are represented by the same line-styles: solid lines refer to the neutral components (e.g. O I), long dashed to the first ionisation state (e.g. O II), short dashed to the second ionisation state (e.g. O III), dotted to the third ionisation state (e.g. O IV), long dashed-dotted to the fourth ionisation state (e.g. O V), short dashed-dotted to the fifth ionisation state for O VI, and the sixth ionisation state is represented in dashed-spaced lines for O VII.

H fractions, while small discrepancies still remain in the He fractions. Such discrepancies are, on the other hand, always below 20 percent and remain limited to the small number of cells encompassing the ionisation fronts.

Hereafter all the variables in this Chapter will refer to values calculated at Step 3 and the superscript C^3 will be omitted to simplify the notation.

4.4.1.3 Metal ionisation states

I now analyze the behaviour of the metal ionisation states, plotted in Figure 4.6. As a reference, in the upper panel I report the evolution of x_{HI} , x_{HII} , x_{HeI} , x_{HeII} and x_{HeIII} . Before discussing the details of the Figure, it is necessary to point out that the balance among the different ions is established by the relative values of their ionisation potentials and by the values of their recombination coefficients. It also depends on the spectral distribution of the radiation field and its variations with the distance from the source, as induced by the radiative transfer effects. The complex interplay between these numerous processes makes the interpretation of the results non trivial; despite this, some trends have a straightforward interpretation.

Because of the small amount of metals included in this test, I expect their impact on the evolution of H and He to be negligible. This is confirmed from a comparison of the curves in the upper panel of the Figure to the corresponding curves in Figure 4.4, without metals. The maximum difference is 7 percent across the I-front of H II (compare top panel of Figure 4.6 line green dashed with top panel Figure 4.4 solid blue line). Effects on the ionisation fractions induced by an increase in the gas metallicity will be investigated in the next Section.

I now turn to analyse the behaviour of C in the second panel (from the top). Inside the HII region ($d < 29$ cells), C is in the form of C III, C IV and C V. Close to the source, for $d < 20$ cells, C V is by far the dominant species. This high ionisation level is obtained from a combination of collisional ionisation and photo-ionisation. The evolution of C III is very similar to that of He II because of the similar ionisation potentials (see Figure 4.2). The abundance of C IV, which is present throughout the HII region, is dictated by the evolution of C III and C V, and their relative recombination coefficients.

C IV extends over the entire HII region ($10 < d < 55$ cells) with x_{CIV} being always below 30 percent. For $d \gtrsim 30$ cells x_{CV} goes to zero because no more C IV ionising photons are available. The ionisation potential of C V is outside our frequency range (see Table 4.1) and thus higher ionisation states are not present. Because of the paucity of photons with $E > E_{\text{CIII}}$, at $d > 50$ cells only C III is present in large quantities with $x_{\text{CIII}} \sim 70\%$. Closer to $d \sim 63$ cells, similarly to what happens to H II and He II, also C III recombines into C II. Finally, outside of the HII region, only C I is present.

In the third panel (from top) the ions of the oxygen are shown. The ionisation potential for O VI is the highest photo-ionising energy available in the adopted spectrum. A very small fraction of O VII is in fact present in few cells around the source. In addition to photo-ionisation by photons with $E > E_{\text{OVI}}$, collisional ionisation contributes for 10 percent at $T \geq 7 \cdot 10^4[\text{K}]$ present at $d < 3$ cells. The presence of O VI, is more evident but it is

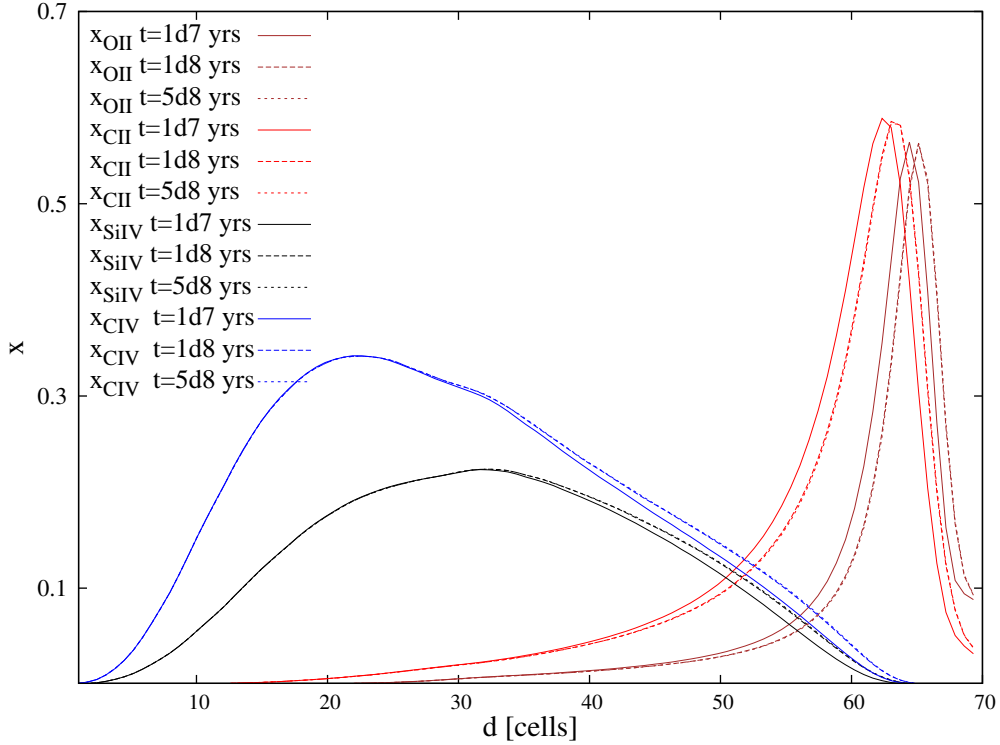


Figure 4.7: Time evolution of the ionisation fractions x_{OII} (brown lines), x_{CII} (red lines), x_{SiIV} (black lines), x_{CIV} (blue lines), as function of the distance from the source d in the reference run including metals. The values are taken at three tracking times $t_m = 10^7 \text{yr}$ (solid lines), 10^8yr (dashed lines), $5 \cdot 10^8 \text{yr}$ (short-dashed lines).

consistently limited to the inner region ($d < 8$ cells) of the ionised sphere and decreases rapidly with the distance from the source in favour of O V and O IV . For $d \gtrsim 30$ cells O III dominates the ionisation balance until it recombines into O II .

In the bottom panel the behaviour of the silicon ions is reported. Si V completely dominates the inner region of the Strömgren sphere ($d < 25$ cells) with a long tail extending up to the external region ($d \sim 55$ cells) where it is in equilibrium with lower ionised states. In the central region many ions are in equilibrium with a low ionisation fraction. Si III peaks at $x_{\text{SiIII}} \sim 0.4$ nearly at the center of the HII region ($d \sim 45$ cells), where it results to be in equilibrium with Si IV and Si II . The rising of Si II ($d > 52$ cells) finally dominates the outer region.

In general, it is possible to say that in the vicinity of the source the most abundant species are those with the higher ionisation state compatible with the maximum potential in the spectrum, i.e. H II , He III , C V , O V and Si V . Despite E_{OV} , E_{OVI} and E_{SiV} being covered by the spectrum, the abundance of photons at these energies is so low that x_{OVI} , x_{OVII} and x_{SiVI} are negligible. As the distance increases, the luminosity available for ionisation decreases, in particular for ions with high ionisation potential (see Figure 4.2).

This is reflected by the decrease of the abundance of these highly ionised states and the predominance of lower ionisation states (e.g. He II, C III, O III and Si III). Species like Si IV and C IV are always present, although they are not dominant, because the spectrum of the ionising radiation maintains energies higher than E_{SiIII} and E_{CIII} throughout the HII region (see Figure 4.2). At even larger distances ($d > 60$ cells) the dominant species are typically singly ionised metals and the neutral components.

While the discussion above refers to the final gas configuration, in Figure 4.7 I show the time evolution of C IV (blue lines), Si IV (black), C II (red) and O II (brown lines). The former two have an ionisation potential similar to that of He II, while the latter two are similar to He I (see Figure 4.2). The temporal evolution is shown at $t_m = 10^7$, 10^8 and $5 \cdot 10^8$ yrs. From the Figure it is clear that the profiles of the above species do not evolve much in time. In particular, the variations in x_{CIV} and x_{SiIV} are at most of a few percent while a larger evolution is observed for x_{CII} and x_{OII} as the ionisation front moves outwards.

4.4.1.4 Feedback by metals

In this Section I investigate the feedback of metals on the gas temperature by changing the gas metallicity Z_g . I have changed Z_g maintaining the relative abundance of C, O and Si. The runs considered in this test are shown in Figure 4.8 and they have metallicities $Z_g = 0.006$ (reference case in blue solid line), 0.01 (blue dotted-long dashed), 0.064 (brown solid), 0.1 (brown dotted-long dashed), 0.638 (red solid), 1.0 (red dotted-long dashed), 1.267 (black solid) and $2Z_\odot$ (black dotted-long dashed).

This Figure shows the values of the temperature ratio $\delta T/T$ defined as:

$$\delta T/T \equiv \frac{T(0) - T(Z_g)}{T(0)}, \quad (4.4)$$

where $T(0)$ is the value of the electron temperature (as function of the distance d) relative to a configuration with $Z_g = 0$. The ratio in Equation 4.4 can be interpreted as temperature deviation from the values at zero metallicity; it is then directly linked to the metal cooling efficiency.

The reference case (solid blue line) does not show any significant metal cooling, with the exception of the region near the source ($d < 5$ cells) where recombination of high ionisation states of C, O and Si, is more significant, inducing an average $\delta T/T \sim 10\%$. Temperature deviations at the He II I-front ($d > 65$ cells), where the ionising radiation is very faint, are also present, with $\delta T/T < 10\%$.

Increasing the metallicity to one percent solar (blue dotted-long dashed line) does not change the situation. Only at $Z_g = 0.064Z_\odot$ (brown solid line) some cooling is visible at each distance. In few cells near the source $20\% < \delta T/T < 40\%$, while $\delta T/T$ remains below 10 percent at $d > 10$ cells.

The shape of the $\delta T/T$ curve remains very similar up to $Z_g = 0.1Z_\odot$ (brown dotted-long dashed line).

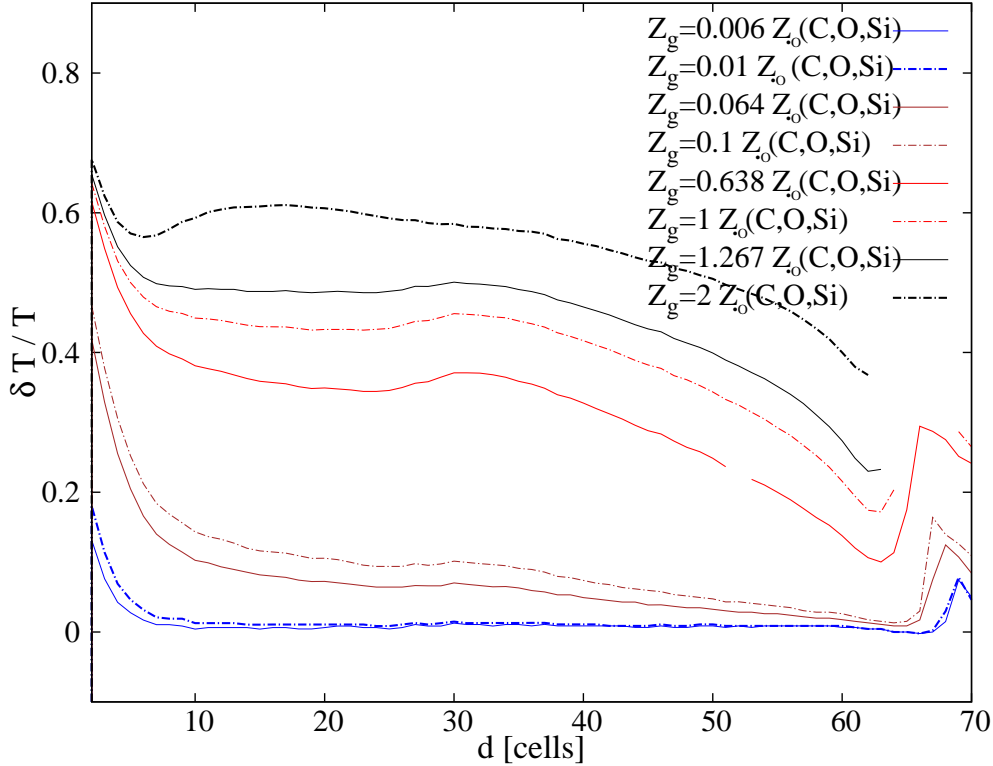


Figure 4.8: Metal cooling studied as ratio $\delta T/T$ (see the definition in the text) as function of the distance d from the source at simulation time $t_f = 5 \cdot 10^8 \text{yr}$. The various curves refer to an increase of the gas metallicity Z_g with respect to the reference run; in this Figure the gas is enriched only by C, O, Si. The metallicity values are: $Z_g = 0.006 Z_\odot$ (blue solid, reference value), $Z_g = 0.01 Z_\odot$ (blue dotted-long dashed), $Z_g = 0.064 Z_\odot$ (brown solid), $Z_g = 0.1 Z_\odot$ (brown dotted-long dashed), $Z_g = 0.638 Z_\odot$ (red solid), $Z_g = 1.0 Z_\odot$ (red dotted-long dashed), $Z_g = 1.267 Z_\odot$ (black solid), $Z_g = 2 Z_\odot$ (black dotted-long dashed).

For $Z_g \geq 0.638 Z_\odot$ (red solid line), a temperature decrease (i.e. an increase in $\delta T/T$) is sensitively present at every distance: in the inner region ($d < 5$ cells) the deviation exceeds 40 percent; it then remains at $\delta T/T \sim 40\%$ up to $d \sim 30$ cells. Beyond this distance, the ratio $\delta T/T$ progressively decreases to 17 percent in the outer region ($d \sim 64$ cells). At this metallicity some episodic CRASH3 instabilities occur⁴, as marked by the absence of data in two cells ($d = 52, 53$); the missing values can be derived by interpolation because of the regular trend in the other cells.

In the solar and super-solar range ($Z_g \geq 1 Z_\odot$) the deviation is $\delta T/T > 50\%$ in the

⁴In practice, a limited number of Cloudy calculations present many temperature convergence warnings and they are rejected by the internal checks at Step 3 of the pipeline. A deeper investigation shows that the Cloudy configurations are correctly evaluated in these cells and the automatic rejections can be neglected.

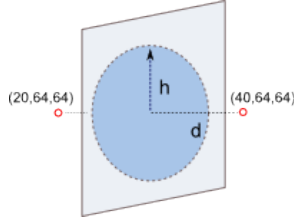


Figure 4.9: Sketch of the geometrical set-up used for Test 2.

Sim. Name	\dot{N}_1 [phot s $^{-1}$]	\dot{N}_2 [phot s $^{-1}$]	T_1 [K]	T_2 [K]
$\dot{N}_{var}T_{fix}$	$[3, \dots, 9] \cdot 10^{51}$	$[3, \dots, 9] \cdot 10^{51}$	10^5	10^5
$\dot{N}_{fix}T_{var}$	$9 \cdot 10^{51}$	$9 \cdot 10^{51}$	$[5, 10, 50] \cdot 10^4$	$[5, 10, 50] \cdot 10^4$
$\dot{N}_{1fix}\dot{N}_{2var}T_{fix}$	$9 \cdot 10^{51}$	$[3, 7, 9] \cdot 10^{51}$	10^5	10^5
$\dot{N}_{fix}T_{1fix}T_{2var}$	$9 \cdot 10^{51}$	$9 \cdot 10^{51}$	10^4	$[5, 10] \cdot 10^4$

Table 4.2: Grid of simulations used to test the metal ions in the bubble overlap. The simulation sub-grid names contain the subscript *fix* or *var* to indicate the physical quantity which changes or remains fixed in the simulation grid.

inner region, and exceeds 40 percent up to $d \sim 45$ cells, confirming the dominant role played by the metal cooling. It is necessary to consider the cases with $Z_g > 1Z_\odot$ only as indicative because in this metallicity regime the metal contribution to the absorption cannot be neglected and the assumptions of the method fail.

The absence of data at distances $d > 65$ cells is due to the lack of a convergent solution of CRASH3 at low luminosity and high metallicity.

4.4.2 Test 2: metal fluctuations in a HII region overlap

This is an extension of Test 1, in which I study the behaviour of metals in the HII region overlap produced by two point sources located in cell (20, 64, 64) and (40, 64, 64). This geometrical set-up is sketched in Figure 4.9.

The sources ionising rates are \dot{N}_1 and \dot{N}_2 and their associated black body spectral temperatures are T_1 and T_2 . The box is the same of Test 1, but now the gas number density is $n_{gas} = 1\text{cm}^{-3}$, to obtain a sharper overlap profile.

Because in this test I am interested in studying the behaviour of metals only in the overlap region, I concentrate on the plane corresponding to $x = 30$ (dark blue circle in Figure 4.9).

In the following I will discuss the ionisation fractions of the metals and the gas temperature as function of the source characteristics by using a grid of simulations combining different values of \dot{N}_1 , \dot{N}_2 , T_1 and T_2 , as summarized in Table 4.2. All the values in the following discussion refer to the final simulation time.

The sub-grid $\dot{N}_{var}T_{fix}$ is obtained by simultaneously changing the source ionising rates in the range $\dot{N}_1 = \dot{N}_2 = (3 \cdot 10^{51} - 9 \cdot 10^{51})[\text{phot s}^{-1}]$, while the spectrum temperature is

maintained fixed at the reference value $T = 10^5$ [K].

The combination $\dot{N}_1 = \dot{N}_2 = 9 \cdot 10^{51}$ [phot s⁻¹], is considered as reference case (see Section 4.4.2.1). Notice that the decrement in the source rates is taken deliberately small (they never vary by more than an order of magnitude) because this set of simulations is intended to test the **CRASH3** sensitivity to small variations in the source ionisation rates.

The sub-grid $\dot{N}_{fix}T_{var}$ represents the specular case to the previous one. In this set-up both spectrum temperatures of the sources vary simultaneously, spanning an order of magnitude, while the source ionisation rates remain fixed at the maximum reference value $\dot{N}_1 = \dot{N}_2 = 9 \cdot 10^{51}$ [phot s⁻¹].

$\dot{N}_{1fix}\dot{N}_{2var}T_{fix}$ and $\dot{N}_{fix}T_{1fix}T_{2var}$ are mixed cases in which only one source is allowed to change in ionisation rate or spectral temperature, respectively. These latter cases allow to test any asymmetric variation with respect to the symmetric cases in the previous sub-grids.

4.4.2.1 Reference case

I first describe a single set-up which I use as reference case to study the properties of the overlap. Here I consider two identical sources with fixed ionisation rates $\dot{N}_1 = \dot{N}_2 = 9 \cdot 10^{51}$ [phot s⁻¹] and a fixed spectrum temperature $T_1 = T_2 = 10^5$ [K].

Similarly to the Test 1, here I show the results by averaging the physical quantities on all the cells of the plane at the same distance h from the cell (30,64,64) (see Figure 4.9).

In Figure 4.10 the resulting ionisation fractions and temperature are shown. The ions of hydrogen and helium (dashed lines) are reported in the top panel. $x_{\text{HIII}} = 1$ and $x_{\text{HeII}} = 1$ up to $h \sim 13$ cells; as for a single Strömgen sphere (see Test 1), the region beyond the I-front of the overlap is characterized by the presence of He II. x_{HeIII} is limited to few percents because it is always confined in regions very close to the sources and then it is not shown in the panel⁵.

In the second panel (from the top) the ionisation fractions of C II, C III, O II, O III, Si II and Si III are shown together because they trace the external regions of the Strömgen spheres (see Figure 4.6) creating the overlap.

C III, O III and Si III are present for $h < 12$ cells with different ionisation fractions $x_{\text{OIII}} \sim 1$, $x_{\text{CIII}} \sim 0.5$, $x_{\text{SiIII}} \sim 0.3$, indicating that these ions have a different sensitivity to the ionising field; this is also in qualitative agreement with the relative trends noticed in Test 1 (Figure 4.6). Their recombination fronts are distributed between $h = 13$ and $h = 14$ cells, and are wider compared to those of hydrogen and helium case (top panel).

The values of their ionisation fractions are compatible with the case of a single sphere, indicating the low overlapping degree of the two bubbles.

In the third panel (from top) the fractions of the fourth ions of C and Si, together with Si V are shown. The ions Si IV, Si V and C IV are present with low ionisation fractions (less than 0.5). While x_{SiV} and x_{CIV} cut their initial values by half up to $h = 12$ cells (i.e.

⁵The lines in the Figures are evaluated by using a c-spline algorithm which causes an unphysical interpolation in the cell before the recombination front. This should be considered as a graphical issue because by definition the fractions shown in the plots are less or equal than one.

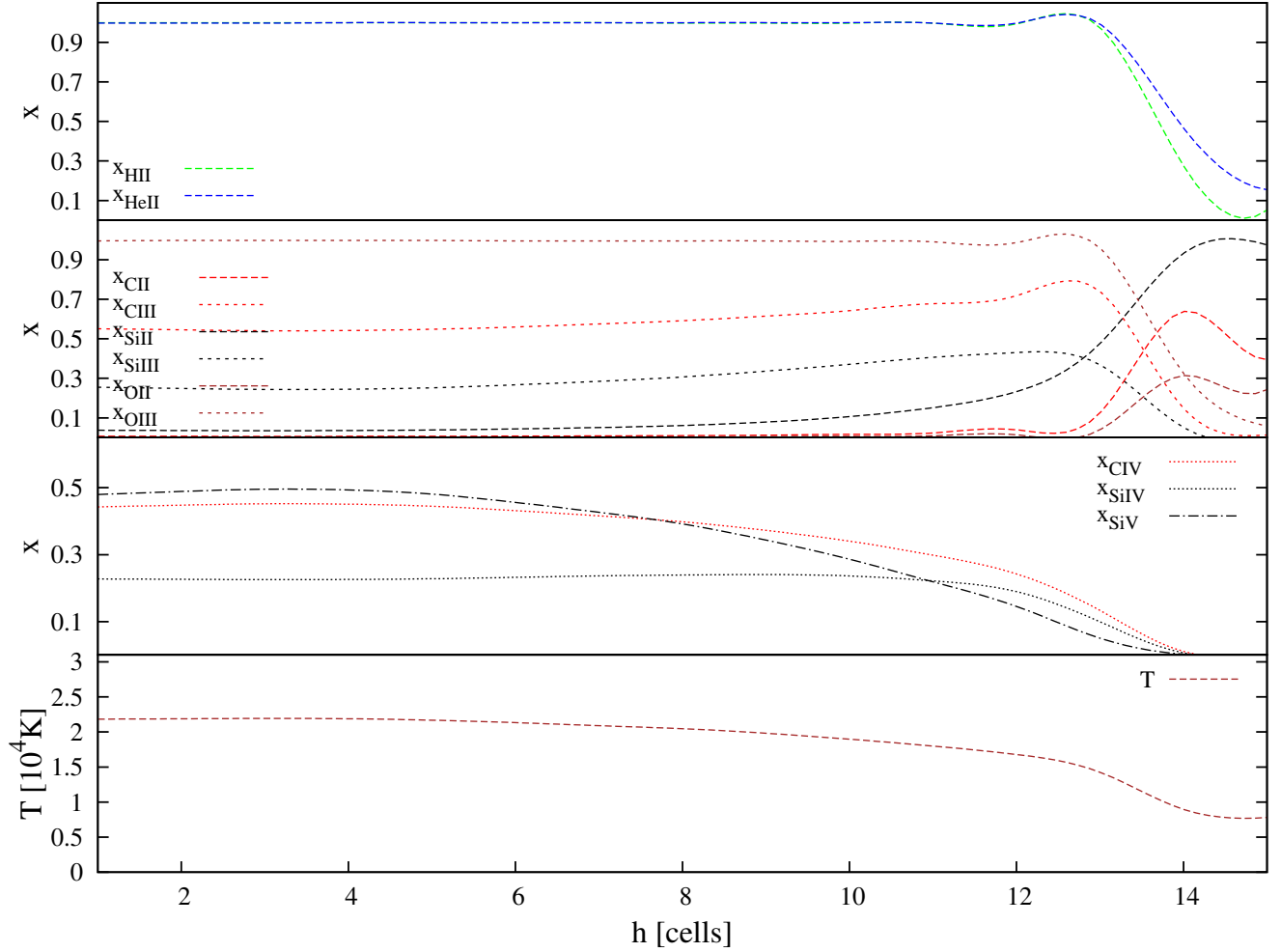


Figure 4.10: Fractions of H, He, C, O, Si and gas temperature as function of h , evaluated in the plane equidistant from the two sources ($x = 30$), in the reference case. **Top panel:** x_{HII} (green dashed), x_{HeII} (blue dashed). **Second panel** (from top): x_{CII} (red dashed) and x_{CIII} (red short-dashed); x_{SiII} (black dashed) and x_{SiIII} (black short-dashed). The fraction x_{OII} is reported in dashed brown lines and the values for x_{OIII} as brown short-dashed lines. **Third panel** (from top): x_{CIV} (red dotted). The fraction x_{SiIV} is reported as dotted black line and x_{SiV} as dashed-dotted black line. **Bottom panel:** gas temperature T (brown dashed).

with the decrease of the ionising field), x_{SiIV} remains constant at $x_{\text{SiIV}} \sim 0.25$ and does not increase with the recombination of SiV . After $h \sim 13$ cells it starts decreasing with the other ions and rapidly recombines in SiIII and SiII . The absence of OIV , OV and CV (few percents are present in the data) in this panel is in agreement with the fact that HeIII is not present in the region (see top panel).

The value of the temperature is finally shown in the bottom panel up to the value of h in which high ionisation states (e.g. SiIV) are also present. Inside the overlap it remains constant at $T \sim 2 \cdot 10^4 \text{ K}$, with a final drop at the I-front ($h > 13$ cells); these values are compatible with a photo-ionisation equilibrium dominated by a diffuse radiation field.

4.4.2.2 Variations in the source ionising rates

In this Section I discuss the trends obtained for the cases with varying ionisation rates.

In the sub-grid $\dot{N}_{var} T_{fix}$ I have decreased the ionisation rates of the two sources simultaneously. Because the sources are identical, I expect a regular decrease of the bubble overlap. This is clearly shown by this test because the H and He I-fronts are closer to the sources and their size, compared to the reference case, is decreased by 52 percent when \dot{N} decreases from $\dot{N} = 9 \cdot 10^{51} \text{ phot s}^{-1}$ to $\dot{N} = 3 \cdot 10^{51} \text{ phot s}^{-1}$.

I also verified that the lowest ionisation states of all the metals follow the same trend of the reference case in all the sub-grid with x_{SiIII} and x_{CII} regularly tracing the recombination front regression. A regular decrease in x_{CIV} and x_{SiIV} can also be verified in the internal region of the overlap; remarkably, x_{CIV} appears more sensitive than x_{SiIV} in every case. Finally, a regular decrease of the temperature T in the overlap (about 25 percent comparing the values of the extreme cases in the sub-grid) is also confirmed.

From the results of this sub-grid I can conclude that CRASH3 predicts a regular behaviour of the ions in the gas and it is very sensitive also to small changes in the source ionisation rates.

In a second series of runs (sub-grid $\dot{N}_{fix} \dot{N}_{2var} T_{fix}$ in Table 4.2), I have kept one source fixed at the reference ionisation rate \dot{N}_1 , while varying the second with values $\dot{N}_2 = 3 \cdot 10^{51}, 7 \cdot 10^{51}, 9 \cdot 10^{51} \text{ phot s}^{-1}$. These simulations allow to comment on the dependence of the metal ionisation states on asymmetries in the radiation field. The results are shown in Figure 4.11.

In the top panel I show x_{HII} (green lines), x_{HeII} (blue lines) as function of h . Hereafter I indicate the combination $\dot{N}_1 = 9 \cdot 10^{51}$, $\dot{N}_2 = 3 \cdot 10^{51}$ as (9 – 3) for the sake of brevity, and similarly for the other combinations: (9 – 3) (reported in short-dashed lines), (9 – 7) (dashed lines), and the reference cases (9 – 9) (solid lines).

As in the previous case CRASH3 can record a small decrease in the ionisation rate of one source by a regular regression of the HII and HeII I-fronts. The HeII I-front for example, moves from $h \sim 13$ in the reference case (solid lines) to $h \sim 11$ cells in the case (9 – 3) (blue short-dashed lines).

In the middle panel the ionisation fraction x_{CIV} (red lines) is shown as function of h with the same line-styles conventions of the previous case. By comparing the run (9 – 3) (red short-dashed) with the reference one (red solid), the distance where CIV starts recombining

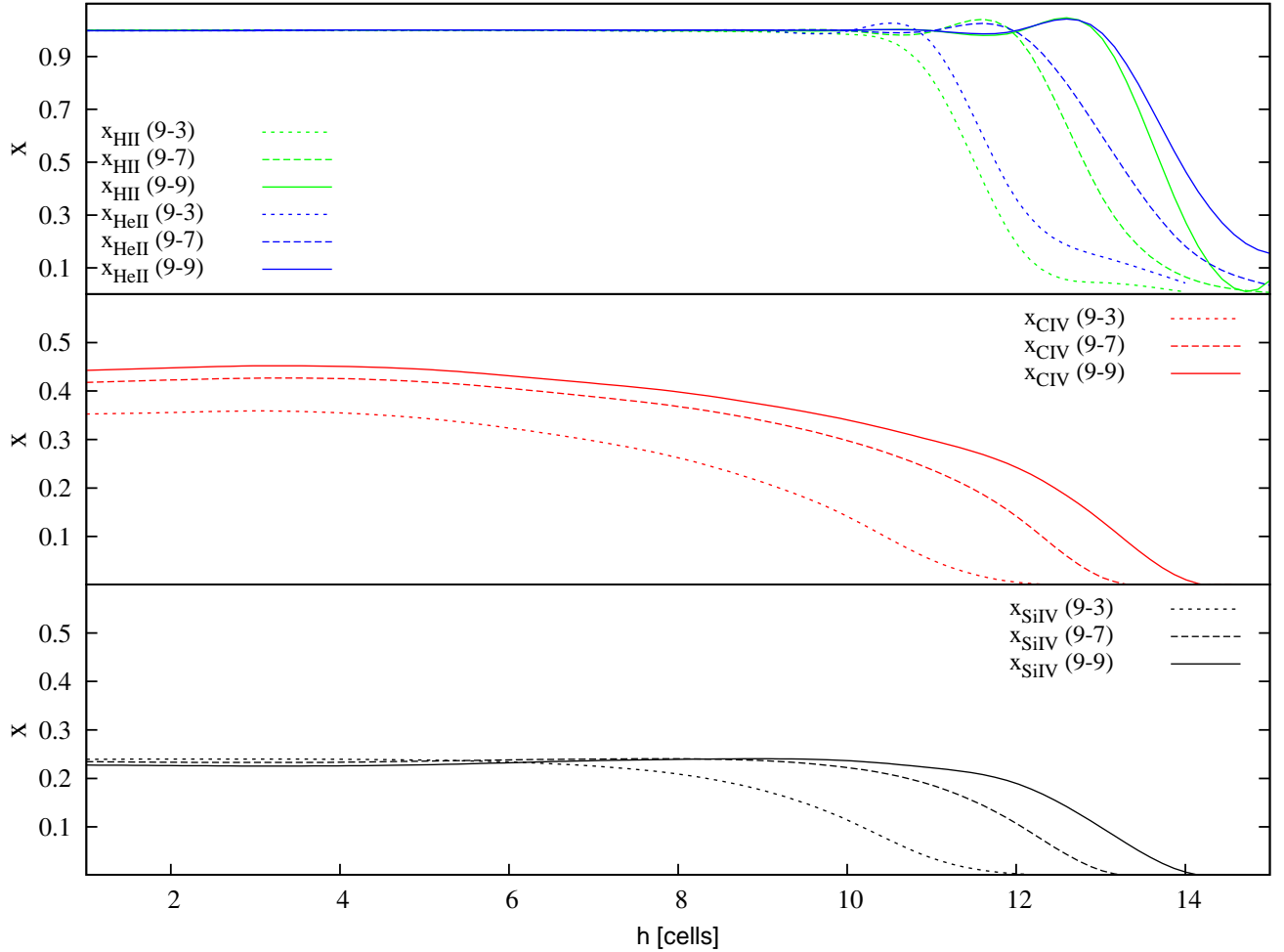


Figure 4.11: Ionisation fractions x_{HII} (green lines), x_{HeII} (blue lines), x_{CIV} (red lines) and x_{SiIV} (black lines) as function of h in the sub-grid $\dot{N}_1 \dot{N}_2 \dot{N}_3 T_{\text{fix}}$ (see Table 4.2). The solid line-style refers to the reference case $\dot{N}_1 = \dot{N}_2 = (9 - 9)$; the dashed to $(9 - 7)$ and the short-dashed to $(9 - 3)$. See text for details. The values refer to the plane $x = 30$ in all the cases. **Top panel:** x_{HII} , x_{HeII} . **Middle panel:** x_{CIV} . **Bottom panel:** x_{SiIV} .

regularly decreases of about 2 cells, while the value of x_{CIV} increases of about 28 percent in the inner region ($h < 6$ cells).

The bottom panel shows x_{SiIV} as function of h in black with same line-style conventions. In the inner region ($h < 6$ cells) x_{SiIV} is insensitive to the small variations of \dot{N}_2 , while its behaviour at the recombination front is consistent with x_{CIV} (previous panel). A similar displacement of the fronts as \dot{N}_2 decreases, can be noticed by comparing the middle and bottom panels.

Finally, I can summarise the results in the sub-grid $\dot{N}_{1fix}\dot{N}_{2var}T_{fix}$ saying that CRASH3 is sensitive also to small and asymmetric variations of the ionisation rates: the fronts of all the species register these variations by a regular regression in their positions, while only the ion C IV shows deviations in its ionisation fraction.

4.4.2.3 Variations in the source spectra

In this Section I study the variations induced in the ionisation fractions by changes in the temperatures T_1 and T_2 of the black body spectra. The source ionisation rates are set to the reference value $\dot{N}_1 = \dot{N}_2 = 9 \cdot 10^{51} \text{phot s}^{-1}$.

In Figure 4.12 the ionisation fractions in the sub-grid $\dot{N}_{fix}T_{var}$ are reported for the H, He (top panel), the ion C IV (middle panel) and the ion Si IV (bottom panel). The line styles refer to different black body temperatures: the case $T_1 = T_2 = 5 \cdot 10^4 \text{K}$ is reported as dashed, $T_1 = T_2 = 10^5 \text{K}$ as solid (this is also the reference case in 4.4.2.1) and $T_1 = T_2 = 5 \cdot 10^5 \text{K}$ as short-dashed lines. Because in this Section $T_1 = T_2$, for the sake of brevity, hereafter the variable T will refer to the black body temperature of both sources.

In the top panel x_{HII} is shown in green lines; x_{HeII} in blue lines and x_{HeIII} in brown lines. The H II I-front is identical in the cases $T = 5 \cdot 10^4 \text{K}$ and $T = 10^5 \text{K}$, while it recedes significantly (about 4 cells) in the case $T = 5 \cdot 10^5 \text{K}$. Note also that the shape of the I-front of He II is very sensitive to the spectral changes. At $T = 5 \cdot 10^5 \text{K}$ (short-dashed lines) in fact, the He II recombination front changes also in its shape and, because of the harder photons in this spectrum, also He III (brown short-dashed line) becomes present for $h \lesssim 12$ cells. This ion is not present in the reference case, as shown by the absence of a brown solid line. This remarkable change can be easily understood considering that the induced variation on the spectral shape moves the bulk of the energy to higher frequencies.

In the middle panel I show the values of x_{CIV} as function of h (red lines) with the same conventions for the line-styles used in the top panel. In the inner region ($h < 6$ cells), x_{CIV} shows a significant increment when the spectrum temperature changes from $T = 5 \cdot 10^4 \text{K}$ to $T = 10^5 \text{K}$, varying from $x_{\text{CIV}} \sim 0.05$ to $x_{\text{CIV}} \sim 0.4$. The shape of the recombination front is also changed in the case $T = 5 \cdot 10^5 \text{K}$, where a bump in the ionisation fraction is present at $h = 10$ cells, before the front starts decreasing.

The bottom panel shows x_{SiIV} with the usual line-style definitions. In this case, unlike the previous tests, Si IV shows remarkable changes over h and by varying the spectrum temperature. As in the previous panel a bump in the value of the ionisation fraction is present at $h = 10$ cells in the case $T = 5 \cdot 10^5 \text{K}$. Moreover, x_{SiIV} decreases from $x_{\text{SiIV}} \sim 0.22$ to $x_{\text{SiIV}} \sim 0.08$ in the inner region of the overlap, if T is increased from $T = 10^5 \text{K}$ and

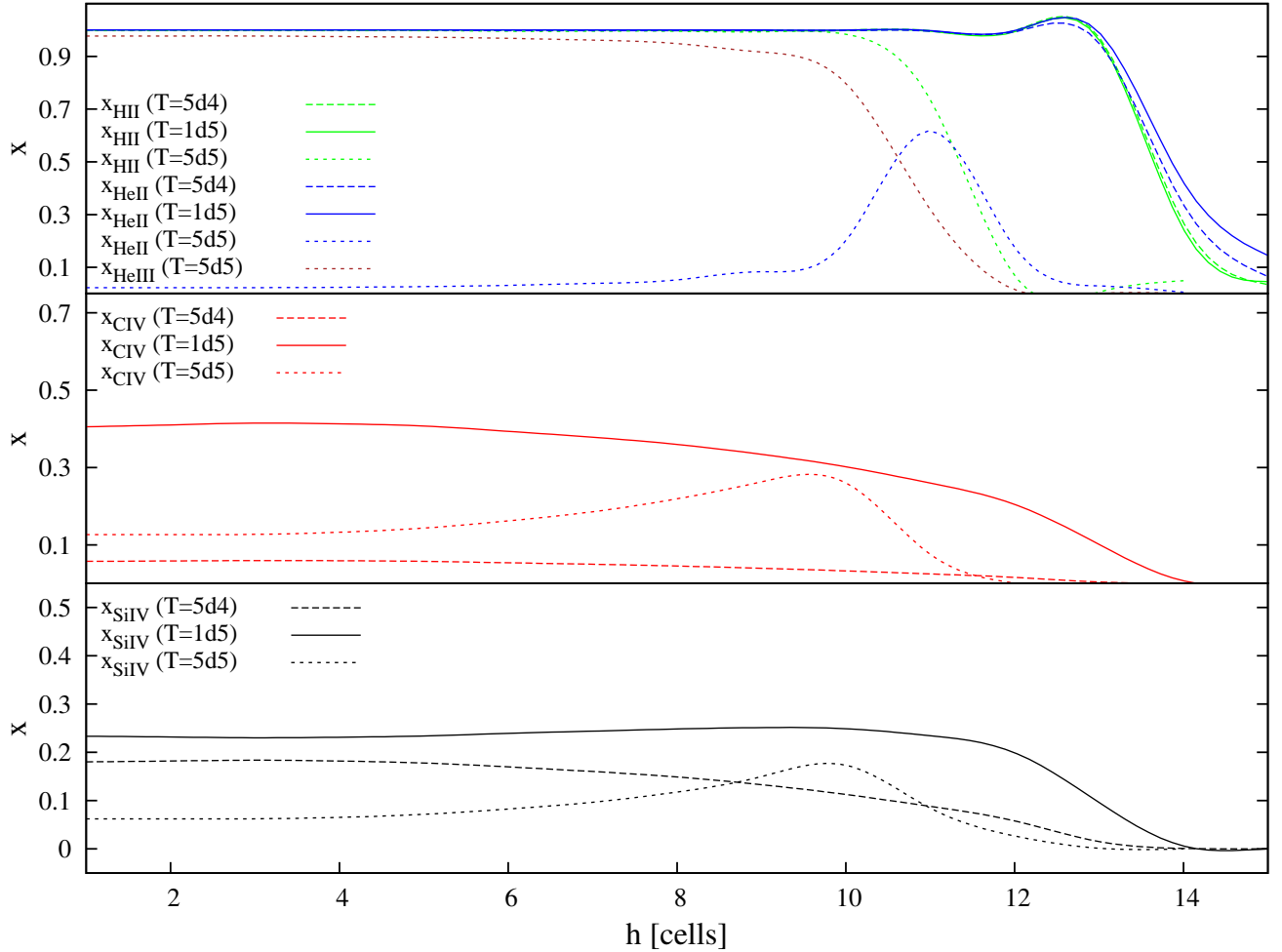


Figure 4.12: Ionisation fractions x_{HII} (green lines), x_{HeII} (blue lines), x_{HeIII} (brown lines), x_{CIV} (red lines) and x_{SiIV} (black lines) as function of h in the sub-grid $N_{\text{fix}}T_{\text{var}}$ (see Table 4.2). The solid line-style refers to the reference case $T = 10^5\text{K}$; the dashed to $T = 5 \cdot 10^4\text{K}$ and the short-dashed to $T = 5 \cdot 10^5\text{K}$. **Top panel:** x_{HII} , x_{HeII} , x_{HeIII} . **Middle panel:** x_{CIV} . **Bottom panel:** x_{SiIV} .

$$T = 5 \cdot 10^5 \text{K}.$$

The idealised tests summarised in Table 4.2 confirm the **CRASH3** sensitivity to the distortions of the radiation field induced by changes in the source ionisation rates and spectra. The **CRASH3** pipeline can then accurately detect and trace such fluctuations in space (Test 2) and time (Test 1).

In realistic cases, where the metals are spread out in the complex structure of the cosmic web, such large fluctuations could be reduced by less variability in the source properties and by density changes in the cosmic gas. On the other hand, the idealized tests proposed in this Section confirm that in simple and intuitive cases, the **CRASH3** pipeline correctly detects the radiation field variations. Moreover, the induced changes in the source properties are correctly reflected by metal ions taking advantage of their high sensitivity.

4.4.3 Test 3: Radiative transfer on a cosmological density field enriched by metals

In this Section I present a variant of the TEST 4 proposed in the Comparison Project ([124, 157]). The original test set-up has been adopted, but I have extended the ICs to include He, C, O and Si as required by **CRASH3** (see 4.3.1). For reference, the box size is $L_b = 0.5h^{-1}\text{Mpc}$ comoving, $N_c = 128$, the simulation duration is set to $t_f = 4 \cdot 10^5 \text{yrs}$, starting at redshift $z = 9$. The cosmological evolution of the box is disabled and the simulation starts with a neutral gas at initial temperature $T_0 = 100\text{K}$. The H and He fractions are the same as in Test 1 and [157].

In the box, 16 point sources are present with a black body spectrum at $T = 10^5\text{K}$. The sampling of the spectrum is done with 91 frequencies, to reach the accuracy established in our Test 1. Finally, I have run the test with 10^8 packets to ensure a good convergence as done in [157].

It is important to note that the aim of this test is to show how the full **CRASH3** pipeline is applied to a realistic density snapshot; this is done by describing the practical implementation of every Step in 4.3. It is not intended instead, to derive any physical result from the RT simulation. The metal ions are then shown only to give an idea of the rich set of information provided by **CRASH3**.

Differently from the previous tests in which I populated the full computational volume with metals, here I assign a metallicity of $Z_g = 0.006\Delta Z_\odot$ to those cells with an over-density $\Delta = \rho/\langle\rho\rangle > 10$. This results in about 5 percent of metal enriched cells. The number density of C, O and Si, relative to the hydrogen, are set up according to the standard solar composition, as introduced in 4.4.

In Figure 4.13 I show the distribution of the C I number density in a slice of the simulation box containing the brightest source (notice the largest over-dense region in Figure). The distribution of Si I and O I is the same, with $n_{\text{Si I}} = 0.142 \cdot n_{\text{C I}}$ and $n_{\text{O I}} = 2 \cdot n_{\text{C I}}$.

By construction, most of the metals are concentrated in the vicinity of the sources and in general in the highest density regions.

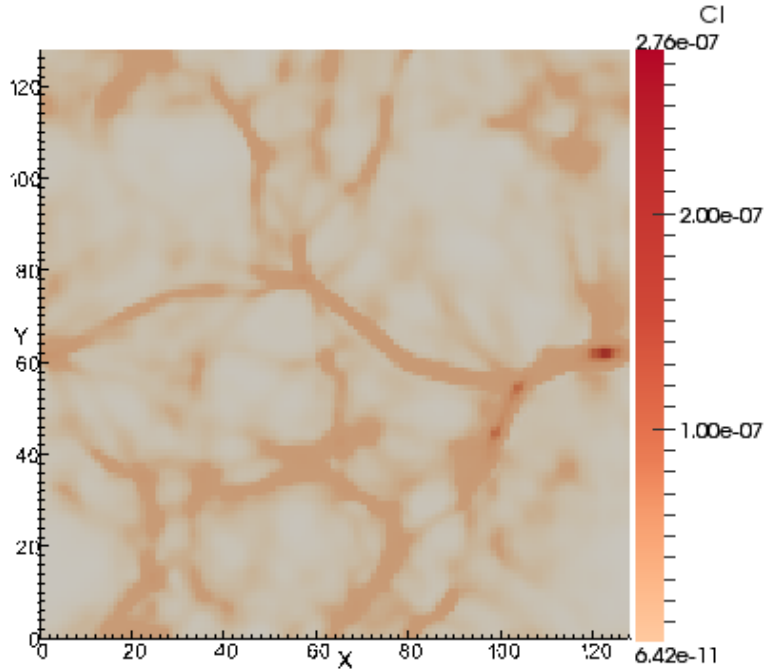


Figure 4.13: Number density map $n_{\text{CI}} [\text{cm}^{-3}]$ of C I (white to red colour gradient), in the selected slice.

As shown in Figure 4.8 of Test 1, only gas with super-solar metallicity substantially affects the cooling function. In this box this corresponds to those cells with $\Delta > 100$, which are only 0.012 percent of the total number. For this reason, in this test I ignore the effect of metal cooling in discussing the results. This question is in fact of primary importance but requires a physically motivated enrichment to draw any conclusion and I will discuss it in future realistic applications.

The second Step of the **CRASH3** pipeline consists in running a standard RT simulation. In Figure 4.14 I show the map of T in the slice by using a blue (low temperature) to red (high temperature) colour gradient. Blue regions ($T = 100\text{K}$) correspond to areas not reached by the radiation field, while light blue patterns clearly trace the He II ionisation fronts at a typical temperature of $T = 2 \cdot 10^4\text{K}$.

The green pattern spatially dominates in the slice indicating a typical temperature of the ionised H I and He I of about $T = 4 \cdot 10^4\text{K}$. Temperatures $T = 5 \cdot 10^4\text{K}$ (yellow areas) trace the gas filaments departing from the sources, while gas fronts with temperatures up to $T \sim 6.8 \cdot 10^4\text{K}$ (red areas) are clearly shown in the map but they are not directly connected with the sources. These last regions could derive from complex tridimensional effects due to the RT in the cosmic web or to the presence of clustered sources not intercepted by the slice. This deduction is confirmed by statistically tracing the distribution of the He III, because as I have shown in the previous Tests 1 and 2, this ion traces cells close to the point sources.

The results of the **CRASH3** pipeline are summarized in Figures 4.15 and 4.16 for the ions

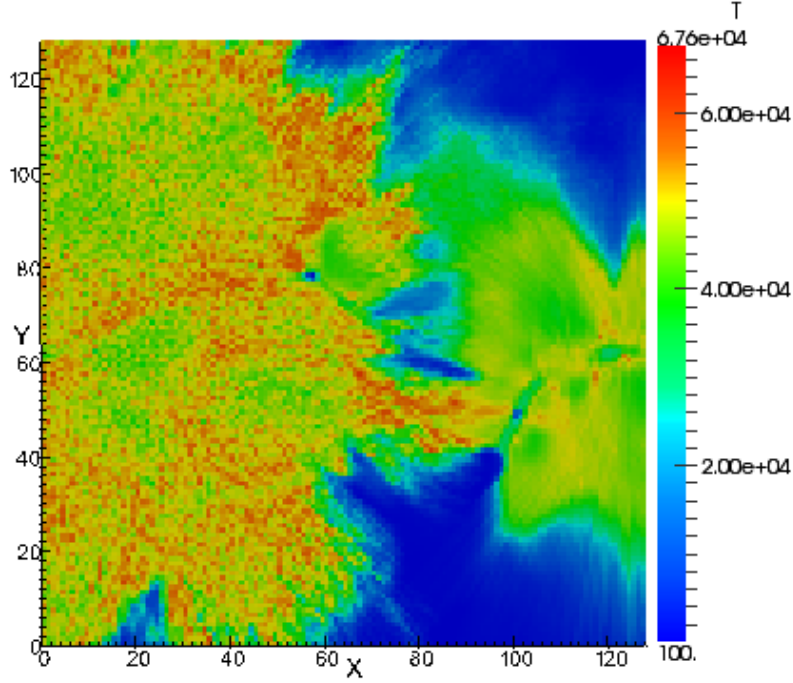


Figure 4.14: Temperature map T [K] of the gas (blue to red colour gradient), in the selected slice.

C_V and C_{III} , in Figures 4.17 and 4.18 for the same ions of oxygen, and the same for silicon is shown in Figure 4.19 and 4.20. All the Figures refer to the usual slice.

Figure 4.15 shows a spatial distribution of C_V , by representing its ionisation fraction value from black to yellow. Along the filament and far from the source small traces of C_V are present with ionisation fraction always below $x_{CV} \sim 0.1$. Moving along the filament, towards the source x_{CV} progressively increases up to $x_{CV} \sim 0.8$. C_V is then fully ionised (yellow colour) in the cell containing the source.

In Figure 4.16 I show the values in space of x_{CIII} with the same colour gradient but notice that in this case x_{CIII} never exceeds ~ 0.8 . C_{III} is highly pervasive in those regions dominated by photo-ionisation equilibrium, in fact most of the enriched cells shown in this Figure have $x_{CIII} \gtrsim 0.6$. A comparison with the typical gas temperatures (in these regions $T \sim 5 \cdot 10^4 K$) shown in Figure 4.14, further confirms this conclusion. Near the source the intricate spatial pattern of the ion shows a decrease to $x_{CIII} \sim 0.4$ and its disappearance in the cell where the source is located.

A further comparison with the simple case of Test 1 can help in establishing the correctness of these results. In fact, I show the carbon ions C_V and C_{III} because in Test 1 I have learned that they are present at different distances from the source originating the Strömgren sphere and in this way they trace disconnected regions. Figure 4.6 shows in fact, that their presence in space is complementary along the distance from the point source. This fact is confirmed by comparing Figure 4.15 and Figure 4.16. Where C_V is

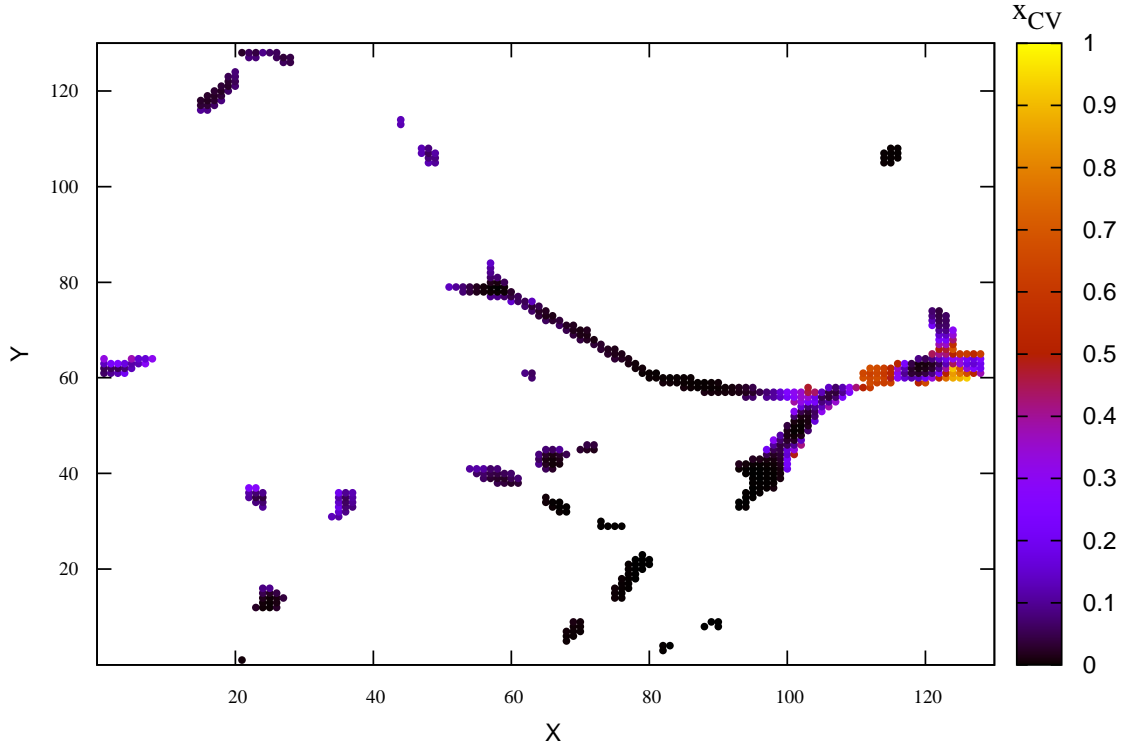


Figure 4.15: Test 3: map of x_{CV} in black to yellow gradient, scale from 0 to 1.

present with a high value of the ionisation fraction, C_{III} disappears and vice versa. This occurs, for instance in the region $60 < X < 80$, $60 < Y < 80$ which traces the end of the visible filament.

A similar behaviour can be confirmed by comparing the Figures showing O_{V} (Figure 4.17) and O_{III} (Figure 4.18), and by comparing Si_{V} in Figure 4.19 with Si_{III} in Figure 4.20.

The test proposed in this Section clearly shows that **CRASH3** can be successfully applied to a realistic gas density snapshot enriched by metals. The flexibility of the pipeline also helps in achieving both detailed and statistical analysis exploiting the database support implemented at Step 3. A full statistical analysis will be made in future works based on realistic simulations including self-consistent metal enrichment (see 2.2.2).

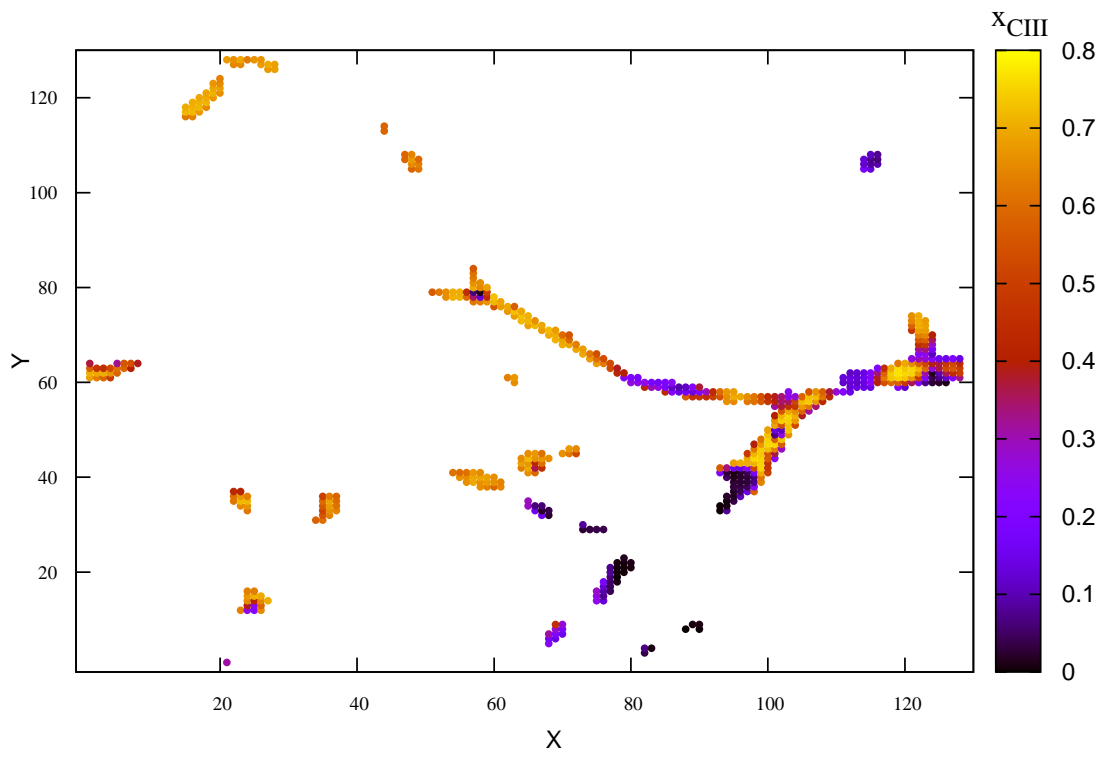


Figure 4.16: Test 3: map of x_{CIII} in black to yellow gradient, scale from 0 to 0.8.

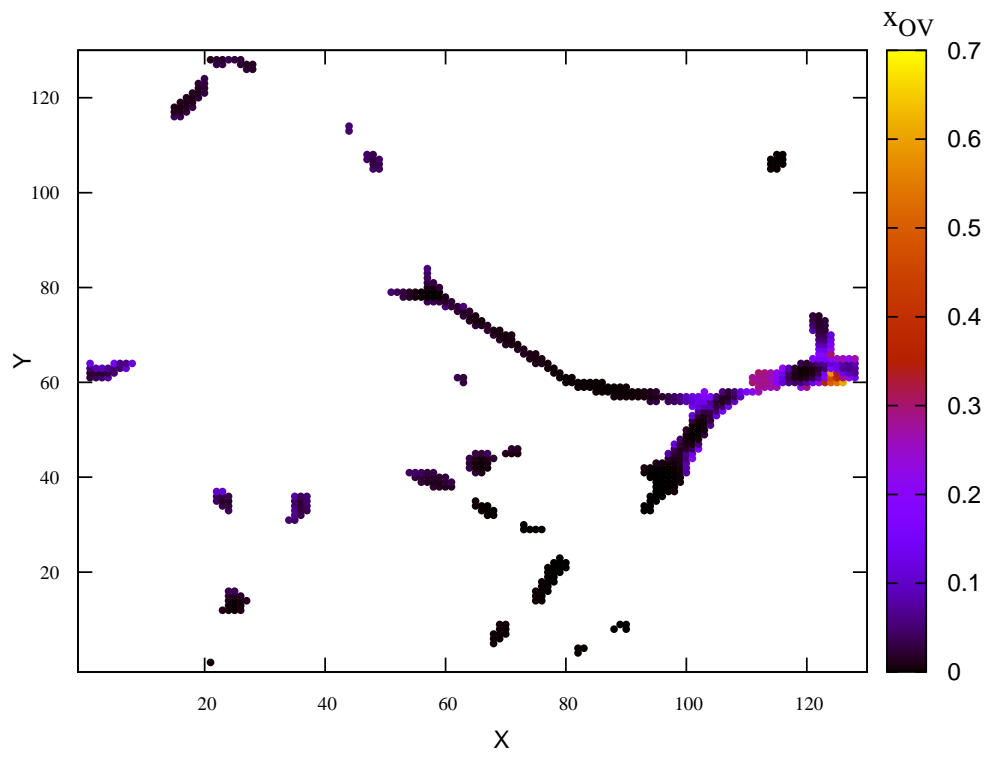


Figure 4.17: Test 3: map of x_{OV} in black to yellow gradient, scale from 0 to 0.7.

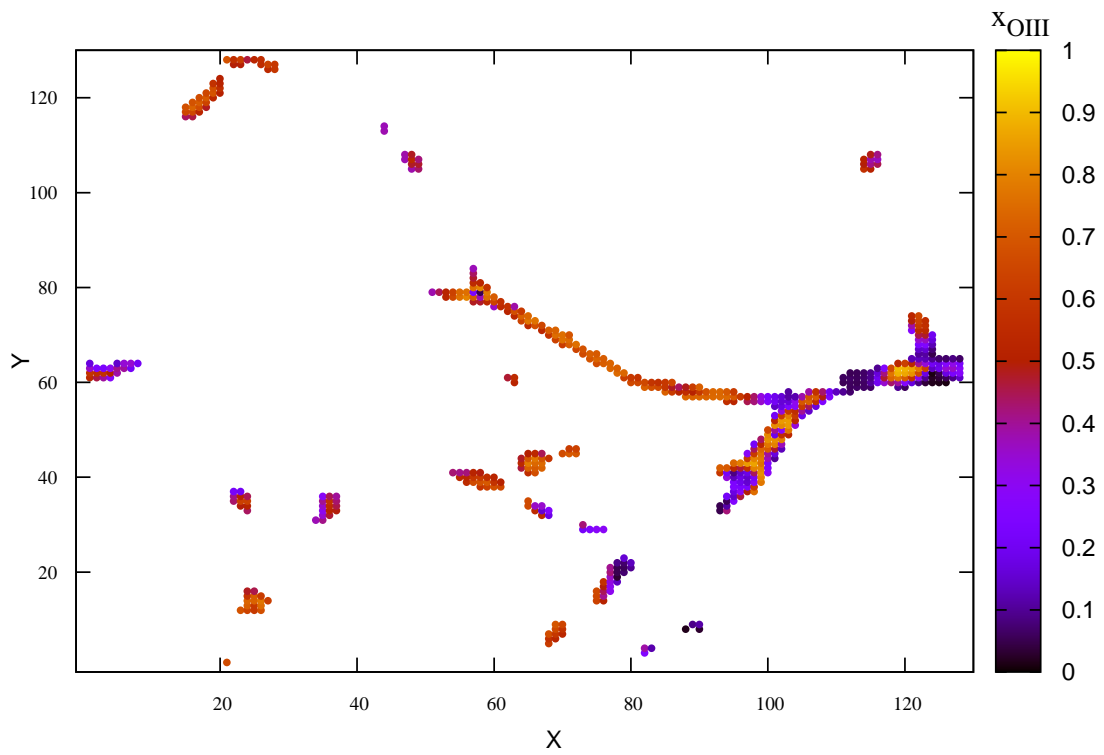


Figure 4.18: Test 3: map of x_{OIII} in black to yellow gradient, scale from 0 to 1.

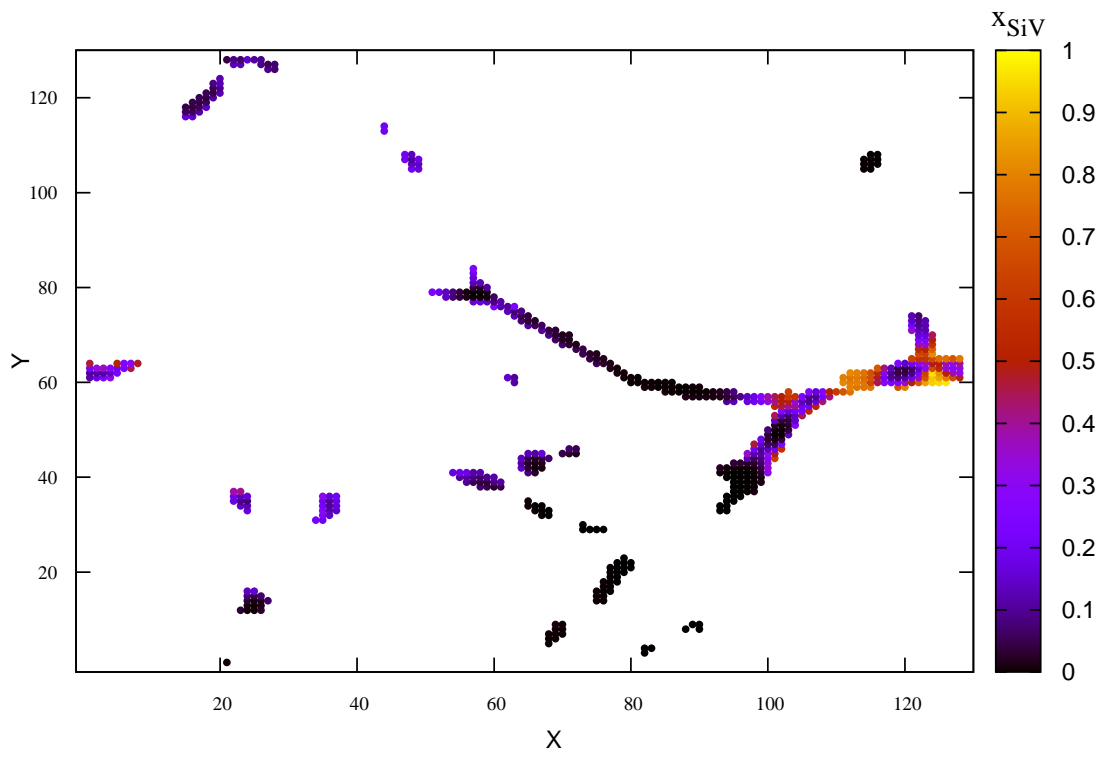


Figure 4.19: Test 3: map of x_{SiV} in black to yellow gradient, scale from 0 to 1.

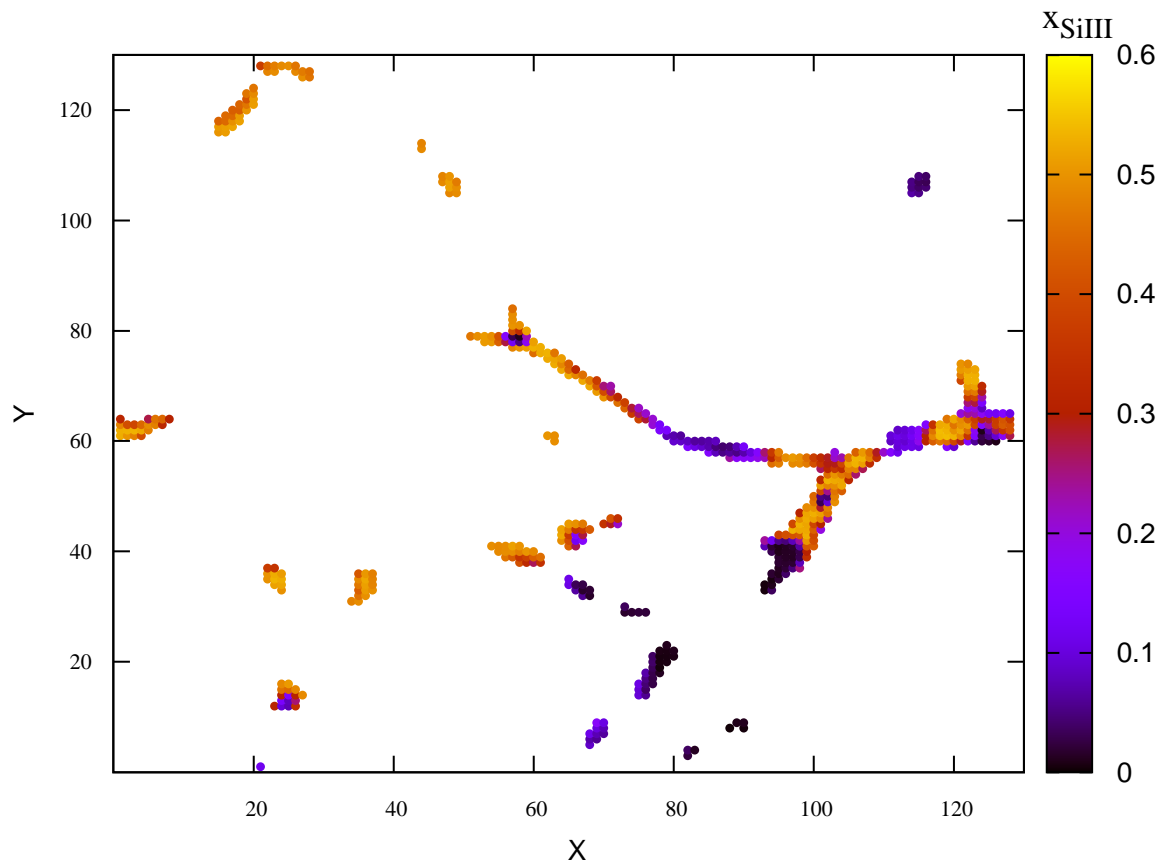


Figure 4.20: Test 3: map of x_{SiIII} in black to yellow gradient, scale from 0 to 0.6.

Chapter 5

UV background fluctuations at $z \sim 3$

In this Chapter I will discuss the possibility of using `CRASH` ([104]) to investigate the fluctuations induced by the radiative transfer on the uniform UV background (UVB), commonly assumed by theoretical models at redshift $z \sim 3$. Independent observations ([167]) suggest that the assumption of the UVB uniformity is not realistic and that the UV background spatially fluctuates. It is then crucial to estimate the effects of such deviations in the UVB shape and intensity.

Theoretical arguments suggest that the UVB variability could be induced by inhomogeneities of the cosmic web or by the variability in the properties of the sources, both spatial and spectral. Quasars at low redshifts have a non negligible variability in their spectral index and are sufficiently rare in space to create a fluctuating UVB.

The physical consequences of a spatially inhomogeneous UVB can be important at many levels; in fact any inhomogeneity in the photo-ionisation rate can alter the ionisation equilibrium regulating the gas of the IGM and consequently the observed properties of the Ly α forest (see 2.1). The correct estimate of the fluctuations in the gas photo-ionisation rates could also help to constrain the role of photo-ionisation versus collisional ionisation in regulating the global ionisation equilibrium on cosmic scales. The cosmological consequences can also be important: changes in the UV background can significantly lengthen the cooling times inhibiting the star formation process or can prevent the formation of low-mass galaxies, as shown by numerical simulations ([73, 43]). The validity of the uniformity hypothesis must then be carefully investigated.

`CRASH` is a suitable choice for constraining the fluctuations of the UV background because it can simulate most of the physical effects expected to cause the UVB spatial variability. It is in fact very accurate in simulating the radiative transfer effects induced by the cosmic web ([158]) and can account for metal ionisation states (see the new code release described in Chapter 4). The inclusion of metal ionisation states can help in particular to constrain the fluctuations of the background shape (see 5.2). The cooling induced by the metal component can also be accounted for, allowing a more reliable estimate of the spatial fluctuations in the IGM temperature.

Finally, the `CRASH` capability to account for different source populations (see 3.3) and their different spectral properties, can be applied to simulate the effects of quasar spectral

variability. A practical application of these features to physically motivated models is part of my future projects and it is not presented in this thesis, where I will just investigate the effects induced by the RT.

The Chapter is organised as follows. In the first Section the problem of the UVB fluctuations at $z \sim 3$ is briefly reviewed in its observational and theoretical aspects (Section 5.1). The problem of the UV background modelling is then addressed in the second Section 5.2. Section 5.3 introduces the new UVB implementation and its tests. An application to a realistic case including a self-consistent treatment of metal spreading is introduced in the last Section.

5.1 The IGM at the epoch of helium Re-ionisation

Nowadays many observations of absorption by the He I and He II Lyman series ([211] and references in 2.1.1) provide independent constraints of the UV background pervading the IGM at low redshifts ($z < 4$). These observations indicate that the He II became fully ionised around $z \sim 2.8$ ([207, 136, 253, 254]), while there are other indirect evidences ([259, 291, 206]) that singly ionised helium started to dominate at $z > 3$ (but also see [28, 27, 16] for conclusions of a more extended He I Re-ionisation epoch).

Theoretical models of helium Re-ionisation ([237, 287, 231, 69, 253]) consider this process as mainly driven by the dominant population of quasars present below $z \sim 4$, in agreement with the peak of the quasar luminosity function predicted at $z \sim 3$ (see [121] and references therein).

Because the He II recombines 5.5 times faster than H I ([77, 187, 71]), to keep helium fully ionised, a sufficient emissivity at the E_{HeII} edge must be provided. Most of the stars we observe lack strong E_{HeII} continua in their spectra, and then QSOs remain the best candidates to drive the process of helium Re-ionisation. A deep understanding of the helium ionisation process can then be used to disentangle the roles of stars and quasars in the history of Re-ionisation ([163, 49] but also see Chapter 2 and 3).

The impact of helium Re-ionisation on the IGM at redshift $z \sim 3$ is also important: the overlapping degree of the ionising bubbles determines in fact the spatial distribution of the He II and He III optical depths (i.e. a variability of the gas transparency), while the rapid ionisation of helium injects substantial heat into the diffuse gas changing significantly its temperature (see for instance [49]). In the following Sections, before discussing the role of UVB fluctuations, I will introduce the modelling of the IGM equation of state (5.1.1) and its optical depths (5.1.2) during the epoch of helium Re-ionisation.

5.1.1 The equation of state of the IGM

Independent observations support the idea of a substantial change in the thermal properties of the IGM near $z = 3$ and then the numerical modelling of the IGM equation of state at this epoch is a central problem in the theory of the Intergalactic Medium.

Bernardi et al. ([20]) detected a spectral feature at $z \approx 3.2$ in the evolution of the Ly α forest, and interpreted the evaluated decrease in the effective optical depth as evidence for He II Re-ionisation. Similarly, a raise in the temperature of the IGM and a change in its equation of state ([123]) to nearly isothermal, was reported by Ricotti et al. ([208]) and Schaye et al. ([226]). The agreement between these results must, however, be considered with some caution because they are based on statistical detections and it is difficult to exclude systematic effects in the measures. Moreover, the data of Ricotti and Schaye have large error bars and the temperature jump they found at $z \sim 3$ is not confirmed by other analyses reporting an isothermal equation of state at the same redshift ([160]).

From the theoretical side, the impact of helium Re-ionisation on the thermal state of the IGM is expected to be particularly relevant in the low density regions of the cosmic web, where heating due to photo-ionisation should dominate over collisional ionisation.

By assuming photo-ionisation equilibrium maintained by a meta-galactic UVB, and by considering a low density gas (in terms of gas over-density $\Delta \equiv \rho/\bar{\rho}$, it is commonly assumed $\Delta \leq (5 - 10)$), it is possible to write the IGM equation of state as a polytropic equation ([123, 269]):

$$T = T_0 \Delta^{\gamma-1}, \quad (5.1)$$

where T_0 is the temperature at the mean density, and γ is the polytropic index. Hui and Gnedin ([123]) assume for instance, $T_0 = 1.5 \cdot 10^4 \text{K}$ and $\gamma = 1.5$, as typical post-hydrogen Re-ionisation conditions.

The polytropic recipe is particularly useful in hydrodynamical simulations and it is based on the recognition that in low density regions the thermal equilibrium is mainly determined through a balance between photo-electric heating and adiabatic cooling losses. Valageas et al. ([269]) argued that this relation is still valid even if the ionising UV background is inhomogeneous, as long as a local ionisation equilibrium can be assumed. Even if this law gives a reasonably good description of the low density IGM, it does not apply to every component of the Intergalactic Medium; in fact the high density regions involved in the gravitational shock-heating processes certainly do not follow it. These regions must instead be modelled as part of the high temperature WHIM, mainly regulated by the physics of collisional ionisation, and then they do not follow the treatment done in this Chapter where the role of photo-ionisation is assumed to be preponderant (see [167] and references therein for an introduction to the WHIM component).

5.1.2 IGM optical depths

If a parcel of gas in the IGM has an optical depth τ , this would induce an absorption in the observed spectrum of e.g. a QSO. The absorption features can be characterised in terms of the mean normalised flux $\langle F \rangle$ and are generally interpreted in terms of τ :

$$\langle F \rangle \equiv \langle e^{-\tau} \rangle. \quad (5.2)$$

It is customary to introduce also the effective optical depth::

$$\tau_{eff} = -\ln \langle e^{-\tau} \rangle. \quad (5.3)$$

Several authors model the evolution of the IGM optical depth during helium Re-ionisation by using a combination of the Fluctuating Gunn-Peterson theory (FGPA) ([276, 275, 160, 30, 284] but also see 2.1.1), and Equation 5.1. These provide an expression for the IGM optical depth τ at $z \gtrsim 2$ as a function of the gas over-density Δ and polytropic index γ as:

$$\tau \simeq 1.0 \left(\frac{1 + \chi_{\text{He}}}{\Gamma_{-12}} \right) \cdot \left(\frac{T_0}{10^4 \text{K}} \right)^{-0.7} \cdot \left(\frac{\Omega_{b,0} h^2}{0.024} \right)^2 \cdot \left(\frac{\Omega_{m,0} h^2}{0.135} \right)^{-0.5} \cdot \left(\frac{1+z}{4} \right)^{4.5} \cdot \Delta^{2-0.7(\gamma-1)}, \quad (5.4)$$

where $\Omega_{b,0}$ and $\Omega_{m,0}$ are the present-day baryon and matter densities (see equations 1.12), h is the reduced present-day Hubble constant (defined in 1.2), and Γ_{-12} is the scaled hydrogen photo-ionisation rate:

$$\Gamma_{-12} = \frac{\Gamma_{\text{HI}}}{10^{-12} \text{s}^{-1}}. \quad (5.5)$$

The term χ_{He} accounts for the extra electrons liberated during He II Re-ionisation and it is commonly assumed: $\chi_{\text{He}} = 1.08$ prior to He II Re-ionisation and $\chi_{\text{He}} = 1.16$ afterwards, for a standard helium fraction by mass of $Y = 0.24$ [183].

The Equation 5.4 can be used to interpret the observed opacity in terms of the physical quantities used to model the IGM. In fact, from the Formula, a decrease in the measured τ_{eff} can be attributed to an increase in the IGM temperature T , either by raising T_0 , by changing γ , or by an increase in the photo-ionisation rate (a combination of them is certainly more realistic).

In general, an increase in the free electron fraction can raise the opacity by reducing the recombination timescale. Both an increase in T and a change of about 8 percent in the fraction of the free electrons, can then be interpreted as a signature that He II Re-ionisation occurs ([30, 284]).

5.1.3 The column density ratio η and the fluctuations of the IGM

A directly measurable quantity in the Ly α forest is the H I to He II column density ratio, defined as:

$$\eta \equiv \frac{N_{\text{HeII}}}{N_{\text{HI}}}. \quad (5.6)$$

Since the first measurements of the quasar Q0302-003 at $z = 3.286$ ([127, 66, 120, 114]) and the quasar HE 2347-4342 at $z = 2.885$ ([207, 234, 180]) it has been shown that the He II opacity is ‘‘patchy’’ and that η decreases gradually from higher to lower redshift, possibly due to a change in the slope of the ionising spectrum ([294]). Shull et al. ([231, 232]) discussed the small scale variations of η and found an apparent correlation between high η (less ionised He II) and low H I column density. They ascribed these variations to ‘‘local ionisation effects’’ in the proximity of the quasars.

Independent spectroscopic observations taken by FUSE, the Keck Telescope, and the Very Large Telescope (VLT) report variations of $\eta \in [20 - 200]$ over [2–10] Mpc scales implying significant spatial fluctuations in the radiation field at the ionisation edges of H I and He II ([109, 110, 149, 230, 77, 81]).

The theoretical importance of the η parameter was firstly realised by Miralda-Escudé ([171]). Linking η with the He II to H I optical depth ratio in the low density and highly ionised IGM, i.e. $\eta \propto \tau_{\text{HeII}}/\tau_{\text{HI}}$, it is possible to show that η depends only on the shape of the ionising background. This means that the observed measures of η are a useful tool to probe the spectrum of the UVB.

Miralda-Escudé ([171]) has proved that the ratio $\tau_{\text{HeII}}/\tau_{\text{HI}}$ depends only from the spectral shape. A simple derivation is reported below.

For a uniform IGM, the Gunn-Peterson optical depth can be written as in Equation 2.1. It can be shown that (for a full derivation refer to [171]):

$$\frac{\tau_{\text{HeII}}}{\tau_{\text{HI}}} = \frac{1}{4} \frac{n_{\text{HeII}}}{n_{\text{HI}}}, \quad (5.7)$$

where n_{HeII} and n_{HI} are number densities of H I and He II at fixed redshift. If the abundances of H I and He II are in equilibrium with an ionising background of intensity $J(\nu)$ at fixed redshift, and the region under consideration is photo-ionisation dominated and optically thin:

$$\frac{n_{\text{HeII}}}{n_{\text{HI}}} = \frac{n_{\text{He}}}{n_{\text{H}}} \frac{\alpha_{\text{HeII}}}{\alpha_{\text{HI}}} \frac{\bar{\sigma}_{\text{HI}}}{\bar{\sigma}_{\text{HeII}}} \frac{J_{\text{HI}}}{J_{\text{HeII}}} \propto \frac{J_{\text{HI}}}{J_{\text{HeII}}}, \quad (5.8)$$

where α_{HI} and α_{HeII} are recombination coefficients of H I and He II and their ratio is very weakly dependent on the temperature T of the gas. We generally assume $\frac{\alpha_{\text{HeII}}}{\alpha_{\text{HI}}} = 5.5$. $\bar{\sigma}_{\text{HI}}$ and $\bar{\sigma}_{\text{HeII}}$ are the integrated cross sections of H I and He II, with $\frac{\bar{\sigma}_{\text{HI}}}{\bar{\sigma}_{\text{HeII}}} = 4$. Finally, J_{HI} and J_{HeII} is the intensity of the UVB calculated at the same frequencies.

To connect η with the optical depth ratio more assumptions are needed. By considering the contribution of hydrogen and helium and separate expression for τ_{HI} and τ_{HeII} provided by the FGPA ([276, 284]) and by assuming that H I and He II are tracing the same cosmic densities, it is possible to obtain an approximated He II optical depth, as function of η and τ_{HI} .

It is possible to write (see the derivation in the original papers):

$$\frac{\tau_{\text{HeII}}}{\tau_{\text{HI}}} \simeq \frac{\eta}{4} \simeq 0.112 \frac{\Gamma_{\text{HI}}}{\Gamma_{\text{HeII}}}, \quad (5.9)$$

and then:

$$\eta \propto \frac{\Gamma_{\text{HI}}}{\Gamma_{\text{HeII}}}. \quad (5.10)$$

Equation 5.10 shows that any fluctuation in the photo-ionisation rates of neutral hydrogen and singly ionised helium can be traced as scatter in η .

Fluctuations in the UV background can be induced by different effects: source clustering, variance in the spatial distribution of the sources and in their intrinsic properties, as well as the contribution of radiative transfer effects through the cosmic web ([295, 296, 78, 166, 57]). If these fluctuations are proven to be large, the common assumption of a spatially uniform UV background after Re-ionisation can be invalidated.

The effects mentioned before certainly impact both the hydrogen and helium component but it is important to discriminate between the hydrogen ionising photons and the helium ones.

For hydrogen Re-ionisation, mainly sustained by the contribution of the galaxies ([54, 52, 49]), it is possible to safely assume (if the RT effects are not considered) a spatially uniform UV background at redshift $z \sim 3$. At this epoch in fact, the galaxies result quite uniformly distributed over the simulated volume and the mean free path of the hydrogen ionising photons is larger than the mean distance of the sources. Madau et al. and Faucher-Giguère et al. ([150, 79]) estimated that the amplitude of these fluctuations induced by the sources is limited to some percent.

Fluctuations in the helium-ionising background have been less investigated (though see [77, 158, 29] and references in [167]) but simple theoretical considerations are sufficient to expect them to be larger.

At the helium resonant frequencies in fact, the absorption is stronger and then we can expect shorter attenuation lengths. Furthermore, because helium Re-ionisation is thought to be mainly driven by quasars after $z \sim 4$, it is necessary to consider that these sources have finite lifetimes, are quite rare and spatially inhomogeneous and they present a broad distribution in spectral indexes ([255, 231]). The combination of these properties can induce variability in the UV background on the typical scales of the IGM (consider for instance that the QSO mean separation is about 100 comoving Mpc at $z \sim 3$).

Although many authors tried to estimate the relative contribution to the UVB fluctuations of each of the effects mentioned above ([167, 158, 29]), the adopted methods suffer large uncertainties in the prediction of the amplitude and of the spatial scales of these fluctuations.

Recently, Furlanetto and collaborators ([90, 91, 92]) confirmed the presence of deviations on large physical scales. They found that large fluctuations are induced mainly by the source distribution at $z \sim 2 - 3$, in agreement with previous results of Meiksin [167].

The main limitations of these studies, mostly based on semi-analytic approximations, reside in their difficulty to account for radiative transfer effects. On the small scales of the cosmic web, where the density field gradients are more steep, the RT could play a relevant role and should not be discarded.

Full radiative transfer simulations are then necessary to constrain the epoch of helium Re-ionisation and to model the impact of an inhomogeneous He III evolution on the Ly α forest opacity ([158, 165, 162, 161]). Radiative transfer effects (like shadowing, filtering and self-shielding) obviously modify the intensity and the shape of the UV background prior and during He II Re-ionisation and must be included in the simulations, but the development cost of such cosmological RT codes is very high and their current implementations still suffer a lack of flexibility in modelling variability of source properties (see Chapter 3).

Studies based on the results of full helium Re-ionisation simulations are then less common in the scientific literature (but see McQuinn [162] and references therein for a recent treatment). In particular, Bolton et al. ([29]) found that assuming $\eta \approx 60$ it is possible to reproduce the observed optical depth in the helium Ly α forest, when a fluctuating radiation field is accounted for.

To summarise the fluctuations predicted by theoretical models, we can consider a column-density ratio oscillating in the range $\eta \in [40 - 100]$ ([172, 77]).

5.2 Modelling the shape of the cosmic UV background

The problem of modelling the shape and the intensity of the UVB, without tracing the entire history of the Re-ionisation, plays a central role in the theory of the IGM. An accurate model of the UVB is in fact necessary to estimate the intergalactic metallicity, temperature and opacity from observations ([223, 6, 4] but see also 2.1 in this thesis).

The strongest evidence of the existence of this background comes from the quasar ‘proximity effect’, i.e. the observed tendency of the clouds in the Ly α forest to be statistically under-abundant in the immediate vicinity of quasars ([204]). While the UVB intensity (I_{UVB}) is indirectly estimated by the ‘proximity effect’, and its evolution in redshift (mainly below $z \sim 4$) can be determined from the evolution of the QSO luminosity function ([190, 121]), the shape of the background is observationally inaccessible and must be modelled at each redshift by using assumptions on the physical properties of the sources and the physical state of the IGM.

Theoretical models generally use the metal ions observed in the IGM (see 2.6). By considering the various ions of C, O and Si up to O VII we have in fact a remarkable number of ionisation potentials well distributed across the resonant edges of the main absorbers: H I, He I and He II. As an example, consider the case of C IV and Si IV (see Figure 4.2). The ratio $N_{\text{CIV}}/N_{\text{SiIV}}$ is sensitive to the shape of the UVB on either side of the He II ionisation edge ([241, 212, 99]), and has the additional advantage of being less susceptible to the fluctuations of the IGM density field ([93, 283, 285]). It is instead sensitive to fluctuations in the relative abundance of carbon and silicon, if these metals do not follow the solar composition ratios.

These ions are particularly important because they also have an observational counterpart, although controversial. Songaila & Cowie ([240]) and Songaila ([238]) reported the observation of an abrupt change in the column density ratio $N_{\text{CIV}}/N_{\text{SiIV}}$ around $z = 3$, and argued for a sudden hardening of the UVB at that epoch. This result is also in agreement with the effects of the helium Re-ionisation and it is consistent with the idea that the gas in the IGM becomes optically thin to the He II ionising photons. Unfortunately, such observations are controversial: while Agafonova et al. ([3] but also see [212, 99]) extensively found an evolution in metal ratios ([2, 3, 141]), other independent measurements ([132, 6, 26]) did not report any significant change in these column ratios. At present, the observations of the He II forest, and the ratios in metal lines at $z \sim 3$, are too scarce to draw definitive conclusions on the epoch of helium Re-ionisation, especially if the process is highly inhomogeneous.

Theoretical models of the UVB evolution in redshift, based on the number, distribution, and spectral properties of the underlying sources (like AGNs and starburst galaxies) have been computed by Miralda-Escudé & Ostriker ([173]), Haardt & Madau ([109, 110, 111]), Fardal et al. ([77]), Bianchi et al. ([25]) and Faucher-Giguère ([80]), taking into account

the filtering effects due to the hydrogen and helium Ly α forests. In these models, the shape of the ionising spectrum depends on the relative mix between “hard” (AGNs) and “soft” (stellar) sources and on the details of the radiative transfer through the IGM ([227, 207, 292, 293][15, 228, 173, 164, 98, 109]), often computed on a simplified 1D geometry.

Recently Bolton and Viel ([31]) have tried to simulate the $N_{\text{CIV}}/N_{\text{SiIV}}$ fluctuations by using a series of simplified UVB models reproducing most of the relevant aspects of the spatially inhomogeneous UVB expected towards the tail-end of He II Re-ionisation ([77, 29, 168]). These models have been combined with a large hydrodynamical simulation and the metallicity of the IGM has been reproduced by assuming that it traces the simulated gas over-density ([223, 6]). Finally, they have calculated the ratios $\tau_{\text{HeII}}/\tau_{\text{HI}}$ and $\tau_{\text{CIV}}/\tau_{\text{SiIV}}$, at redshift $z \sim 3$, resulting from each model. By comparing these results they have found fluctuations in the ratio of $\tau_{\text{HeII}}/\tau_{\text{HI}}$ largely attributable to spatial variations in the He II ionising background. Quasars in the simulated volume can then be responsible of these variations. Unfortunately, the authors were not able to report a counterpart in the ratio $\tau_{\text{CIV}}/\tau_{\text{SiIV}}$, which did not show any relevant sensitivity to the models. In any case, this lack of metal fluctuations does not provide a stringent limit on the non-uniformity of the UVB spectral shape, and does not preclude the possibility of He II Re-ionisation completing around $z \sim [2 - 3]$.

As already discussed in Chapter 4, metals have been included in CRASH with the main limitation that they do not contribute to the optical depth of the gas. At metallicities typical of the IGM, this is quite appropriate as I have proved in the test Section 4.4 of the same Chapter. For those ions with ionisation potentials nearby E_{HeII} , these approximations are even more appropriate because the absorption is certainly dominated by He II. In the following Sections we then use the new release of CRASH to numerically simulate the fluctuations of the parameter η and to obtain the ratio $\tau_{\text{CIV}}/\tau_{\text{SiIV}}$.

5.3 UV background in CRASH

The first physical application of the background algorithm implemented in CRASH ([159]) has been published by Maselli and Ferrara in 2005 ([158]). The authors applied CRASH to study the effects of the RT on the Ly α forest on small scales (they used a simulation box of $10h^{-1}$ Mpc comoving), finding that spatial fluctuations in η and in the gas temperature are induced by the radiative transfer. To ensure that these fluctuations are not dominated by the numerical noise of the Monte Carlo method (see 3.2) the authors changed the original background implementation ([159]) allowing all the cells, but those associated with over-densities $\Delta > \Delta_e$, to emit photons¹.

The successive improvements introduced in CRASH2 (i.e. the adoption of photon packets and an improved algorithm for the temperature calculation, see [157]) have sensitively reduced the algorithm performances and the original background sampling recipe adopted by Maselli and Ferrara has been extensively re-considered during my PhD project (see 3.3).

¹(The value of the threshold $\Delta_e = 60$, necessary to preserve the effect of self-shielding in high-density regions and galactic haloes, is motivated in [158])

Although many performance problems will be substantially alleviated when pCRASH ([188]) and CRASH will converge in a further code release, it is very important to implement an efficient background algorithm in itself.

As already introduced in Section 3.3.2, the global re-engineering of the new CRASH helps in solving some performance issues linked to the multi-frequency packets and the temperature algorithm, allowing the execution of large Re-ionisation simulations with many point sources ($N_s > 4 \cdot 10^4$) within a reasonable CPU time ([49]); these improvements however, can not help when we want to simulate a uniform UV background by using an MC code.

In the old CRASH a typical simulation of the UVB has to handle a global number of photon packets $N_{pc} \sim 10^9$ crossing the box to minimise the random noise of the MC sampling. This is a critical order of magnitude which could impede the run to terminate in a reasonable time. To ensure the spatial uniformity of the UVB with a lower computational cost, in the new CRASH I have imposed the condition that the photon packets are emitted from the cells of a regular sub-grid of the computational domain (see 5.3.1).

Before discussing the implementation details, I want to point out that when the metal component is included in the calculation, the spatial uniformity requirement is even more stringent. In fact, unlike hydrogen and helium, which are assumed to be present in every cell of the volume, metals are confined into an irregular sub-domain, roughly tracing the gas over-densities (see 4.3.1 or Figures in Test 3). A coarse spatial sampling of this irregular sub-domain, could produce unphysical fluctuations in the metal ions, because of their high sensitivity to the ionising field (see Test 2 4.4.2).

In the following Sections I will provide more technical details of the background implementation and one of the test I have performed to prove its reliability.

5.3.1 Numerical scheme of the CRASH UVB

The new UV background implementation uses the same domain masking technique described in Section 4.3.1 to define a regular sub-grid U , whose nodes (or points) are allowed to emit photon packets. These 'emission points' are identical in their ionisation rates, established by the calibration technique introduced in [158]. They also propagate packets with identical UVB spectral shape (e.g. the HM96 shape [109]) as established by the general CRASH algorithm (see 3.3.1). Each emitter is then responsible for sampling its solid angle by using a number of packets specified during the simulation initialization (see 3.3.1). A more formalised description of the masking technique can be found in Section 4.3.1.

In practice, U is implemented as boolean mask loaded at the CRASH_SIMULATION initialization, as additional CRASH IC. U is then processed by the CRASH_SIMULATION, which internally morphs it into a linear array of EMITTER_POINTS types and then starts the usual RT work-flow (3.3.1).

The mask U can eventually be pre-processed cross-correlating it with the over-density map, to exclude the grid points in which the condition $\Delta > \Delta_e$ holds.

Once emitted from a node, the packets cross the cells of the domain and deposit their energy as established by the standard CRASH algorithm in Section 3.3.1. Periodic boundary

conditions are generally enabled in UVB simulations to enforce a good sampling on the six faces of the simulated box (as already detailed in [159, 158]).

This strategy ensures that every region of the domain has the same sampling by design, within the intrinsic accuracy of the MC scheme. It also allows a great flexibility because the resolution of the mask U can be chosen as a sub-multiplier of the $(N_c - 1)^3$ nodes in the CRASH grid and a high resolution of U (e.g. 32^3) can be balanced by an appropriate decrease of the sampling packets in use, maintaining the MC convergence. The best combination of nodes versus packets, must be obtained by numerical experiments as done in the uniformity test in Section 5.3.2.

Additional randomness can be easily added in the algorithm without relevant drawbacks on the execution performances: the linear array of `EMITTER_POINTS` could be easily shuffled after each packet cycle, for instance. One of the tests I have performed is illustrated in the next Section.

5.3.2 Spatial uniformity test

In this Section I show the ability of the new UVB model in maintaining a good spatial sampling with reduced computational requirements.

I have simulated a UV background in a box of side length $L_b = 10.0h^{-1}\text{Mpc}$ comoving, filled with a pristine gas mixture of H and He (their respective fractions are 0.9 and 0.1). The gas is assumed to be initially neutral and with constant number density of $n_{gas} = 1.0 \cdot 10^{-5} \text{cm}^{-3}$ and temperature $T_0 = 100 \text{K}$. The simulation is set up with a duration of $t_f = 7 \cdot 10^6 \text{yrs}$ as in [158]. A standard grid resolution of $N_c^3 = 128^3$ cells is adopted and it is masked in three runs with three U grids of 16^3 (U_{16}), 32^3 (U_{32}) and 64^3 (U_{64}) emitting cells respectively.

The spectrum selected for this test is the first Haardt and Madau cosmic UV background model ([109], hereafter HM96) used also in [158]. The global emissivity in the cube is maintained constant in the three runs, after calibrating the field with the values provided in HM96. I have adopted the same calibration algorithm illustrated in [158]; a brief summary of the calibration technique is provided in the following Paragraph.

The problem of calibrating the intensity of the simulated UVB raises when the assigned emissivity of the UVB must be related to the photon content of each emitted packet: it is in fact not obvious how to convert the assigned flux J_ν [$\text{erg s}^{-1} \text{cm}^{-2} \text{Hz}^{-1} \text{sr}^{-1}$] in photons per frequency ν of the sampling packets. In the formalism of the Maselli and Ferrara, the number of monochromatic photons in a packet (N_γ), as function of the simulation parameters, can be written as:

$$N_\gamma = A \frac{N_c^2 t_f}{N_p N_{cyc}} \frac{J_\nu}{J_{912}}, \quad (5.11)$$

where A [s^{-1}] is the calibration factor and J_{912} indicates the UV background flux at the ionisation edge for hydrogen. In the HM96 $J_{912} \sim 0.4 \cdot 10^{-21} \text{erg cm}^{-2} \text{s}^{-1} \text{Hz}^{-1}$ is assumed at redshift $z \sim 3$.

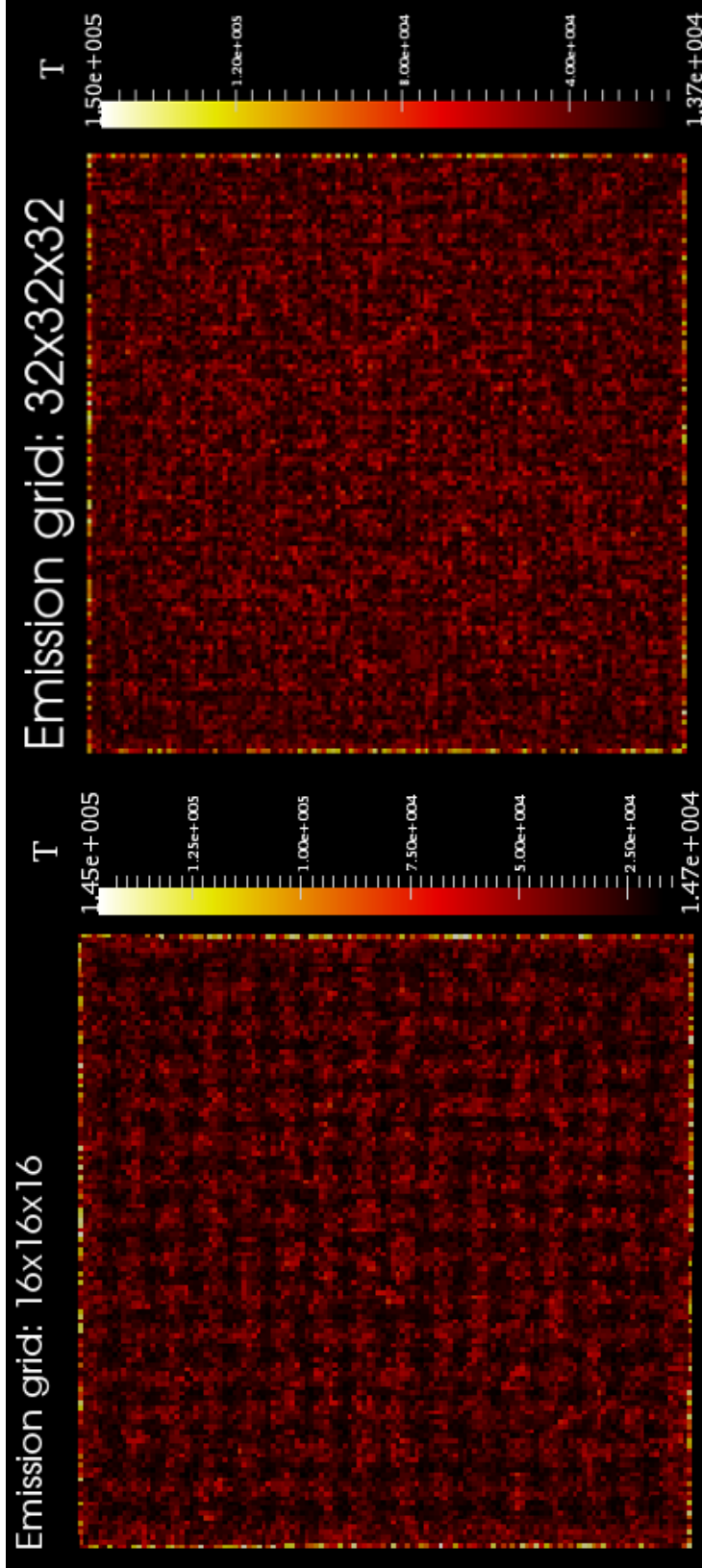


Figure 5.1: **Left panel:** temperature field (red-to-yellow gradient) simulated by the CRASH background algorithm on a volume slice of $L_b = 10h^{-1}\text{Mpc}$ with domain resolution of $N_c = 128$ cells per box side. The slice is placed at the center of the cube and perpendicular to the z axis. The image refers to a simulation configuration using the HM96 ([109]) spectrum and an emitter mask of 16^3 nodes, after emitting $N_p \sim 5.3 \cdot 10^6$ packets. **Right panel:** temperature field (red-to-yellow gradient) simulated by the CRASH background algorithm on a volume slice of $L_b = 10h^{-1}\text{Mpc}$ with domain resolution of $N_c = 128$ cells per box side. The slice is placed at the center of the cube and perpendicular to the z axis. The image refers to a simulation configuration using the HM96 ([109]) spectrum and an emitter mask of 32^3 nodes, after emitting $N_p \sim 5.3 \cdot 10^6$ packets.

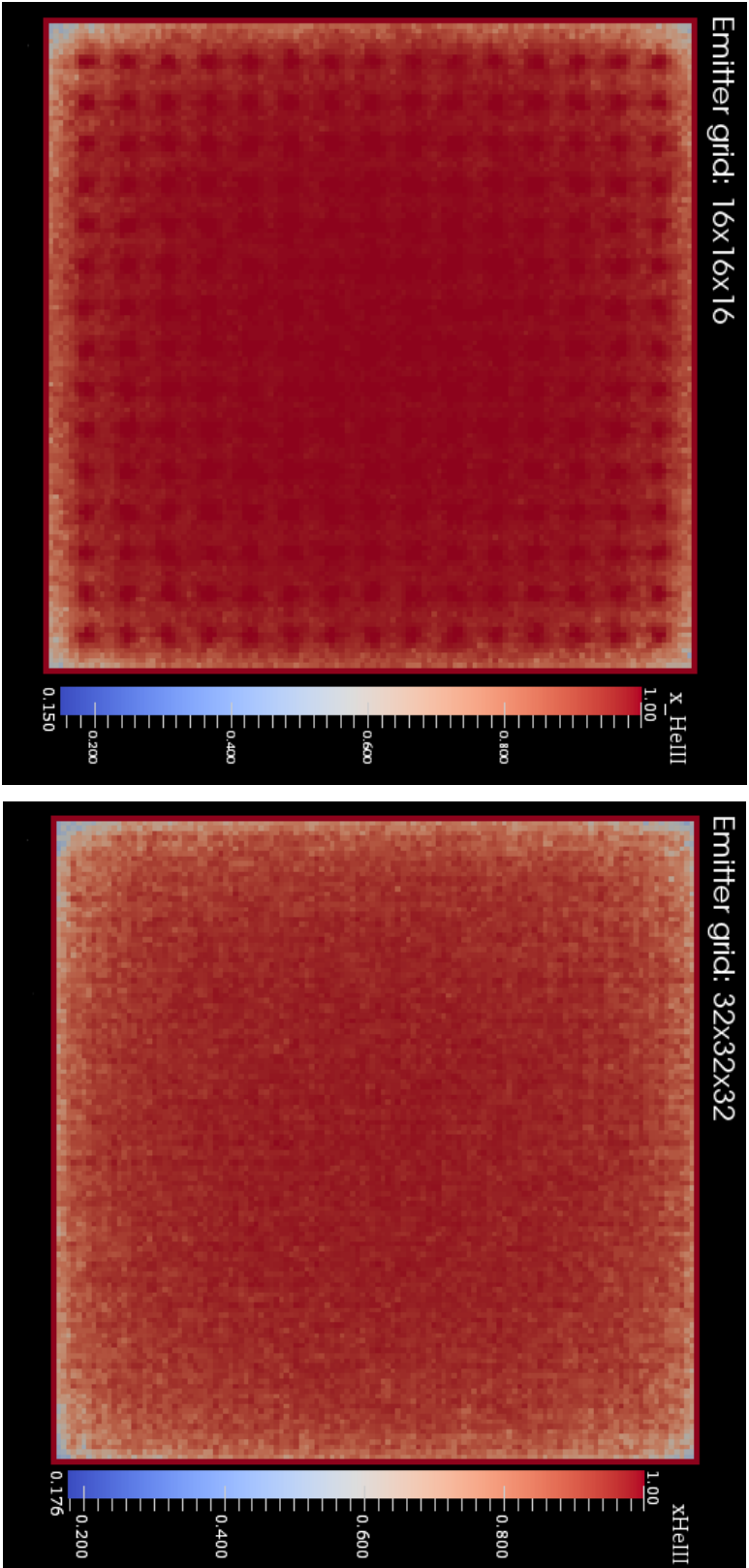


Figure 5.2: **Left panel:** ionisation fraction of He III (bue-to-red gradient) simulated by the CRASH background algorithm on a volume slice of $L_b = 10h^{-1}\text{Mpc}$ with domain resolution of $N_c = 128$ cells per box side. The slice is placed at the center of the cube and perpendicular to the z axis. The image refers to a simulation configuration using the HM96 ([109]) spectrum and an emitter mask of 16^3 nodes, after emitting $N_p \sim 5.3 \cdot 10^6$ packets. **Right panel:** ionisation fraction of He III (bue-to-red gradient) simulated by the CRASH background algorithm on a volume slice of $L_b = 10h^{-1}\text{Mpc}$ with domain resolution of $N_c = 128$ cells per box side. The slice is placed at the center of the cube and perpendicular to the z axis. The image refers to a simulation configuration using the HM96 ([109]) spectrum and an emitter mask of 32^3 nodes, after emitting $N_p \sim 5.3 \cdot 10^6$ packets.

Once the intensity and the spectral shape of the background have been provided by the model, the factor A is the same for any combination of numerical parameters and can be inferred analytically in the optically thin case when the gas is composed only by hydrogen (see the original paper for a derivation). When helium is present in the gas, a numerical calibration is required, as described in the following Paragraph.

As suggested by the authors, I have performed a simulation on a box empty in all the cells but the central one in which I have assigned the values $n_{gas}, T = 10^4\text{K}$ as representative of the ionisation equilibrium imposed by the HM96 model. The cell is chosen at the center of the box to ensure a uniform illumination in each cell face and to maximise the sampling of the radiation field created inside its volume. The number density of the cell used for the calibration is simply n_{gas} because the box selected for this test is uniform, and T is the reference value for the photo-ionisation of a gas compatible with the equilibrium assumptions of the HM96 model.

During the calibration run, CRASH counts all the photons absorbed in the cell and derives the average hydrogen ionisation rate Γ_{HI} in the central cell. This is done first by collecting the absorbed photons per spectrum frequency and per species, and after by solving the integrals in Formula 3.2. Once the photo-ionisation rate is known per each species, A is obtained as the best calibration parameter reproducing the value of Γ_{HI} and x_{HI} , indicated in HM96 as $\Gamma_{\text{HI}} = 1.2 \cdot 10^{-12}\text{s}^{-1}$, i.e. calibrating the photo-ionisation equilibrium of the hydrogen. I found a calibration value of $A = 1.48 \cdot 10^{-52}\text{s}^{-1}$; this value is compatible with the value obtained in [158] with a similar simulation set-up but the old model in use.

I now proceed to show the results of this test. Because the RT is performed on a uniform medium, once the box is in equilibrium with the UVB after a time t_{eq} , I expect to see a low spatial scatter in the values of the tracked UV intensity and also in the gas ionisation fractions and temperature.

The time t_{eq} is determined comparing the volume averaged values of all the physical quantities (i.e. ionisation fractions and temperature) and selecting t_{eq} after which the values in the successive output differ by 10^{-5} .

As expected, I found the quality of the spatial sampling is increased with higher resolutions of the mask U but the large number of emitters in the run U_{64} results in a prohibitive slowdown of the code performances. This is due to a combination of factors. First, the number of emitters is increased and then the loop over the array of `EMITTER_POINTS` requires more CPU time. Second, the number of emitters near the faces of the cube is higher and the number of packets immediately escaping the box (i.e. with large energy content) is significant. With the adoption of periodic boundary conditions and $N_{cyc} = 10$ (see [158]), each packets re-entering the box, performs a large number of cell-crossings and then the code rapidly slows down in its performances.

Finally, because the HM96 background is very efficient in rapidly ionising the box with the assumed n_{gas} , the increased transparency of the medium implies that more CPU time is needed to complete a simulation.

After a series of numerical experiments balancing N_p and the resolution of the grid U , I found that a combination of 32^3 emission nodes and a number of $N_p = 179$ packets per node is sufficient to create an equilibrium configuration within $t_{eq} = 10^3\text{yrs}$. This is also

consistent with similar numerical experiments performed by Maselli and Ferrara.

The differences in the new model reside in the quality of the obtained spatial resolution as visually illustrated by a slice of the temperature map in Figure 5.1, taken at the equilibrium time. The left and right panels of this Figure refer to the simulation set-up reported above but with different resolutions of the mask U . The left panel refers to the case U_{16} and reports the temperature field (red-to-yellow gradient) after a total emission of $5.3 \cdot 10^6$ packets. The right panel instead reports the case with U_{32} nodes after the emission of the same number of total packets.

The field in the right panel results visually more homogeneous with less regular patterns thanks to the increased number of equispaced emitters in the volume. The simulated UVB creates then a more uniform temperature background on a constant gas configuration, as expected. The finer grid in fact allows more cell-crossings for each packet and the bubbles created around each emitter overlap faster, reducing the spatial inhomogeneities.

The situation is better illustrated in Figure 5.2 reporting the ionisation fraction of He III on the same slice. From the tests performed on various Strömgren spheres (see Chapter 4), I know that the patterns of the He III bubbles are sharper than the temperature ones; this is clearly shown in the left panel. The right panel instead appears remarkably regular, but on the box borders where the background is still not well established. Note however that the same trend is uniformly present in all the box sides, showing a high degree of symmetry of the generated background field. To solve the problem at the borders, more N_p emissions are needed, as confirmed by the successive ionised snapshots. On the other hand, because the problematic cells are regularly confined to the borders of the simulated box, in many applications they could be easily rejected from the data, before doing a statistical analysis.

As final remark I want to point out that this test can be used also to constraint the average MC noise affecting any realistic simulation involving a cosmic web. After selecting an appropriate size for U and a value of N_p which guarantees the MC convergence, it is possible to run a simulation with a constant number density equal to the mean gas number density of the cosmic web and to provide an average estimate of the MC noise in the uniform case. This estimate can then be subtracted to the fluctuations found in the real simulation once the best grid resolution has been established.

A realistic application of this technique is provided in the following Sections.

5.4 Simulation of UV background fluctuations at $z \sim 3$

This Section introduces the first cosmological application I am currently running. The set-up of a realistic case requires a gas density snapshot at redshift $z \sim 3$ taken from an hydrodynamical simulation of galaxy formation, accounting for metal production and spreading (see 2.2). As explained in [158], the fluctuations induced by the radiative transfer are believed to be efficient on a scale of about $10h^{-1}\text{Mpc}$ comoving, where the effects of the variability in the source properties (especially the quasars) should be minimised because they act on the typical source correlation scale of $100h^{-1}\text{Mpc}$. For this reason I decided to adopt the same simulation scale of Maselli and Ferrara ([158]) but changing the gas density

snapshot and using one of the runs performed at MPA by U. Maio ([151]). The simulation set-up is briefly introduced in the following Section.

5.4.1 Galaxy formation simulation

The simulation run described in this Section is referred as 'Zcrit4-10th7' in Maio et al. 2010 ([151]); the run has been performed by using a modified version of the GADGET-2 code ([243]) in the frame of the standard CDM cosmological model (see 1.2).

The following cosmological parameters (see Chapter 1) have been adopted: $H_0 = 70 \text{Kms}^{-1} \text{Mpc}^{-1}$, $\Omega_{m,0} = 0.3$, $\Omega_{b,0} = 0.04$, $\Omega_{\Lambda,0} = 0.7$, $\Omega_{tot,0} = 1.0$, $\sigma_8 = 0.9$. The simulation starts from a neutral gas configuration at $z = 100$ and zero metallicity, and evolves 320^3 particles per gas and dark matter species, having masses of 116 and $755 M_{\odot} h^{-1}$, respectively.

A rich set of physical processes is accounted for in the simulation: primordial molecular evolution ([153]), star formation prescriptions ([152]), and metal pollution from stars ([263]). The code is able to simulate the whole set of chemistry reactions leading to molecule creation or destruction and metal pollution, with the corresponding cooling functions (fine structure metal transition cooling are included for O, C⁺, Si⁺, Fe⁺ at $T < 10^4 \text{K}$) and to follow the abundances of the H-, He- and Deuterium-based chemistry ([288, 153]). The scheme adopted to simulate the metals spreading is described in [263] and it is able to account for an arbitrary number of metals. In the simulation under consideration the most abundant metals produced during stellar evolution (C, O, Mg, S, Si and Fe) are accounted for. The simulation starts with zero metallicity.

The IMF is chosen according to the metallicity of the stellar particles (Z) and a transition from PopIII stars to metal-enriched POPII, is assumed to take place, whenever the gas reaches a critical metallicity $Z_{crit} = 10^{-4} Z_{\odot}$. Below Z_{crit} the authors assume a Salpeter IMF in the mass range $[100, 500 M_{\odot}]$, while for higher metallicities, a Salpeter IMF in the mass range $[0.1, 100 M_{\odot}]$ is taken.

The metal production is accounted for following star formation and evolution: stars evolve and die according to their characteristic lifetimes and expel newly created metals into the surrounding gas; changes in gas cooling properties either at low ([153]) and at high temperatures ([251, 280]) are simulated self-consistently. Metals are produced by AGB stars and supernovae [SNII, SNIa]: star forming SPH-particles produce metals which are smoothed over the neighbours according to the SPH kernel; the relevant mass range for metal pollution is approximately $[140, 260 M_{\odot}]$, because of the formation of PISN (see 2.2.1).

Metal spreading is simulated by mechanical feedback from supernovae and galactic winds; winds are simulated within the kinetic feedback scheme (see 2.2.2) with velocities of 500Kms^{-1} .

Finally, a cosmic UV background (HM96) is included as photo-ionisation mechanism affecting the gas cooling function and the resulting structure formation.

5.4.2 Radiative transfer simulation set-up

For the radiative transfer simulation I have selected the last version of the code `CRASH` which includes the new UV background model (Section 5.3) and the pipeline capabilities described in Chapter 4.

The initial conditions for the RT simulation including metals (see Section 4.3) have been prepared by selecting an output at redshift $z = 3$ of the hydrodynamical simulation described in the previous Section.

First, the number density maps for the gas and the metal component (C, O, Si) have been created mapping the SPH-particles distribution on a uniform grid of $N_c^3 = 128$ cells. This can be done by using the code `GadgetToGrid` (see [202]) developed to map particle distribution into gas distribution on a uniform grid of assigned cell resolution N_c .

To generate the metallicity maps I have made a simple extension to `GadgetToGrid`, which accounts for the metal mass contained in each SPH gas particle and selects only C, O, Si. The mass of each element has then been mapped following the same gridding algorithm of the original code.

Once the maps are ready, the initial conditions for the RT set-up must be chosen.

Following the results of the UVB uniformity tests (see Section 5.3.2), I selected a uniform grid U_{32} , from which I have removed over-dense points following the prescription $\Delta_e > 60$, to preserve the self-shielding occurring in over-dense regions. The old UV background model (HM96) has been selected for a first set of runs, in order to be consistent with the hydro simulation set-up. I have then performed the same calibration strategy described in the uniformity test (see 5.3.2), obtaining a similar calibration factor $A = 1,52 \cdot 10^{52} \text{s}^{-1}$; this is justified by the similar averaged properties of the new simulation, in which $n_{gas} \sim 1.3 \cdot 10^{-5} \text{cm}^{-3}$.

In absence of a full Re-ionisation simulation setting the initial conditions for the ionisation fractions of H, He, C, O, Si at specific redshift, I have decided to start the simulation from a neutral configuration at temperature of $T = 100\text{K}$ and to wait for an equilibrium time $t_{eq} \sim 4 \cdot 10^2 \text{yrs}$ defined when a fully ionised configuration is reached. This corresponds to a volume average ionisation fraction of He III : $x_{\text{HeIII}} \sim 0.99999$. The simulation is set up with a duration of $t_f = 7 \cdot 10^6 \text{yrs}$; this means that the equilibrium configuration is found after few steps.

A special attention is also required for the temperature correction (see Section 4.3.3) set-up and the radiation tracking strategy (see Section 4.3.1).

Because I am interested in the fluctuations of both temperature and ionisation fractions, it is very important to guarantee a self-consistent treatment between metal cooling and metal ionisation. For these reasons the temperature correction algorithm is enabled in the primary set of runs, while additional simulations with the correction disabled are also performed to disentangle the importance of the metal cooling feedback on the temperature fluctuations and on the global ionisation equilibrium.

To establish the radiation tracking, a boolean mask Π_k is built as follows. First, a pre-analysis of the metal enriched cells is done (see 4.3.1) and Π_k is prepared to account for the global spatial distribution without discriminating between metal species. The pattern

Sim. Name	$L_b(\text{Mpc})$	$t_f(\text{yrs})$	δT_k correction	Metal enrichment	Emission Mask nodes
UVB_0	$10h^{-1}$	$7 \cdot 10^6$	no	yes, self-consistent	32^3
UVB_1	$10h^{-1}$	$7 \cdot 10^6$	yes	yes, self-consistent	32^3
UVB_2	$10h^{-1}$	$7 \cdot 10^6$	yes	yes, Schaye (2003)	32^3
UVB_3	$10h^{-1}$	$7 \cdot 10^6$	no	yes, Schaye (2003)	32^3
UVB_4	$10h^{-1}$	$7 \cdot 10^6$	no	no	32^3

Table 5.1: UVB simulation grid set-up

described by Π_k contains information about the realistic metal spreading simulated in the hydro run. As explained in Chapter 4, Π_k is used to track the radiation in the enriched cells but another application is possible, as explained below.

In realistic cases, metals are not present in the enriched cells following the ratios prescribed by the standard solar composition and I have already discussed in Section 5.2 that the ratio $\tau_{\text{CIV}}/\tau_{\text{SiIV}}$ could be sensitive to the variations of relative metal abundances. To disentangle the role of this effect, I have planned a series of runs in which the metal enriched cells distribution in space is described by Π_k but their metallicities are established by a semi-analytic prescription involving the gas over-density Δ and the solar composition ratios. For example the gas metallicity Z_g could be established by using the prescription of Schaye (2003) [223]: $[\text{C}/\text{H}] = -3.47 + 0.65 (\log \Delta - 0.5)$; this is also used by Bolton and Viel ([31]) to account for the metals in their simulations.

The metal enriched cells have then the same spatial distribution (self-consistent with the simulated metal spreading), but the ratios of metal species is fixed by the solar ratios.

The full set of simulations is summarised in Table 5.1.

5.4.3 Fluctuations in η - Preliminary results.

As preliminary result of the runs described in the previous Section, I show the value of the η parameter (see Section 5.1.3) as resulting from the simulation UVB_4 in Table 5.1; the results refer to the RT simulation on a configuration including just H and He.

The value of η can be evaluated during a CRASH simulation by using one approximation of the Formula 5.10 (see [77, 158]):

$$\eta \equiv \frac{\alpha_{\text{HeII}} n_{\text{HeIII}} \Gamma_{\text{HI}}}{\alpha_{\text{HI}} n_{\text{HII}} \Gamma_{\text{HeII}}}, \quad (5.12)$$

were the CASE A recombination coefficients introduced in Equation 5.8 and their ratio can be considered constant. Γ_{HI} and Γ_{HeII} are provided instead by the simulation as explained in Section 5.3.2.

Before calculating the value of η in the simulation UVB_4, I have evaluated the scatter of η in the uniformity test as an estimate of the UVB noise induced by the MC sampling. By applying Formula 5.12 to the uniform case, one can derive a relative error in η of about 2.5 percent for $n_{\text{gas}} \sim 10^{-5} \text{cm}^{-3}$, i.e. the mean value of the number density of UVB_4.

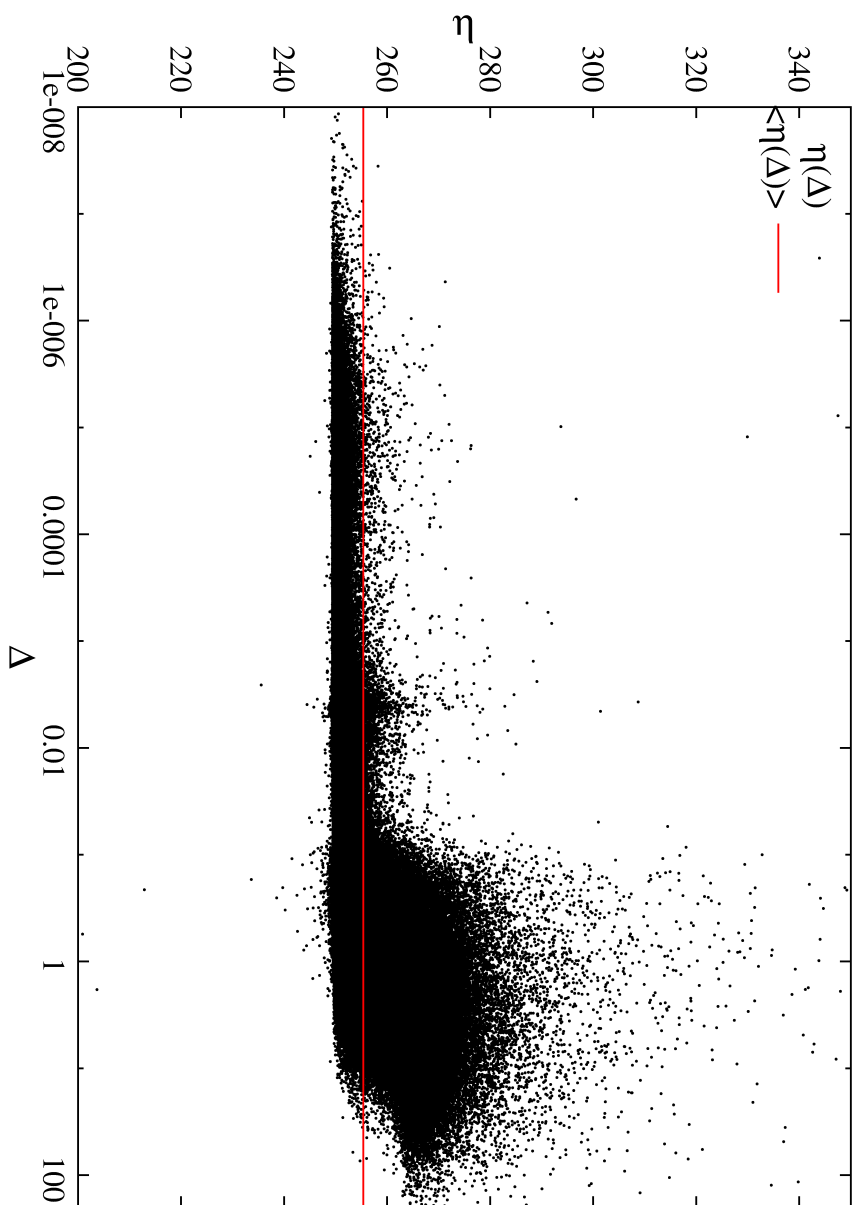


Figure 5.3: UVB Simulation: η parameter as function of the over-density Δ (black points). $\langle \eta \rangle$ over the cells (solid red line).

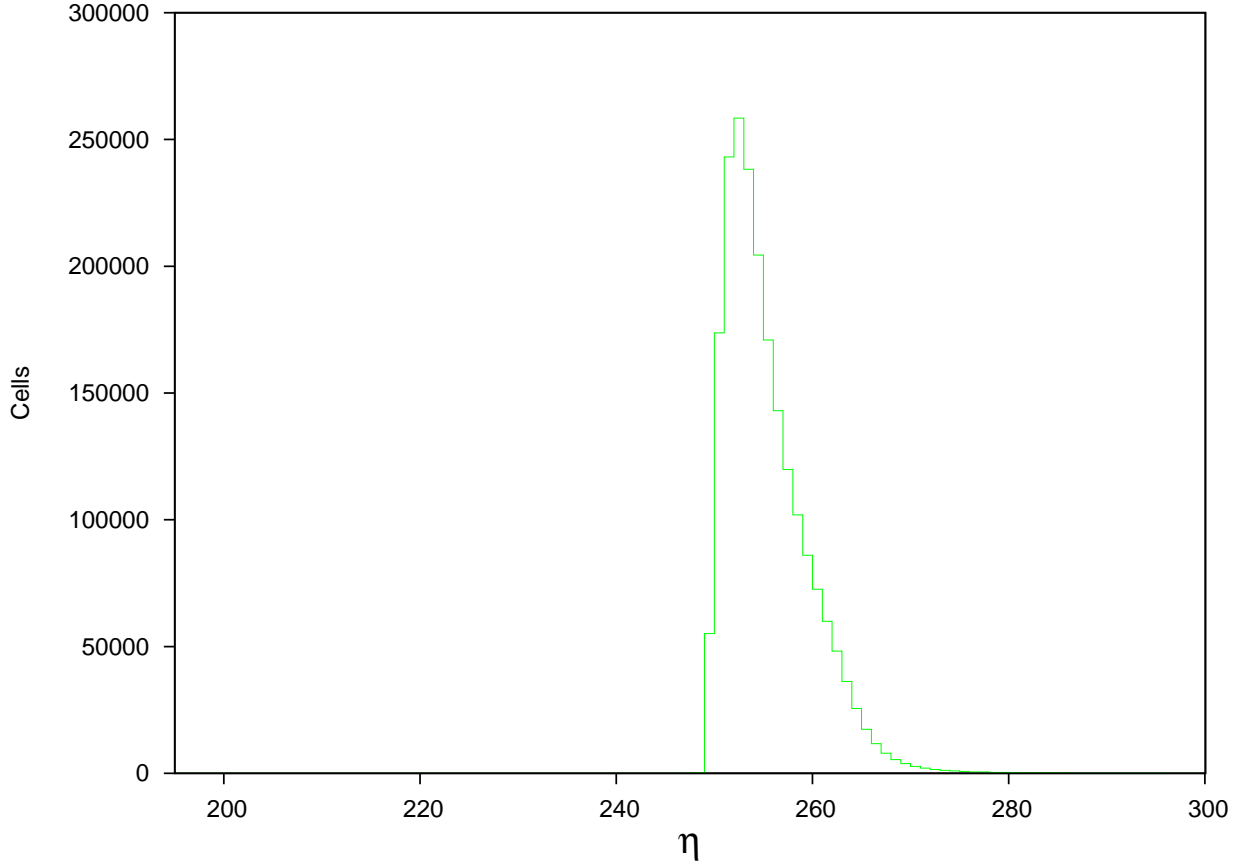


Figure 5.4: UVB Simulation: statistical distribution of η . Total number of cells with fixed η parameter in the simulated volume (green line).

This threshold of 2.5 percent must be considered as the noise of the method in reproducing a uniform UVB.

Once the noise of this case has been established, I have estimated η in the UVB.4 simulation in each cell of the domain. In Figure 5.3 the values of η (black points) are shown as function of the gas over-density Δ . The values of η for $\Delta > 200$ are not shown in this Figure because in this interval there are only few points. The mean value $\langle \eta \rangle \sim 255$ calculated considering all the cells is also shown in solid red line. Although a complete analysis is not available some qualitative trends can be noticed as discussed below.

In low density regions of the map, where $\Delta < 0.1$ the majority of the points have a low scatter (from 5 to 10 percent) around the mean value $\langle \eta \rangle \sim 252$, while some cell showing deviations up to 15 percent.

When the gas density varies of about one order of magnitude around the mean density (i.e. $0.1 < \Delta < 10$) the fluctuations around $\langle \eta \rangle \sim 258$ start increasing in absolute value

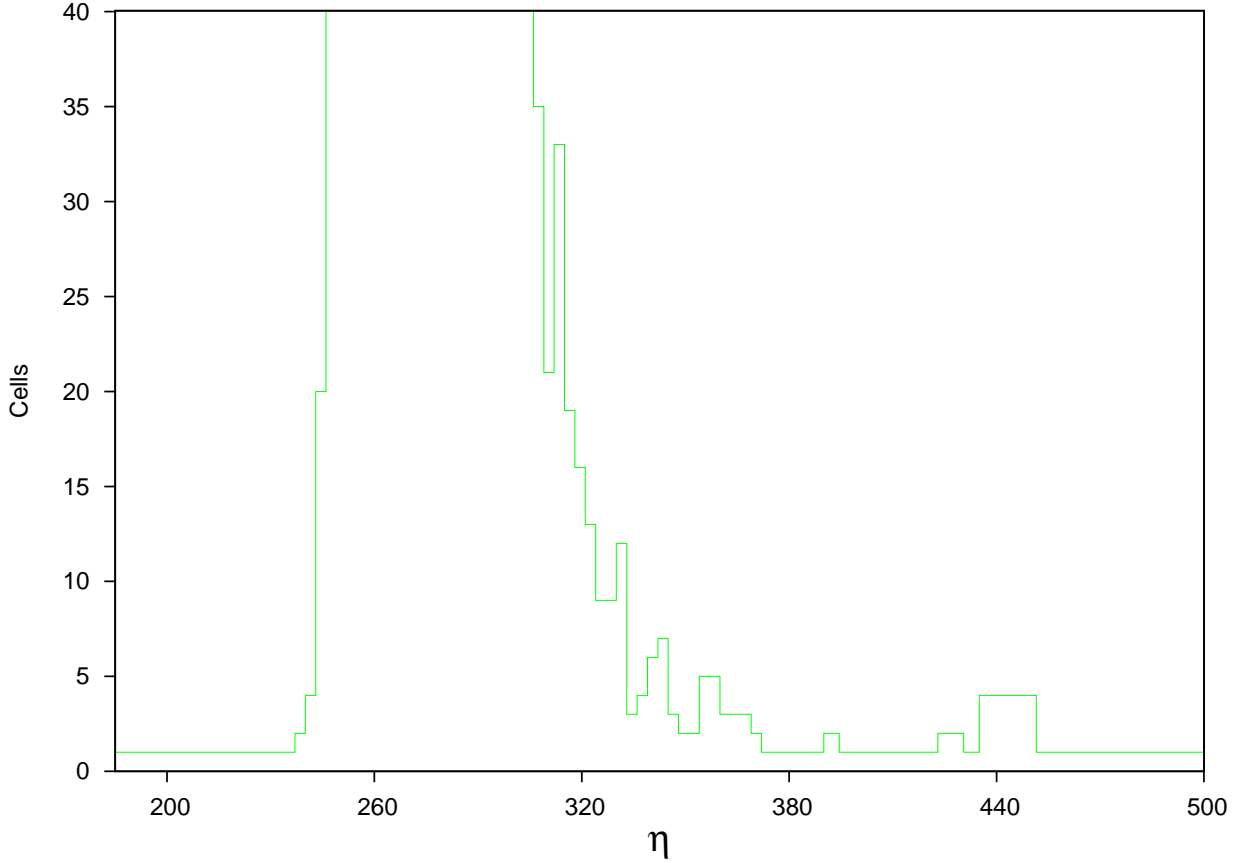


Figure 5.5: UVB Simulation: statistical distribution of $200 < \eta < 500$. Total number of cells with $200 < \eta < 500$ parameter in the simulated volume (green line).

with the increase of Δ . The mean scatter oscillates from 10 to 15 percent while a large number of cells reaches a deviation of 30 percent. A very reduced statistical sample is involved instead by deviations higher than 37 percent. An increase in the average value of η with Δ is present (e.g. $\langle \eta \rangle \sim 270$ when $50 < \Delta < 100$).

A substantial decrease of these fluctuations, down to some percent can be verified in the data at higher over-densities (up to $\Delta > 150$), while at $\Delta \gtrsim 200$ the low number of involved cells creates oscillations also in the mean value. Notice that this fact is also linked to the coarse resolution of the adopted grid which impedes a better resolution of the over-density gradients.

The existence of a correlation between η and Δ is suggested by these preliminary results in agreement with Maselli and Ferrara; on the other hand the spatial deviations of the UVB spectral shape must be deeply investigated over the entire volume of the simulation, and cross correlated with the values of the ratio $\tau_{\text{CIV}}/\tau_{\text{SiIV}}$ (which are still under evaluation) before fixing any new constraint to the shape of the fluctuations. The relation $\eta(\Delta)$ established by the radiative transfer effects in this box could vary with the

scale and additional runs should be planned to investigate how the law changes with the spatial scale of the simulation and its resolution.

In Figure 5.4 a preview of the statistical distribution of η is shown as 'number of cells' at fixed η . It is immediately clear that the largest part of the domain is involved by oscillations down to 7 percent around the average value of $\langle \eta \rangle \sim 255$, while only a negligible number of cells (< 30 for each over-density bin) is involved by $\eta > 300$. Finally, only few cells have values of η higher than 350, as shown in the last Figure. The statistics of η is in fact biased by the large number of cells at $\Delta < 0.1$, which strongly reduce the significance of the fluctuations over the entire volume. In under-dense regions in fact, the photo-ionisation equilibrium seems to be easily maintained by the UVB over large physical volumes (i.e. a large number of cells), with reduced oscillations in the photo-ionisation rates of hydrogen and helium.

To summarise, I can conclude that these preliminary results are in statistical agreement with the conclusions of Maselli and Ferrara about the correlation between η and Δ but the $\eta - \Delta$ anti-correlation they found in over-dense regions seems to be less evident. Moreover, in the new UV background scheme, the impact of the RT on the fluctuations on the η parameter seems sensitively reduced to an average value of 20 percent present in the over-density range $0.1 < \Delta < 10$.

A definite confirmation of these results will come from the data provided by the other simulations described in Table 5.1 and a more adequate statistical analysis.

Chapter 6

Conclusions

In this thesis the radiative transfer (RT) problem has been investigated in some of its applications to the physics of the Intergalactic Medium (IGM). The RT is in fact one of the main ingredients required to understand the observed properties of the IGM (e.g. through the Ly α forest) and to simulate its cosmological evolution through the Re-ionisation process. The modelling of Re-ionisation with the inclusion of all the relevant physics is a tremendous challenge, both theoretically and numerically, and it requires a robust and reliable radiative transfer code. For these reasons I spent a large part of my PhD project in re-engineering, optimising and extending the radiative transfer code **CRASH** which has been developed within my group.

CRASH is a general 3D radiative transfer scheme implementing a wide set of atomic processes regulating the ionisation state and temperature of hydrogen and helium, as well as a sophisticated multi-frequency treatment of the ionising radiation field. The code re-engineering and re-modelling has then required a deep understanding of every part of the algorithm, as described in Chapter 3.

As a first result of this intense numerical work I have released a new version of **CRASH** which changes completely the previous numerical implementation of the radiative transfer algorithm (while maintaining the same physical description) and uses a modern development scheme with a coherent code modularisation technique. This new release dramatically improves the performances of the code, in terms of gain in computation time as well as flexibility. In fact, the work I have done makes the extension of the code with additional physics and/or features a much easier task.

The new **CRASH** code reliability has been tested with a wide range of idealised tests and its many new features have already been used to run a number of state of the art numerical simulations of cosmic Re-ionisation.

The improved expandability of **CRASH** opens new perspectives for future developments within a unified coding scheme based on modules. In this respect, I have already implemented and I am presently testing two new modules which follow the physics of the x-rays and of the scattering of Ly α photons.

The inclusion of dust is another extension to the code I am presently considering.

In addition to the re-engineering of the code, another large part of my PhD thesis was

devoted to the inclusion of a self-consistent treatment of the radiative transfer through metals, taking advantage of the excellent capabilities of the code `Cloudy` in simulating the photo-ionisation of a metal enriched gas. In fact, the interpretation of observations of metal ionisation states in the IGM (which are used, among others, to set constraints on the shape of the UVB at different redshifts as well as on the metal enrichment history) requires an accurate modelling of the radiative transfer effects.

Although `Cloudy` has a long reputation in simulating HII regions with a great level of detail, its implementation is very focused on a specific set of physical problems and thus it cannot be used as a general photo-ionisation code. For this reason I have decided to use a modular approach, integrating the two codes in a common pipeline. This part of the work and the associated challenges have been described in detail in Chapter 4. In the same Chapter the new code, called `CRASH3`, has been fully tested in a number of idealised cases (as a Strömgren sphere enriched with metals) as well as in the more realistic context of a cosmological hydrodynamic simulation.

The final release of a fully tested software pipeline is the main result of this second part of my project. `CRASH3` allows us to derive the metal ionisation fractions self-consistently with the details of the radiative transfer through highly inhomogeneous media as proven by the numerous tests performed. The feedback of metals on the gas temperature can also be taken into account self-consistently, opening a wide range of future physical applications.

The last part of my PhD has been spent to study the problem of the UV background fluctuations at the epoch of the helium Re-ionisation at $z \sim 3$ as a possible, first application of `CRASH3`. The problem of constraining the amplitude of such fluctuations and understanding the relative role of RT versus the effects induced by the source properties, is of primary importance. Moreover the shape of the UV background can be inferred through observations of ionised states of the metals contaminating the IGM. `CRASH3` seems then the right tool to investigate this problem as widely discussed in Chapter 5.

The application of the new pipeline to the simulation of a UV background has required a further extension. As first step I have provided a novel implementation of the UVB scheme spending a considerable time in reducing the numerical noise in the simulated field. This is necessary to safely and correctly interpret the metal ion fluctuations through the cosmic web because it guarantees that they are physical and not induced by the Monte Carlo noise intrinsic in our RT code.

The new implementation has been used to model the UVB using realistic hydrodynamic simulations of galaxy formation and metal enrichment. A first set of results has already been produced.

Bibliography

- [1] K.L. Adelberger, A.E. Shapley, C.C. Steidel, M. Pettini, D.K. Erb und N.A. Reddy, *ApJ* **629** (2005), 636. 2.2, 2.2.1
- [2] I.I. Agafonova, M. Centurión, S.A. Levshakov und P. Molaro, *AAP* **441** (2005), 9. 5.2
- [3] I.I. Agafonova, S.A. Levshakov, D. Reimers, C. Fechner, D. Tytler, R.A. Simcoe und A. Songaila, *AAP* **461** (2007), 893. 5.2
- [4] A. Aguirre, C. Dow-Hygelund, J. Schaye und T. Theuns, *ApJ* **689** (2008), 851. 5.2
- [5] A. Aguirre, L. Hernquist, J. Schaye, N. Katz, D.H. Weinberg und J. Gardner, *ApJ* **561** (2001), 521. 2.2.2
- [6] A. Aguirre, J. Schaye, T.S. Kim, T. Theuns, M. Rauch und W.L.W. Sargent, *ApJ* **602** (2004), 38. 5.2
- [7] K. Alatalo, L. Blitz, L.M. Young, T.A. Davis, M. Bureau, L.A. Lopez, M. Cappellari, N. Scott, K.L. Shapiro, A.F. Crocker, S. Martín, M. Bois, F. Bournaud, R.L. Davies, P.T. de Zeeuw, P.A. Duc, E. Emsellem, J. Falcón-Barroso, S. Khochfar, D. Krajinović, H. Kuntschner, P.Y. Lablanche, R.M. McDermid, R. Morganti, T. Naab, T. Oosterloo, M. Sarzi, P. Serra und A. Weijmans, *ApJ* **735** (2011), 88. 2.4
- [8] A. Albrecht und P.J. Steinhardt, *Physical Review Letters* **48** (1982), 1220. 1.1
- [9] M.G. Allen, B.A. Groves, M.A. Dopita, R.S. Sutherland und L.J. Kewley, *ApJS* **178** (2008), 20. 2.2.3
- [10] B. Aracil, P. Petitjean, C. Pichon und J. Bergeron, *AAP* **419** (2004), 811. 2.2.1
- [11] S. Baek, B. Semelin, P. Di Matteo, Y. Revaz und F. Combes, *AAP* **523** (2010), A4+. 2.2.3
- [12] R. Barkana und A. Loeb, *Reports on Progress in Physics* **70** (2007), 627. 2, 2.1

- [13] M. Bartelmann, C.L. Bennett, C. Burigana, C. Chiosi, M. D’Onofrio, A. Dressler, I. Gioia, G. Hasinger, J.F. Macias-Perez, P. Madau, P. Marziani, J. Mather, F. Matteucci, K. Olive, J. Peacock, W. Reich, P.M. Robitaille, M. Rowan-Robinson, G. Steigman, M. Steinmetz, J.W. Sulentic, M. Turatto und S.D.M. White. *Fundamental Cosmological Observations and Data Interpretation*, 2009. Seiten 7–202. 1.2
- [14] J. Bechtold: *Quasar absorption lines. Quasar absorption lines*, In *Galaxies at High Redshift*, herausgegeben von I. Pérez-Fournon, M. Balcells, F. Moreno-Insertis, & F. Sánchez. (2003) Seiten 131–184. 2.1
- [15] J. Bechtold, R.J. Weymann, Z. Lin und M.A. Malkan, *ApJ* **315** (1987), 180. 5.2
- [16] G.D. Becker, J.S. Bolton, M.G. Haehnelt und W.L.W. Sargent, *MNRAS* **410** (2011), 1096. 5.1
- [17] G.D. Becker, M. Rauch und W.L.W. Sargent, *ApJ* **698** (2009), 1010. 2, 2.2.1
- [18] G.D. Becker, W.L.W. Sargent, M. Rauch und A.P. Calverley, *ApJ* **735** (2011), 93. 2, 2.2.1
- [19] P. Berczik, *AAP* **348** (1999), 371. 2.2.2
- [20] M. Bernardi, R.K. Sheth, M. SubbaRao, G.T. Richards, S. Burles, A.J. Connolly, J. Frieman, R. Nichol, J. Schaye, D.P. Schneider, D.E. Vanden Berk, D.G. York, J. Brinkmann und D.Q. Lamb, *AJ* **125** (2003), 32. 5.1.1
- [21] G. Bertone, D. Hooper und J. Silk, *PhysRep* **405** (2005), 279. 1.2
- [22] S. Bertone, G. De Lucia und P.A. Thomas, *MNRAS* **379** (2007), 1143. 2.2.2
- [23] S. Bertone, F. Stoehr und S.D.M. White, *MNRAS* **359** (2005), 1201. 2.2.2
- [24] S. Bertone und S.D.M. White, *MNRAS* **367** (2006), 247. 2.2.2
- [25] S. Bianchi, S. Cristiani und T.S. Kim, *AAP* **376** (2001), 1. 5.2
- [26] A. Boksenberg, W.L.W. Sargent und M. Rauch, *ArXiv Astrophysics e-prints* (2003). 5.2
- [27] J.S. Bolton, G.D. Becker, J.S.B. Wyithe, M.G. Haehnelt und W.L.W. Sargent, *MNRAS* **406** (2010), 612. 5.1
- [28] J.S. Bolton und M.G. Haehnelt, *MNRAS* **382** (2007), 325. 5.1
- [29] J.S. Bolton, M.G. Haehnelt, M. Viel und R.F. Carswell, *MNRAS* **366** (2006), 1378. 5.1.3, 5.2

- [30] J.S. Bolton, S.P. Oh und S.R. Furlanetto, *MNRAS* **396** (2009), 2405. 5.1.2, 5.1.2
- [31] J.S. Bolton und M. Viel, *MNRAS* **414** (2011), 241. 5.2, 5.4.2
- [32] J.R. Bond, L. Kofman und D. Pogosyan, *NATURE* **380** (1996), 603. 2
- [33] S. Borgani, D. Fabjan, L. Tornatore, S. Schindler, K. Dolag und A. Diaferio, *SSR* **134** (2008), 379. 2.2.2
- [34] M. Boylan-Kolchin, V. Springel, S.D.M. White, A. Jenkins und G. Lemson, *MNRAS* **398** (2009), 1150. 1.2
- [35] S.M. Carroll, *Living Reviews in Relativity* **4** (2001), 1. 1.2
- [36] S.M. Carroll: *Why is the Universe Accelerating? Why is the Universe Accelerating?*, In *The New Cosmology: Conference on Strings and Cosmology*, herausgegeben von R. E. Allen, D. V. Nanopoulos, & C. N. Pope, Band 743 von *American Institute of Physics Conference Series*. (Dezember 2004) Seiten 16–32. 1
- [37] R.F. Carswell: *Properties of the Ly-alpha clouds. Properties of the Ly-alpha clouds*, In *Proceedings of the QSO Absorption Line Meeting*, herausgegeben von J. C. Blades, D. A. Turnshek, & C. A. Norman. (1988) Seiten 91–100. 2.1.1
- [38] R.F. Carswell: *QSO absorption lines, winds, and the high-redshift intergalactic medium. QSO absorption lines, winds, and the high-redshift intergalactic medium*, In *A Massive Star Odyssey: From Main Sequence to Supernova*, herausgegeben von K. van der Hucht, A. Herrero, & C. Esteban, Band 212 von *IAU Symposium*. (2003) Seiten 681–+. 2.2.1
- [39] R. Cen und G.L. Bryan, *ApJL* **546** (2001), L81. 2.2, 2.2.1
- [40] R. Cen und T. Fang, *ApJ* **650** (2006), 573. 2.2.1
- [41] R. Cen, J. Miralda-Escudé, J.P. Ostriker und M. Rauch, *ApJL* **437** (1994), L9. 2.1.1
- [42] R. Cen, K. Nagamine und J.P. Ostriker, *ApJ* **635** (2005), 86. 2.2.2
- [43] R. Cen und J.P. Ostriker, *ApJL* **399** (1992), L113. 5
- [44] R. Cen und J.P. Ostriker, *ApJ* **514** (1999), 1. 2
- [45] R. Cen, T.M. Tripp, J.P. Ostriker und E.B. Jenkins, *ApJL* **559** (2001), L5. 2, 2.2.2
- [46] S. Chandrasekhar: *Radiative transfer*, 1960. 3.2
- [47] J. Charlton, C. Churchill und P. Murdin. *Quasistellar Objects: Intervening Absorption Lines*, November 2000. 2.1
- [48] X. Chen, D.H. Weinberg, N. Katz und R. Davé, *ApJ* **594** (2003), 42. 2.2.1

- [49] B. Ciardi, J.S. Bolton, A. Maselli und L. Graziani, *ArXiv e-prints* (2011). 2.2.3, 3.3, 5.1, 5.1.3, 5.3
- [50] B. Ciardi und A. Ferrara, *SSR* **116** (2005), 625. 1.2, 2, 2.2, 2.2.1
- [51] B. Ciardi, A. Ferrara, S. Marri und G. Raimondo, *MNRAS* **324** (2001), 381. 3.2.1, 3.3
- [52] B. Ciardi, A. Ferrara und S.D.M. White, *MNRAS* **344** (2003), L7. 2.2.3, 3.3, 5.1.3
- [53] B. Ciardi und A. Loeb, *ApJ* **540** (2000), 687. 2.1
- [54] B. Ciardi, F. Stoehr und S.D.M. White, *MNRAS* **343** (2003), 1101. 2.2.3, 3.3, 5.1.3
- [55] P. Coles: *Large-scale Structure, Theory and Statistics. Large-scale Structure, Theory and Statistics*, In *Phase Transitions in the Early Universe: Theory and Observations*, herausgegeben von H. J. de Vega, I. M. Khalatnikov, & N. G. Sanchez. (2001) Seite 217. 1
- [56] L.L. Cowie und A. Songaila, *NATURE* **394** (1998), 44. 2.2.1
- [57] R.A.C. Croft, *ApJ* **610** (2004), 642. 5.1.3
- [58] A.P.S. Crofts und Y. Fang, *ApJ* **502** (1998), 16. 2.1.1
- [59] C.W. Danforth und J.M. Shull, *ApJ* **624** (2005), 555. 2.2.1, 2.2.2
- [60] C.W. Danforth und J.M. Shull: *The Ly β and O VI Forest in the Local Universe. The Ly β and O VI Forest in the Local Universe*, In *Astrophysics in the Far Ultraviolet: Five Years of Discovery with FUSE*, herausgegeben von G. Sonneborn, H. W. Moos, & B.-G. Andersson, Band 348 von *Astronomical Society of the Pacific Conference Series*. (Juni 2006) Seite 357. 2.2.1
- [61] C.W. Danforth, J.M. Shull, J.L. Rosenberg und J.T. Stocke, *ApJ* **640** (2006), 716. 2.2.1, 2.2.2
- [62] R. Davé: *Simulations of the Intergalactic Medium. Simulations of the Intergalactic Medium*, In *Maps of the Cosmos*, herausgegeben von M. Colless, L. Staveley-Smith, & R. A. Stathakis, Band 216 von *IAU Symposium*. (Januar 2005) Seiten 251–+. 2
- [63] R. Davé, R. Cen, J.P. Ostriker, G.L. Bryan, L. Hernquist, N. Katz, D.H. Weinberg, M.L. Norman und B. O’Shea, *ApJ* **552** (2001), 473. 2
- [64] R. Davé, L. Hernquist, N. Katz und D.H. Weinberg, *ApJ* **511** (1999), 521. 2
- [65] R. Davé, B.D. Oppenheimer, N. Katz, J.A. Kollmeier und D.H. Weinberg, *MNRAS* **408** (2010), 2051. 2.2.2

- [66] A.F. Davidsen, G.A. Kriss und W. Zheng, *NATURE* **380** (1996), 47. 2.1.1, 5.1.3
- [67] G. De Lucia, G. Kauffmann und S.D.M. White, *MNRAS* **349** (2004), 1101. 2.2.2
- [68] R.H. Dicke, P.J.E. Peebles, P.G. Roll und D.T. Wilkinson, *ApJ* **142** (1965), 414. 1.1
- [69] K.L. Dixon und S.R. Furlanetto, *ApJ* **706** (2009), 970. 5.1
- [70] M.A. Dopita und R.S. Sutherland: *Astrophysics of the diffuse universe*, 2003. 4.1, 4.2
- [71] B.T. Draine: *Physics of the Interstellar and Intergalactic Medium*, 2011. 2.2.1, 3.1, 4.1, 4.2, 5.1
- [72] Y. Dubois und R. Teyssier: *Metal enrichment in galactic winds. Metal enrichment in galactic winds*, In *EAS Publications Series*, herausgegeben von E. Emsellem, H. Wozniak, G. Massacrier, J.-F. Gonzalez, J. Devriendt, & N. Champavert, Band 24 von *EAS Publications Series*. (2006) Seiten 95–100. 2.2.2
- [73] G. Efstathiou, *MNRAS* **256** (1992), 43P. 5
- [74] S.L. Ellison, A. Songaila, J. Schaye und M. Pettini, *AJ* **120** (2000), 1175. 2.2.1
- [75] X. Fan. *Observational Constraints of Reionization History in the JWST Era*, 2009. Seite 457. 2.1
- [76] T. Fang und G.L. Bryan, *ApJL* **561** (2001), L31. 2.2.1
- [77] M.A. Fardal, M.L. Giroux und J.M. Shull, *AJ* **115** (1998), 2206. 5.1, 5.1.3, 5.1.3, 5.2, 5.4.3
- [78] M.A. Fardal und J.M. Shull, *ApJ* **415** (1993), 524. 5.1.3
- [79] C.A. Faucher-Giguère, A. Lidz, L. Hernquist und M. Zaldarriaga, *ApJ* **688** (2008), 85. 5.1.3
- [80] C.A. Faucher-Giguère, A. Lidz, M. Zaldarriaga und L. Hernquist, *ApJ* **703** (2009), 1416. 5.2
- [81] C. Fechner und D. Reimers, *AAP* **461** (2007), 847. 5.1.3
- [82] G.J. Ferland, *ARAA* **41** (2003), 517. 4.1, 4.2
- [83] G.J. Ferland, K.T. Korista, D.A. Verner, J.W. Ferguson, J.B. Kingdon und E.M. Verner, *PASP* **110** (1998), 761. 2.2.3, 4, 4.1, 4.2
- [84] A. Ferrara, F. Ferrini, B. Barsella und J. Franco, *ApJ* **381** (1991), 137. 2.2.2
- [85] A. Ferrara, M. Pettini und Y. Shchekinov, *MNRAS* **319** (2000), 539. 2.2, 2.2.2

- [86] W.L. Freedman, B.F. Madore, B.K. Gibson, L. Ferrarese, D.D. Kelson, S. Sakai, J.R. Mould, R.C. Kennicutt, Jr., H.C. Ford, J.A. Graham, J.P. Huchra, S.M.G. Hughes, G.D. Illingworth, L.M. Macri und P.B. Stetson, *ApJ* **553** (2001), 47. 1.1
- [87] C.S. Frenk, S.D.M. White, M. Davis und G. Efstathiou, *ApJ* **327** (1988), 507. 1.2
- [88] M. Fukugita, C.J. Hogan und P.J.E. Peebles, *ApJ* **503** (1998), 518. 2
- [89] M. Fumagalli, J.M. O'Meara und J.X. Prochaska, *Science* **334** (2011), 1245. (document), 2.1, 2.2.1, 2.6
- [90] S.R. Furlanetto, *ApJ* **703** (2009), 702. 2.2.3, 5.1.3
- [91] S.R. Furlanetto, *ApJ* **700** (2009), 1666. 5.1.3
- [92] S.R. Furlanetto und K.L. Dixon, *ApJ* **714** (2010), 355. 5.1.3
- [93] S.R. Furlanetto und A. Lidz, *ApJ* **735** (2011), 117. 5.2
- [94] S.R. Furlanetto und A. Loeb, *ApJ* **556** (2001), 619. 2
- [95] S.R. Furlanetto und A. Loeb, *ApJ* **588** (2003), 18. 2.2.2, 2.2.3
- [96] S.R. Furlanetto, L.A. Phillips und M. Kamionkowski, *MNRAS* **359** (2005), 295. 2.2.1
- [97] G. Gamow und E. Teller, *Physical Review* **55** (1939), 654. 1.1
- [98] M.L. Giroux und P.R. Shapiro, *ApJS* **102** (1996), 191. 5.2
- [99] M.L. Giroux und J.M. Shull, *AJ* **113** (1997), 1505. 5.2
- [100] N.Y. Gnedin, *MNRAS* **294** (1998), 407. 2.2.2, 2.2.2
- [101] N.Y. Gnedin und J.P. Ostriker, *ApJ* **486** (1997), 581. 2.2
- [102] F. Governato, B. Willman, L. Mayer, A. Brooks, G. Stinson, O. Valenzuela, J. Wadsley und T. Quinn, *MNRAS* **374** (2007), 1479. 2.2.2
- [103] L. Graziani, L. Barletti, S. Aiello und C. Cecchi-Pestellini, *Mathematical Methods in the Applied Sciences* **33** (2010), 1263. 3.2.1
- [104] L. Graziani, A. Maselli und B. Ciardi, *in prep.* (2012). 4, 5
- [105] N. Grevesse und A.J. Sauval, *SSR* **85** (1998), 161. 4.2
- [106] A.J. Grocholski, A. Aloisi, R.P. van der Marel, J. Mack, F. Annibali, L. Angeretti, L. Greggio, E.V. Held, D. Romano, M. Sirianni und M. Tosi, *ApJL* **686** (2008), L79. (document)

- [107] S.E.L.A. Gropp W.: *Using MPI Portable Parallel Programming with the Message-Passing Interface second edition*. The MIT Press Scientific and Engineering Computation Series, 1999. 3.2.1
- [108] J.E. Gunn und B.A. Peterson, *ApJ* **142** (1965), 1633. 2.1
- [109] F. Haardt und P. Madau, *ApJ* **461** (1996), 20. 5.1.3, 5.2, 5.3.1, 5.3.2, 5.1, 5.2
- [110] F. Haardt und P. Madau: *Modelling the UV/X-ray cosmic background with CUBA. Modelling the UV/X-ray cosmic background with CUBA*, In *Clusters of Galaxies and the High Redshift Universe Observed in X-rays*, herausgegeben von D. M. Neumann & J. T. V. Tran. (2001). 5.1.3, 5.2
- [111] F. Haardt und P. Madau, *ArXiv e-prints* (2011). 5.2
- [112] M.G. Haehnelt, M. Steinmetz und M. Rauch, *ApJL* **465** (1996), L95. 2.2.2
- [113] C. Hazard, M.B. Mackey und A.J. Shimmins, *NATURE* **197** (1963), 1037. 2.1
- [114] S.R. Heap, G.M. Williger, A. Smette, I. Hubeny, M.S. Sahu, E.B. Jenkins, T.M. Tripp und J.N. Winkler, *ApJ* **534** (2000), 69. 5.1.3
- [115] T. Heckman: *Starburst-Driven Outflows and the Evolution of Dwarf Galaxies. Starburst-Driven Outflows and the Evolution of Dwarf Galaxies*, In *Chandra Proposal*. (September 2000) Seite 638. 2.2.1
- [116] T.M. Heckman, M.D. Lehnert, D.K. Strickland und L. Armus, *ApJS* **129** (2000), 493. 2.2.1
- [117] T.M. Heckman, C.A. Norman, D.K. Strickland und K.R. Sembach, *ApJ* **577** (2002), 691. 2.2.1
- [118] U. Hellsten, R. Dave, L. Hernquist, D.H. Weinberg und N. Katz, *ApJ* **487** (1997), 482. 2.2.1
- [119] L. Hernquist, N. Katz, D.H. Weinberg und J. Miralda-Escudé, *ApJL* **457** (1996), L51. 2.1.1
- [120] C.J. Hogan, S.F. Anderson und M.H. Rugers, *AJ* **113** (1997), 1495. 5.1.3
- [121] P.F. Hopkins, G.T. Richards und L. Hernquist, *ApJ* **654** (2007), 731. 5.1, 5.2
- [122] I. Hubeny: *From Escape Probabilities to Exact Radiative Transfer. From Escape Probabilities to Exact Radiative Transfer*, In *Spectroscopic Challenges of Photoionized Plasmas*, herausgegeben von G. Ferland & D. W. Savin, Band 247 von *Astronomical Society of the Pacific Conference Series*. (2001) Seiten 197–+. 4.2
- [123] L. Hui und N.Y. Gnedin, *MNRAS* **292** (1997), 27. 5.1.1, 5.1.1

- [124] I.T. Iliev, B. Ciardi, M.A. Alvarez, A. Maselli, A. Ferrara, N.Y. Gnedin, G. Mellema, T. Nakamoto, M.L. Norman, A.O. Razoumov, E.J. Rijkhorst, J. Ritzerveld, P.R. Shapiro, H. Susa, M. Umemura und D.J. Whalen, *MNRAS* **371** (2006), 1057. 2.2.3, 3.2, 3.3, 4.3.3, 4.4.1, 4.4.3
- [125] I.T. Iliev, G. Mellema, U.L. Pen, H. Merz, P.R. Shapiro und M.A. Alvarez, *MNRAS* **369** (2006), 1625. 2.2.3
- [126] I.T. Iliev, D. Whalen, G. Mellema, K. Ahn, S. Baek, N.Y. Gnedin, A.V. Kravtsov, M. Norman, M. Raicevic, D.R. Reynolds, D. Sato, P.R. Shapiro, B. Semelin, J. Smidt, H. Susa, T. Theuns und M. Umemura, *MNRAS* **400** (2009), 1283. 2.2.3, 3.2
- [127] P. Jakobsen, A. Boksenberg, J.M. Deharveng, P. Greenfield, R. Jedrzejewski und F. Paresce, *NATURE* **370** (1994), 35. 5.1.3
- [128] G. Kauffmann, J.M. Colberg, A. Diaferio und S.D.M. White, *MNRAS* **303** (1999), 188. 1.2
- [129] D. Kawata, *ApJ* **558** (2001), 598. 2.2.2
- [130] D. Kawata und B.K. Gibson, *MNRAS* **340** (2003), 908. 2.2.2
- [131] R.C. Kennicutt, Jr., *ARAA* **36** (1998), 189. 2.2.2
- [132] T.S. Kim, S. Cristiani und S. D’Odorico, *AAP* **383** (2002), 747. 5.2
- [133] C. Kobayashi, V. Springel und S.D.M. White, *MNRAS* **376** (2007), 1465. 2.2.2
- [134] E. Komatsu, J. Dunkley, M.R. Nolta, C.L. Bennett, B. Gold, G. Hinshaw, N. Jarosik, D. Larson, M. Limon, L. Page, D.N. Spergel, M. Halpern, R.S. Hill, A. Kogut, S.S. Meyer, G.S. Tucker, J.L. Weiland, E. Wollack und E.L. Wright, *ApJS* **180** (2009), 330. 1.1, 1.2
- [135] E. Komatsu, K.M. Smith, J. Dunkley, C.L. Bennett, B. Gold, G. Hinshaw, N. Jarosik, D. Larson, M.R. Nolta, L. Page, D.N. Spergel, M. Halpern, R.S. Hill, A. Kogut, M. Limon, S.S. Meyer, N. Odegard, G.S. Tucker, J.L. Weiland, E. Wollack und E.L. Wright, *ApJS* **192** (2011), 18. 1.1, 1.2
- [136] G.A. Kriss, J.M. Shull, W. Oegerle, W. Zheng, A.F. Davidsen, A. Songaila, J. Tumlinson, L.L. Cowie, J.M. Deharveng, S.D. Friedman, M.L. Giroux, R.F. Green, J.B. Hutchings, E.B. Jenkins, J.W. Kruk, H.W. Moos, D.C. Morton, K.R. Sembach und T.M. Tripp, *Science* **293** (2001), 1112. 5.1
- [137] P.P. Kronberg, H. Lesch und U. Hopp, *ApJ* **511** (1999), 56. 2
- [138] R.P. Kudritzki, *ApJ* **577** (2002), 389. 2.2.1

- [139] V.P. Kulkarni, D.G. York, J.T. Lauroesch, S.M. Fall, P. Khare, B.E. Woodgate, P. Palunas, J. Meiring, D.G. Thatte, D.E. Welty und J.W. Truran: *The evolution of damped Ly- α absorbers: metallicities and star formation rates. The evolution of damped Ly- α absorbers: metallicities and star formation rates*, In *IAU Colloq. 199: Probing Galaxies through Quasar Absorption Lines*, herausgegeben von P. Williams, C.-G. Shu, & B. Menard. (März 2005) Seiten 307–312. 2.2.1
- [140] D.P. Landau und K. Binder: *A Guide to Monte Carlo Simulations in Statistical Physics - 2nd Edition*, September 2005. 3.2.1
- [141] S.A. Levshakov, I.I. Agafonova, D. Reimers, J.L. Hou und P. Molaro, *AAP* **483** (2008), 19. 5.2
- [142] C. Lia, L. Portinari und G. Carraro, *MNRAS* **335** (2002), 864. 2.2.2
- [143] C. Lia, L. Portinari und G. Carraro, *MNRAS* **330** (2002), 821. 2.2.2
- [144] M. Limongi und A. Chieffi: *Presupernova Evolution and Explosive Nucleosynthesis of Massive Stars at Various Metallicities from $Z=0$ to $Z=1Z_{sol}$. Presupernova Evolution and Explosive Nucleosynthesis of Massive Stars at Various Metallicities from $Z=0$ to $Z=1Z_{sol}$* , In *1604-2004: Supernovae as Cosmological Lighthouses*, herausgegeben von M. Turatto, S. Benetti, L. Zampieri, & W. Shea, Band 342 von *Astronomical Society of the Pacific Conference Series*. (Dezember 2005) Seite 122. 2.2.2
- [145] A.D. Linde, *Physics Letters B* **108** (1982), 389. 1.1
- [146] L. Lu, *ApJ* **379** (1991), 99. 2.2.1
- [147] M.M. Mac Low und A. Ferrara, *ApJ* **513** (1999), 142. 2.2.2
- [148] P. Madau, A. Ferrara und M.J. Rees, *ApJ* **555** (2001), 92. 2.2
- [149] P. Madau und F. Haardt, *ApJL* **693** (2009), L100. 4.2, 5.1.3
- [150] P. Madau, F. Haardt und M.J. Rees, *ApJ* **514** (1999), 648. 5.1.3
- [151] U. Maio, B. Ciardi, K. Dolag, L. Tornatore und S. Khochfar, *MNRAS* **407** (2010), 1003. 2.2.2, 5.4, 5.4.1
- [152] U. Maio, B. Ciardi, N. Yoshida, K. Dolag und L. Tornatore, *AAP* **503** (2009), 25. 5.4.1
- [153] U. Maio, K. Dolag, B. Ciardi und L. Tornatore, *MNRAS* **379** (2007), 963. 2.2, 2.2.2, 5.4.1
- [154] U. Maio, S. Khochfar, J.L. Johnson und B. Ciardi, *MNRAS* **414** (2011), 1145. 2.2.2
- [155] C.L. Martin, *ApJ* **621** (2005), 227. 2.2.2

- [156] C.L. Martin: *The Neutral Component of Galactic Winds. The Neutral Component of Galactic Winds*, In *Extra-Planar Gas*, herausgegeben von R. Braun, Band 331 von *Astronomical Society of the Pacific Conference Series*. (Juni 2005) Seite 305. 2, 2.2.1
- [157] A. Maselli, B. Ciardi und A. Kanekar, *MNRAS* **393** (2009), 171. 3.2.1, 3.3, 3.3.1, 3.3.1, 3.3.2, 4, 4.3.3, 4.4.1.1, 4.4.1.2, 4.4.3, 5.3
- [158] A. Maselli und A. Ferrara, *MNRAS* **364** (2005), 1429. 2.2.3, 3.3, 5, 5.1.3, 5.3, 1, 5.3.1, 5.3.2, 5.3.2, 5.4, 5.4.3
- [159] A. Maselli, A. Ferrara und B. Ciardi, *MNRAS* **345** (2003), 379. 3.2.1, 3.3, 3.3.1, 3.3.1, 4.3.3, 4.4.1.1, 5.3, 5.3.1
- [160] P. McDonald und J. Miralda-Escudé, *ApJL* **549** (2001), L11. 5.1.1, 5.1.2
- [161] M. McQuinn, *ApJL* **704** (2009), L89. 5.1.3
- [162] M. McQuinn, A. Lidz, M. Zaldarriaga, L. Hernquist, P.F. Hopkins, S. Dutta und C.A. Faucher-Giguère, *ApJ* **694** (2009), 842. 2.2.3, 5.1.3
- [163] A. Meiksin, *MNRAS* **356** (2005), 596. 5.1
- [164] A. Meiksin und P. Madau, *ApJ* **412** (1993), 34. 5.2
- [165] A. Meiksin und E.R. Tittley, *ArXiv e-prints* (2011). 5.1.3
- [166] A. Meiksin und M. White, *MNRAS* **342** (2003), 1205. 2.2.3, 5.1.3
- [167] A.A. Meiksin, *Reviews of Modern Physics* **81** (2009), 1405. 2, 2.2.3, 3.2, 5, 5.1.1, 5.1.3
- [168] A. Mesinger und S. Furlanetto, *MNRAS* **400** (2009), 1461. 5.2
- [169] D.M. Meyer und D.G. York, *ApJL* **315** (1987), L5. 2.2.1
- [170] D. Mihalas und B.W. Mihalas: *Foundations of radiation hydrodynamics*, 1984. 3.2
- [171] J. Miralda-Escudé, *MNRAS* **262** (1993), 273. 5.1.3
- [172] J. Miralda-Escudé, R. Cen, J.P. Ostriker und M. Rauch, *ApJ* **471** (1996), 582. 5.1.3
- [173] J. Miralda-Escudé und J.P. Ostriker, *ApJ* **350** (1990), 1. 5.2
- [174] H. Mo, F.C. van den Bosch und S. White: *Galaxy Formation and Evolution*, 2010. 1, 1.2, 1.2, 1.2, 2.1
- [175] M. Mori, A. Ferrara und P. Madau: *Early Metal-Enrichment by Pregalactic Outflows. Early Metal-Enrichment by Pregalactic Outflows*, In *8th Asian-Pacific Regional Meeting, Volume II*, herausgegeben von S. Ikeuchi, J. Hearnshaw, & T. Hanawa. (2002) Seiten 277–278. 2.2.2

- [176] M. Mori, A. Ferrara und P. Madau, *ApJ* **571** (2002), 40. 2.2.2
- [177] D.J. Mortlock, S.J. Warren, B.P. Venemans, M. Patel, P.C. Hewett, R.G. McMahon, C. Simpson, T. Theuns, E.A. Gonzáles-Solares, A. Adamson, S. Dye, N.C. Hambly, P. Hirst, M.J. Irwin, E. Kuiper, A. Lawrence und H.J.A. Röttgering, *NATURE* **474** (2011), 616. 2.1
- [178] M.B. Mosconi, P.B. Tissera, D.G. Lambas und S.A. Cora, *MNRAS* **325** (2001), 34. 2.2.2
- [179] N. Murray, E. Quataert und T.A. Thompson, *ApJ* **618** (2005), 569. 2.2.2, 2.2.2
- [180] S. Muzahid, R. Srianand und P. Petitjean, *MNRAS* **410** (2011), 2193. 5.1.3
- [181] J.F. Navarro, C.S. Frenk und S.D.M. White, *ApJ* **490** (1997), 493. 1.2
- [182] S.P. Oh, *MNRAS* **336** (2002), 1021. 2.2.3
- [183] K.A. Olive und E.D. Skillman, *ApJ* **617** (2004), 29. 5.1.2
- [184] B.D. Oppenheimer und R. Davé, *MNRAS* **373** (2006), 1265. 2.2.2, 2.2.2, 2.2.2, 2.2.3
- [185] B.D. Oppenheimer und R. Davé, *MNRAS* **387** (2008), 577. 2.2.2, 2.2.2
- [186] B.D. Oppenheimer, R. Davé und K. Finlator, *MNRAS* **396** (2009), 729. 2.2.3
- [187] D.E. Osterbrock und G.J. Ferland: *Astrophysics of gaseous nebulae and active galactic nuclei*, 2006. 4.2, 5.1
- [188] A.M. Partl, A. Maselli, B. Ciardi, A. Ferrara und V. Müller, *MNRAS* **414** (2011), 428. 3.2.1, 3.3, 5.3
- [189] P.J.E. Peebles: *Principles of Physical Cosmology*, 1993. 1.2
- [190] Y.C. Pei, *ApJ* **438** (1995), 623. 5.2
- [191] D. Péquignot, G. Ferland, H. Netzer, T. Kallman, D.R. Ballantyne, A.M. Dumont, B. Ercolano, P. Harrington, S. Kraemer, C. Morisset, S. Nayakshin, R.H. Rubin und R. Sutherland: *Photoionization Model Nebulae. Photoionization Model Nebulae*, In *Spectroscopic Challenges of Photoionized Plasmas*, herausgegeben von G. Ferland & D. W. Savin, Band 247 von *Astronomical Society of the Pacific Conference Series*. (2001) Seiten 533–+. 2.2.3, 4.1
- [192] P. Petitjean, *Astrophysics and Space Science Supplement* **277** (2001), 517. 2.2.1
- [193] P. Petitjean: *Metals at High Redshift. Metals at High Redshift*, In *From Lithium to Uranium: Elemental Tracers of Early Cosmic Evolution*, herausgegeben von V. Hill, P. François, & F. Primas, Band 228 von *IAU Symposium*. (2005) Seiten 575–580. 2.2.1

- [194] M. Pettini, S.L. Ellison, C.C. Steidel und D.V. Bowen, *ApJ* **510** (1999), 576. 2.2.1
- [195] M.M. Pieri und M.G. Haehnelt, *MNRAS* **347** (2004), 985. 2.2.1
- [196] M.M. Pieri, J. Schaye und A. Aguirre, *ApJ* **638** (2006), 45. 2.2.1
- [197] M.M. Pieri, J. Schaye, M.G. Haehnelt und A. Aguirre: *The Spatial Distribution of CIV in the Intergalactic Medium. The Spatial Distribution of CIV in the Intergalactic Medium*, In *22nd Texas Symposium on Relativistic Astrophysics*, herausgegeben von P. Chen, E. Bloom, G. Madejski, & V. Patrosian. (2005) Seiten 391–395. 2.2.1
- [198] M. Pierleoni, A. Maselli und B. Ciardi, *MNRAS* **393** (2009), 872. 3.3
- [199] M. Pierleoni, A. Maselli und B. Ciardi, *MNRAS* (2012). 3.3
- [200] G.C. Pomraning: *The equations of radiation hydrodynamics*, 1973. 3.2
- [201] W.H. Press und P. Schechter, *ApJ* **187** (1974), 425. 1.2
- [202] P. R.: *Progenitor systems of Type Ia Supernovae: mergers of white dwarfs and constraints on hydrogen-accreting white dwarfs*. TU Munich, Dissertation, 2010. 5.4.2
- [203] C.M. Raiteri, M. Villata und J.F. Navarro, *MemSAI* **67** (1996), 817. 2.2.2
- [204] M. Rauch, *ARAA* **36** (1998), 267. 2.1, 5.2
- [205] M. Rauch, M.G. Haehnelt und M. Steinmetz, *ApJ* **481** (1997), 601. 2.2.1
- [206] D. Reimers, C. Fechner, H.J. Hagen, P. Jakobsen, D. Tytler und D. Kirkman, *AAP* **442** (2005), 63. 5.1
- [207] D. Reimers, S. Kohler, L. Wisotzki, D. Groote, P. Rodriguez-Pascual und W. Wamsteker, *AAP* **327** (1997), 890. 5.1, 5.1.3, 5.2
- [208] M. Ricotti, N.Y. Gnedin und J.M. Shull, *ApJ* **534** (2000), 41. 5.1.1
- [209] M. Ricotti und J.P. Ostriker, *MNRAS* **350** (2004), 539. 2.2.2
- [210] E.V. Ryan-Weber, M. Pettini, P. Madau und B.J. Zych, *MNRAS* **395** (2009), 1476. 2.2.1
- [211] W.L.W. Sargent, P.J. Young, A. Boksenberg und D. Tytler, *ApJS* **42** (1980), 41. 5.1
- [212] S. Savaglio, S. Cristiani, S. D’Odorico, A. Fontana, E. Giallongo und P. Molaro, *AAP* **318** (1997), 347. 5.2
- [213] C. Scannapieco, P.B. Tissera, S.D.M. White und V. Springel, *MNRAS* **364** (2005), 552. 2.2.2

- [214] C. Scannapieco, P.B. Tissera, S.D.M. White und V. Springel, *MNRAS* **371** (2006), 1125. 2.2
- [215] C. Scannapieco, P.B. Tissera, S.D.M. White und V. Springel: *Effects of Supernova Feedback on the Formation of Galaxies. Effects of Supernova Feedback on the Formation of Galaxies*, In *IAU Symposium*, herausgegeben von J. Andersen, J. Bland-Hawthorn, & B. Nordström, Band 254 von *IAU Symposium*. (März 2009) Seiten 369–374. 2.2
- [216] C. Scannapieco, M. Wadepuhl, O.H. Parry, J.F. Navarro, A. Jenkins, V. Springel, R. Teyssier, E. Carlson, H.M.P. Couchman, R.A. Crain, C. Dalla Vecchia, C.S. Frenk, C. Kobayashi, P. Monaco, G. Murante, T. Okamoto, T. Quinn, J. Schaye, G.S. Stinson, T. Theuns, J. Wadsley, S.D.M. White und R. Woods, *ArXiv e-prints* (2011). 2.2.2
- [217] E. Scannapieco, *ApJL* **624** (2005), L1. 2.2
- [218] E. Scannapieco und L. Bildsten, *ApJL* **629** (2005), L85. 2.2.2
- [219] E. Scannapieco, A. Ferrara und P. Madau, *ApJ* **574** (2002), 590. 2.2, 2.2.2
- [220] E. Scannapieco, C. Pichon, B. Aracil, P. Petitjean, R.J. Thacker, D. Pogosyan, J. Bergeron und H.M.P. Couchman, *MNRAS* **365** (2006), 615. 2.2.2
- [221] E. Scannapieco, R.J. Thacker und M. Davis, *ApJ* **557** (2001), 605. 2
- [222] J. Schaye: *The warm-hot intergalactic medium. The warm-hot intergalactic medium*, In *38th COSPAR Scientific Assembly*, Band 38. (2010) Seiten 2632–+. 2
- [223] J. Schaye, A. Aguirre, T.S. Kim, T. Theuns, M. Rauch und W.L.W. Sargent, *ApJ* **596** (2003), 768. 2.2.1, 2.2.2, 5.2, 5.4.2
- [224] J. Schaye, C. Dalla Vecchia, C.M. Booth, R.P.C. Wiersma, T. Theuns, M.R. Haas, S. Bertone, A.R. Duffy, I.G. McCarthy und F. van de Voort, *MNRAS* **402** (2010), 1536. 2.2.2
- [225] J. Schaye, M. Rauch, W.L.W. Sargent und T.S. Kim, *ApJL* **541** (2000), L1. 2.2.1
- [226] J. Schaye, T. Theuns, M. Rauch, G. Efstathiou und W.L.W. Sargent, *MNRAS* **318** (2000), 817. 5.1.1
- [227] S.K. Sethi und B.B. Nath, *MNRAS* **289** (1997), 634. 5.2
- [228] P.R. Shapiro und M.L. Giroux, *ApJL* **321** (1987), L107. 5.2
- [229] A.E. Shapley, C.C. Steidel, M. Pettini und K.L. Adelberger, *ApJ* **588** (2003), 65. 2.2.1

- [230] J.M. Shull, D. Roberts, M.L. Giroux, S.V. Penton und M.A. Fardal, *AJ* **118** (1999), 1450. 5.1.3
- [231] J.M. Shull, J. Tumlinson, M.L. Giroux, G.A. Kriss und D. Reimers, *ApJ* **600** (2004), 570. 5.1, 5.1.3, 5.1.3
- [232] M. Shull, K. France, C. Danforth, B. Smith und J. Tumlinson, *ArXiv e-prints* (2010). 5.1.3
- [233] R.A. Simcoe, W.L.W. Sargent und M. Rauch, *ApJ* **606** (2004), 92. 2.2.1
- [234] A. Smette, S.R. Heap, G.M. Williger, T.M. Tripp, E.B. Jenkins und A. Songaila, *ApJ* **564** (2002), 542. 5.1.3
- [235] B. Smith, S. Sigurdsson und T. Abel, *MNRAS* **385** (2008), 1443. 2.2
- [236] I.M. Sobol: *The Monte Carlo Method*. Nauka, A984. 3.2.1
- [237] A. Sokasian, T. Abel und L. Hernquist, *MNRAS* **332** (2002), 601. 5.1
- [238] A. Songaila, *AJ* **115** (1998), 2184. 5.2
- [239] A. Songaila, *ApJL* **561** (2001), L153. 2.2.1
- [240] A. Songaila und L.L. Cowie, *AJ* **112** (1996), 335. 2.2.1, 5.2
- [241] A. Songaila, E.M. Hu und L.L. Cowie, *NATURE* **375** (1995), 124. 5.2
- [242] D. Spergel, L. Verde, H. Peiris, E. Komatsu, M. Nolta, C. Bennett, M. Halpern, G. Hinshaw, N. Jarosik, A. Kogut, M. Limon, S. Meyer, L. Page, G. Tucker, J. Weiland, E. Wollack und E. Wright, *ApJS* **148** (2003), 175. 1.1, 1.2
- [243] V. Springel, *MNRAS* **364** (2005), 1105. 5.4.1
- [244] V. Springel, C.S. Frenk und S.D.M. White, *NATURE* **440** (2006), 1137. 1, 1.2, 1.2
- [245] V. Springel und L. Hernquist, *MNRAS* **333** (2002), 649. 2, 2.2.2
- [246] V. Springel und L. Hernquist, *MNRAS* **339** (2003), 289. 2.2.2, 2.2.2
- [247] V. Springel, J. Wang, M. Vogelsberger, A. Ludlow, A. Jenkins, A. Helmi, J.F. Navarro, C.S. Frenk und S.D.M. White, *MNRAS* **391** (2008), 1685. 1.2
- [248] V. Springel, S.D.M. White, A. Jenkins, C.S. Frenk, N. Yoshida, L. Gao, J. Navarro, R. Thacker, D. Croton, J. Helly, J.A. Peacock, S. Cole, P. Thomas, H. Couchman, A. Evrard, J. Colberg und F. Pearce, *NATURE* **435** (2005), 629. 1.2
- [249] C.C. Steidel, *ApJS* **74** (1990), 37. 2.2.1

- [250] M. Steinmetz und E. Mueller, *AAP* **281** (1994), L97. 2.2.2
- [251] R.S. Sutherland und M.A. Dopita, *ApJS* **88** (1993), 253. 2.2, 5.4.1
- [252] B.D.J.B. Sykes: *Neutron Transport Theory*. Clarendon Press, Oxford, U.K., 1957. 3.2
- [253] D. Syphers, S.F. Anderson, W. Zheng, A. Meiksin, D. Haggard, D.P. Schneider und D.G. York, *ApJ* **726** (2011), 111. 5.1
- [254] D. Syphers, S.F. Anderson, W. Zheng, B. Smith, M. Pieri, G.A. Kriss, A. Meiksin, D.P. Schneider, J.M. Shull und D.G. York, *ApJ* **742** (2011), 99. 5.1
- [255] R.C. Telfer, W. Zheng, G.A. Kriss und A.F. Davidsen, *ApJ* **565** (2002), 773. 5.1.3
- [256] E. Tescari, M. Viel, V. D’Odorico, S. Cristiani, F. Calura, S. Borgani und L. Tornatore, *MNRAS* **411** (2011), 826. 2.2.2
- [257] E. Tescari, M. Viel, L. Tornatore und S. Borgani, *MNRAS* **397** (2009), 411. 2.2.2
- [258] R.J. Thacker, E. Scannapieco und M. Davis, *ApJ* **581** (2002), 836. 2.2
- [259] T. Theuns, M. Bernardi, J. Frieman, P. Hewett, J. Schaye, R.K. Sheth und M. Subbarao, *ApJL* **574** (2002), L111. 5.1
- [260] T. Theuns, A. Leonard, G. Efstathiou, F.R. Pearce und P.A. Thomas, *MNRAS* **301** (1998), 478. 2.1.1
- [261] T. Theuns, M. Viel, S. Kay, J. Schaye, R.F. Carswell und P. Tzanavaris, *ApJL* **578** (2002), L5. 2.2.2
- [262] T.A. Thompson, E. Quataert und N. Murray, *ApJ* **630** (2005), 167. 2.2.2
- [263] L. Tornatore, S. Borgani, K. Dolag und F. Matteucci, *MNRAS* **382** (2007), 1050. 2.2.2, 5.4.1
- [264] L. Tornatore, S. Borgani, F. Matteucci, S. Recchi und P. Tozzi, *MNRAS* **349** (2004), L19. 2.2.2
- [265] L. Tornatore, S. Borgani, M. Viel und V. Springel, *MNRAS* **402** (2010), 1911. 2.2.2
- [266] H. Trac und R. Cen, *ApJ* **671** (2007), 1. 2.2.3
- [267] T.M. Tripp, B.D. Savage und E.B. Jenkins, *ApJL* **534** (2000), L1. 2.2.1
- [268] D. Tytler, X.M. Fan, S. Burles, L. Cottrell, C. Davis, D. Kirkman und L. Zuo: *Ionization and Abundances of Intergalactic Gas*. *Ionization and Abundances of Intergalactic Gas*, In *QSO Absorption Lines*, herausgegeben von G. Meylan. (1995) Seiten 289–+. 2.2.1

- [269] P. Valageas, R. Schaeffer und J. Silk, *AAP* **388** (2002), 741. 5.1.1, 5.1.1
- [270] S. Veilleux, G. Cecil und J. Bland-Hawthorn, *ARAA* **43** (2005), 769. 2.2.1
- [271] A. Verhamme, D. Schaerer und A. Maselli, *AAP* **460** (2006), 397. 3.3
- [272] G.M. Voit, G.L. Bryan, M.L. Balogh und R.G. Bower, *ApJ* **576** (2002), 601. 2
- [273] J. Wadsley und J.R. Bond: *Probing the High Redshift IGM: SPH+P{3} MG Simulations of the Lyman-alpha Forest. Probing the High Redshift IGM: SPH+P{3} MG Simulations of the Lyman-alpha Forest*, In *American Astronomical Society Meeting Abstracts*, Band 28 von *Bulletin of the American Astronomical Society*. (Dezember 1996) Seite 104.02. 2.1.1
- [274] R.V. Wagoner, *ApJ* **179** (1973), 343. 1.1, 1.2
- [275] D. Weinberg und et al.: *Cosmological tests with the Ly- α forest (invited review). Cosmological tests with the Ly- α forest (invited review)*, In *Evolution of Large Scale Structure : From Recombination to Garching*, herausgegeben von A. J. Banday, R. K. Sheth, & L. N. da Costa. (Januar 1999) Seite 346. 5.1.2
- [276] D.H. Weinberg, J. Miralda-Escude, L. Hernquist und N. Katz, *ApJ* **490** (1997), 564. 5.1.2, 5.1.3
- [277] R.J. Weymann, R.F. Carswell und M.G. Smith, *ARAA* **19** (1981), 41. 2.1
- [278] R.L. White, R.H. Becker, X. Fan und M.A. Strauss, *AJ* **126** (2003), 1. 2.1, 2.2
- [279] R.P.C. Wiersma, J. Schaye, C. Dalla Vecchia, C.M. Booth, T. Theuns und A. Aguirre, *MNRAS* **409** (2010), 132. 2.2.2
- [280] R.P.C. Wiersma, J. Schaye und B.D. Smith, *MNRAS* **393** (2009), 99. 2.2, 5.4.1
- [281] R.P.C. Wiersma, J. Schaye und T. Theuns, *MNRAS* **415** (2011), 353. 2.2.2
- [282] R.P.C. Wiersma, J. Schaye, T. Theuns, C. Dalla Vecchia und L. Tornatore, *MNRAS* **399** (2009), 574. 2.2.2
- [283] G. Worseck, C. Fechner, L. Wisotzki und A. Dall'Aglio, *AAP* **473** (2007), 805. 5.2
- [284] G. Worseck, J.X. Prochaska, M. McQuinn, A. Dall'Aglio, C. Fechner, J.F. Hennawi, D. Reimers, P. Richter und L. Wisotzki, *ApJL* **733** (2011), L24. 5.1.2, 5.1.2, 5.1.3
- [285] G. Worseck und L. Wisotzki: *The Transverse Proximity Effect in Spectral Hardness. The Transverse Proximity Effect in Spectral Hardness*, In *Cosmic Frontiers*, herausgegeben von N. Metcalfe & T. Shanks, Band 379 von *Astronomical Society of the Pacific Conference Series*. (Dezember 2007) Seite 235. 5.2

- [286] K.K.S. Wu, O. Lahav und M.J. Rees, *NATURE* **397** (1999), 225. 1.1
- [287] J.S.B. Wyithe und A. Loeb, *ApJ* **586** (2003), 693. 5.1
- [288] N. Yoshida, T. Abel, L. Hernquist und N. Sugiyama, *ApJ* **592** (2003), 645. 5.4.1
- [289] M.S. Yun, P.T.P. Ho und K.Y. Lo, *NATURE* **372** (1994), 530. (document)
- [290] Y. Zhang, P. Anninos und M.L. Norman, *ApJL* **453** (1995), L57. 2.1.1
- [291] W. Zheng, K. Chiu, S.F. Anderson, D.P. Schneider, C.J. Hogan, D.G. York, S. Burles und J. Brinkmann, *AJ* **127** (2004), 656. 5.1
- [292] W. Zheng, A.F. Davidsen und G.A. Kriss, *AJ* **115** (1998), 391. 5.2
- [293] W. Zheng und L.Z. Fang, *ApJ* **505** (1998), 519. 5.2
- [294] W. Zheng, G.A. Kriss, J.M. Deharveng, W.V. Dixon, J.W. Kruk, J.M. Shull, M.L. Giroux, D.C. Morton, G.M. Williger, S.D. Friedman und H.W. Moos, *ApJ* **605** (2004), 631. 5.1.3
- [295] L. Zuo, *MNRAS* **258** (1992), 36. 2.2.3, 5.1.3
- [296] L. Zuo, *MNRAS* **258** (1992), 45. 2.2.3, 5.1.3

Acknowledgements

At the end of this thesis, I would like to say thanks to Benedetta Ciardi, for the time she spent on it and the many improvements she has provided to the final version. A special thank-you goes to Antonella Maselli, who introduced me to the problem of cosmological radiative transfer.

Furthermore my thanks go to Simon White and the Max-Planck-Institut für Astrophysik for their enduring support and for the exceptional scientific environment they have created in Garching.

Finally, a special mention goes to the MPA secretary staff: Maria, Gabi and Cornelia for being so competent, supportive and friendly.

Un doveroso ringraziamento va a Renata, Tina e Lorenz per la versione tedesca del sommario.

Curriculum vitae

GRAZIANI LUCA

Personal information

Addresses: Schellingstrasse, 30 – 80799 Munich – Germany / Via dell’Ariento, 11 – 50123 Florence - Italy

E-mails: lgmaxp@mpa-garching.mpg.de, graziani@arcetri.astro.it

Nationality: Italian

Place/Date of birth: Macerata, Italy, 12th August 1973

Education and Academic Record

- 2012 - Institution: PhD LMU Munich and MPA Garching - Germany. Thesis Title: Cosmological radiative transfer through metals in CRASH . Supervisors: Dr. Benedetta Ciardi and Prof. Simon White
- 2008 - Institution: LMU Munich and MPA Garching - Germany. Start of PhD studies at LMU/MPA with IMPRS scholarship of the Max-Planck-Gesellschaft
- 2008 - Institution: University of Florence - Italy. Laurea specialistica in Scienze fisiche e Astrofisiche 20s (eq. Master Degree). Thesis Title: Il trasporto della radiazione nei dischi protoplanetari: il ruolo della polvere (Radiative transfer in dusty protoplanetary disks). Supervisor: Prof. Santi Aiello
- 2007 - Institution: CINECA Bologna - Italy. Summer School of Scientific Visualization and 3D interactive Graphics Advanced School of Parallel computing.
- 2005 - Institution: University of Pisa - Italy. Laurea in Fisica 25s (eq Bachelor). Thesis Title: Metodi numerici per la soluzione di problemi di dinamica planetaria (Numerical methods in Planetary System Dynamics). Supervisor: Prof. P. Paolicchi

- 2003 - Institution: CINECA Bologna - Italy. MPI and OpenMP Programming Courses
- 2002 - Institution: République française – Ministère de l'éducation nationale - France. DALF – Diplôme approfondi de langue française – CEF Level: C2
- 2001 - Institution: République française – Ministère de l'éducation nationale - France. DELF – Diplôme d'études en langue française
- 1992 - Institution: Scientific High School “Galileo Galilei” - Macerata – Italy. Scientific High-School Diploma

Professional Record

Since 1995: Working experience in the field of Information Tecnology as Software Architect. Professional development in Java Enterprise IBM Websphere, IBM DB2, IBM Visualage C++, IBM Visualage SmallTalk, IBM Voice Technologies. Teaching experience for Professionals and High School Students.

Scientific Conferences and Workshops

- 2007 EANA 2007 7th European Workshop on Astrobiology, University of Turku, Turku, Finland. Radiative Transfer in Protoplanetary Disk: vertical energy structure modelling and disk chemistry effects. (Poster Contribution)
- 2008 EPSC2008 European Planetary Science Congress 2008, Münster, Germany. Radiative transfer in protoplanetary disks. (Poster Contribution)
- 2008 Cosmological Radiative Transfer Comparison Project Workshop, University of Texas, Austin, USA
- 2009 The Chemical Enrichment of the Intergalactic Medium, Leiden, The Netherlands
- 2010 European-US Summer School on HPC Challenges in Computational Sciences, Acireale, Italy. DEISA and TeraGrid – Europe USA – DEISA Grant
- 2010 Cosmological Reionization HRI, Allahabad, India
- 2010 5th VI-HPS Tuning Workshop TUM/LRZ/MPG in Garching, München, Germany
- 2010 5th Heidelberg Summer School: First Stars and Cosmic Reionization, International Max Planck Research School for Astronomy and Cosmic Physics, University of Heidelberg, Germany

- 2011 New Horizons for High redshifts, Institute of Astronomy, University of Cambridge, UK. Cosmological radiative transfer through metals in CRASH (Poster Contribution)
- 2011 Young and Bright: Understanding High Redshift Structures, Potsdam, Germany.

Refereed Publications

- *Graziani, L.*, Barletti, L., Aiello, S., & Cecchi-Pestellini, C. (2010). Radiative transfer modelling in protoplanetary disks with the P-N approximation and Monte Carlo techniques. *Mathematical Methods in the Applied Sciences*, 33(10), 1263-1273. doi:10.1002/mma.1285.
- Ciardi, B.; Bolton, J. S.; Maselli, A.; *Graziani, L.* (2011). The effect of intergalactic helium on hydrogen reionisation: implications for the sources of ionising photons at $z > 6$. Submitted to MNRAS, eprint arXiv:1112.4646

In preparation

- *Graziani L.*, Maselli A. and Ciardi B., CRASH3: cosmological radiative transfer through metals. (MNRAS)
- *Graziani L.*, Ciardi B., Maio U. and Maselli A., Cosmic UV background fluctuations at redshift $z \sim 3$. (MNRAS)